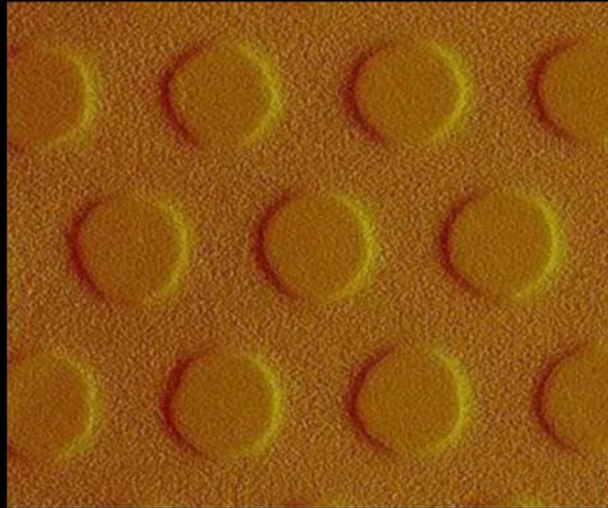# Self-Assembled Monolayers on Metal Oxides: Applications in Nanotechnology

Oktay YILDIRIM

SELF-ASSEMBLED MONOLAYERS ON METAL OXIDES:

APPLICATIONS IN NANOTECHNOLOGY

nano Ned

SELF-ASSEMBLED MONOLAYERS ON METAL OXIDES:

APPLICATIONS IN NANOTECHNOLOGY

PROEFSCHRIFT

ter verkrijging van

de graad van doctor aan de Universiteit Twente,

op gezag van de rector magnificus,

prof. dr. H. Brinksma,

volgens besluit van het College voor Promoties

in het openbaar te verdedigen

op woensdag 8 december 2010 om 15.00 uur

door

Oktay Yildirim

geboren op 25 mei 1977

te Erzurum, Turkije

Dit proefschrift is goedgekeurd door:

Promotoren: prof. dr. ir. J. Huskens
                          prof. dr. ing. A.J.H.M. Rijnders

To my friends and family

Table of Contents

Chapter 1

General Introduction

Nanotechnology is a multidisciplinary field. On one hand, it deals with understanding the behavior of materials at the nanometer scale, which is nanoscience, on the other hand the manipulation and fabrication of materials to obtain nanostructured objects, which is nanotechnology. Nanofabrication is a discipline of nanotechnology which is focused on the preparation of nanostructures by a range of fabrication methods.[1] Approaches to create nanostructures are top-down or bottom-up strategies[1-2] as well as combinations of these two.[2-3] Top-down uses lithography techniques to create (nano)patterns with arbitrary shapes and with superior precision. Bottom-up methods create well-defined (nano)structures in two and three dimensions, from elementary building blocks by using specific interactions between molecules or nano particles.

Bottom-up self-assembly of molecules is a very efficient, simple and rapid method to create functional features at various length scales.[4-5] Self-assembled monolayers (SAMs) of thiols on gold and silanes on SiO_2 have been extensively used to create functional nanostructures, but SAMs on metal oxides are relatively less studied. However, metal oxides offer a broad range of materials properties such as insulating, semiconducting, metallic, superconducting, ferroelectric, piezoelectric, and ferromagnetic.[6-8] Therefore, it would be of interest to combine SAMs and metal oxides. Moreover, with their smooth and well-defined surfaces, metal oxides can provide good templates for SAM growth. Patterning and modifying metal oxides with SAMs may be used for adding new functionalities to the metal oxide surfaces, for changing their surface properties, and for device fabrication. Of the existing classes of adsorbates on metal oxides, phosph(on)ate-based molecules form SAMs with high ambient stability. Phosphates and phosphonates will be named as phosph(on)ates throughout this thesis.

The research presented in this thesis contributes to the understanding of structural and functional properties of self-assembled monolayers of phosph(on)ates on metal oxides. Some fundamental questions are addressed. What are the coverage,

packing, orientation and stability of the SAMs on metal oxides? What are the electrical properties of these SAMs? How can SAMs with different end-groups be used to add new functionalities to metal oxides? What kind of patterning techniques can be used and what kind of patterns can be created? To address these questions, the use of phosph(on)ate-based SAMs on conducting metal oxides for electrical applications and for directing the adsorption of magnetic NPs for data storage applications have been studied. SAMs were used to pattern and modify metal oxides to create functional inorganic-organic composite structures.

Chapter 2 gives an overview of self-assembled monolayer types used on metal oxides and compares them in terms of SAM formation (bond mechanism, interaction between the head-group and substrate surface, growth mechanism), quality (coverage, packing, order), structure (configuration) and stability. Patterning metal oxides with SAMs is reviewed and several examples in which SAMs or SAM patterns are used at biomaterials or in electronic applications or as wear and corrosion resistants are discussed.

Chapter 3 deals with the assembly of phosph(on)ate-based SAMs on single crystal metal oxide substrates such as Al_2O_3. Defect free SAM layers with high coverage, bound to the metal oxide substrates through phosph(on)ate headgroups with methyl, amino, thiol or carboxylic acid terminations are prepared.

Chapter 4 describes the electrochemical properties of SAMs on the conducting metal oxide Nb-STO. The effect of chain length of the SAM on the properties of the formed insulating barrier is investigated as well as the electrochemical stability of phosph(on)ate based SAMs.

In Chapter 5, SAMs are used as a dielectric thin film on Nb-STO to decrease the leakage current. Pt top metal electrodes are deposited by pulsed laser deposition (PLD) on bare Nb-STO and on the same type of substrate modified with a tetradecylphosphate SAM. Electrochemical Cu deposition is employed to show the efficiency of PLD to prepare top electrodes without crashing into the SAM layer.

In Chapter 6, functionalized adsorbates are used as linkers to assemble ferromagnetic FePt nanoparticles (NP) on an alumina surface in a controlled way. Microcontact printing was employed to create a chemical contrast on the alumina surface for directional assembly of nanoparticles as a method to prepare NP patterns. Structural and magnetic properties of the FePt assemblies are observed as well.

Finally, chapter 7 employs nanoimprint lithography (NIL) and nanomolding in capillaries (NAMIC) to create magnetic nanoparticle patterns at micrometer and nanometer scales on aluminum oxide substrates. The polymer template generated by NIL behaves as a physical barrier on the substrate and defines the pattern areas. Magnetic characterization of NP patterns is done by magnetic force microscopy (MFM). Effect of applying an external magnetic field during assembly to align ferromagnetic FePtAu NPs is shown.

References

1. Gates, B. D.; Xu, Q. B.; Stewart, M.; Ryan, D.; Willson, C. G.; Whitesides, G. M., *Chem. Rev.* **2005,** *105*, 1171.
2. Maury, P.; Crespo-Biel, O. P., M.; Reinhoudt, D. N.; Huskens, J. In *Integration of Top-Down and Bottom-Up Nanofabrication Schemes*, Mater. Res. Soc. Symp. Proc., 2006; pp 0901.
3. Maury, P.; Peter, M.; Mahalingam, V.; Reinhoudt, D. N.; Huskens, J., *Adv. Funct. Mater.* **2005,** *15*, 451.
4. Wang, J. Q.; Yang, S. R.; Chen, M.; Xue, Q. J., *Surf. Coat. Technol.* **2004,** *176*, 229.
5. Whitesides, G. M.; Grzybowski, B., *Science* **2002,** *295*, 2418.
6. Ahn, C. H.; Triscone, J. M.; Mannhart, J., *Nature* **2003,** *424*, 1015.
7. Dagotto, E., *Science* **2005,** *309*, 257.
8. Hwang, H. Y., *MRS Bull.* **2006,** *31*, 28.

Chapter 2

Self-Assembled Monolayers on Metal Oxides

Abstract

       Self-assembled monolayers (SAMs), in particular thiols on gold and silanes on SiO_2, have been studied extensively, but SAMs on metal oxides are relatively new. Alkyl phosph(on)ates form more densely packed, more ordered and more stable SAMs on metal oxides when compared to alkanoic acid-based molecules. Phosph(on)ate based SAMs can be used to pattern metal oxide surfaces by microcontact printing and photopatterning, and the pattern can be transferred by etching. In biomaterial applications, they can be used to facilitate cell growth or to prevent protein adsorption. They enhance the properties of OLED devices by improving the interface properties between organic and inorganic electrodes. Moreover, they form additional dielectric layers and decrease the leakage current at electrical applications. By combining suitable molecules and fabrication techniques, SAMs can add new functionalities to the metal oxide surfaces and can potentially be used in device fabrication.

2.1 Introduction

Self–assembled monolayers (SAMs) may be defined as ordered molecular assemblies formed spontaneously by the adsorption of a surfactant with a specific affinity of its headgroup to a substrate.[1] SAMs can completely change the surface properties although they are extremely thin (typically 2 nm).[2] Due to ease of preparation, low cost, availability of a variety of functionalities, and their structural properties, SAMs have potential applications in protective coatings, catalysts, biological sensors, optoelectronic devices, adhesion promoters, etc. [3]

The most frequently studied adsorbate/substrate pairs are thiols on gold surfaces[1] and silanes on SiO_2,[2] but SAMs on metal oxides are relatively new. Silanes on SiO_2 form a cross-polymerized network of molecules with only a few bonds to the SiO_2 surface.[4] Silane-based SAMs have been formed on metal oxides[5-8] with similar properties in terms of bond mechanism, coverage and morphology,[8] so they will not be covered in this overview. Alkanoic acid-based[3, 9-22] and phosph(on)ate-based[23-32] SAMs on several metal oxides such as Al_2O_3, TiO_2, ITO and Ta_2O_5, are the most studied ones, however SAMs of hydroxamic acids,[33] alkyl isocyanates,[34] sodium alkyl sulfates[35] and poly(L-lysine)-g-poly(ethylene glycol) (PLL-g-PEG)[36] have also been reported. In most of the studies amorphous metal oxides with 10-250 nm thickness were used.
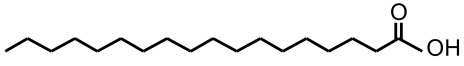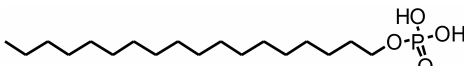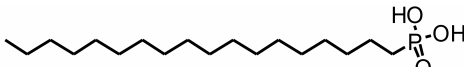
In this review, alkanoic acid and phosph(on)ate-based SAMs on several metal oxide surfaces are covered. SAM systems will be described in terms of SAM formation (bond mechanism, interaction between the head-group and substrate surface, growth mechanism), quality (coverage, packing, order), structure (configuration) and stability. The preparation of patterned SAMs is reviewed in terms of advantages and limitations of the used patterning techniques. Finally, some examples are shown in which SAMs or SAM patterns are used for biomaterials or electronic applications, or as wear and corrosion resistants.

2.2 Self-assembled monolayers (SAMs) on metal oxides

Generally, two main classes of adsorbates on metal oxides can be discriminated, n-alkanoic acids and alkylphosph(on)ates. It should be noted that the same organic molecules may be named differently. n-Alkanoic acids are also named carboxylic acids or fatty acids. Stearic acid, for example, is a carboxylic acid which

has 18 carbon atoms in its structure. The structures and molecular formulas of some of the organic molecules which are mentioned in this review are shown in Table 2.1. SAMs reviewed here are usually prepared by immersion of a clean substrate into a solution of the adsorbate, unless mentioned otherwise.

Table 2.1 Structure and molecular formulas of some organic molecules.

Type of Molecule	Name(s) of Molecule	Structure
Carboxylic acid, n-alkanoic acid, Fatty acid	Stearic acid, Octadecanoic acid	
Alkylphosphoric acid	Octadecylphosphoric acid	
Alkylphosphonic acid	Octadecylphosphonic acid	

2.2.1 n-Alkanoic acid SAMs on metal oxides

n-Alkanoic acid SAM formation has been reported on several metal oxide surfaces, prepared from solution within a few minutes to several days,[3, 9-22] resulting in densely packed monolayers with a tilt angle up to 25°. As usually agreed upon, chemisorption occurs by proton dissociation to form carboxylate species[10-11] with mono[3, 17, 21] and bidentate[16, 20] binding modes but the headgroup-substrate interaction is generally accepted to be weak.[21] Some authors claim that the SAMs are resistant to solvent rinsing[10-11, 22, 33] while others report partial or complete SAM removal upon solvent exposure.[17, 20-21]

Taylor *et al*. explained the contradicting results in terms of kinetics or stability with the effect of ambient exposure or hydration of the substrates prior to SAM formation.[21] Similarly, Pertays *et al.* pointed out the importance of the substrate history prior to SAM formation.[19] They found hydroxyl formation in the ambient atmosphere to increase stearic acid adsorption density and SAM order. On the other hand, carbon contamination blocked adsorption sites and caused disorder. Oxygen plasma treatment removed adsorbed carbonaceous material from the aluminium surface and significantly increased the order of the stearic acid monolayer.[19]

Tao demonstrated that the structure of n-alkanoic acid SAMs on native oxide surfaces of copper, aluminum, and silver depends on the substrates as well as chain length.[20] According to the IR data, peak shape and relative intensities for the carboxylate head group were very much the same for all the acids with different chain lengths. This would imply that the binding geometry of the head group is determined by the interaction between the substrate and head group and is independent of chain length. Molecules bind the silver oxide surface in a symmetrical way, while they interact with aluminum and copper oxide asymetrically (Figure 2.1).[20] IR results indicated a shift to a highly ordered crystalline phase with increasing chain length due to the cohesive forces. Ellipsometry suggested a tilt angle of 15-25° for SAMs of all chain lengths on silver. On the surface of copper oxide as well as aluminum oxide, the binding geometry resulted in normal-oriented molecules. The isoelectric points followed $Al_2O_3 < Cu_2O < AgO$, showing that Al_2O_3 is the least basic among all which results in weaker coordination to carboxylates. In line with this, monolayers on alumina are not resistant to solvent rinsing.
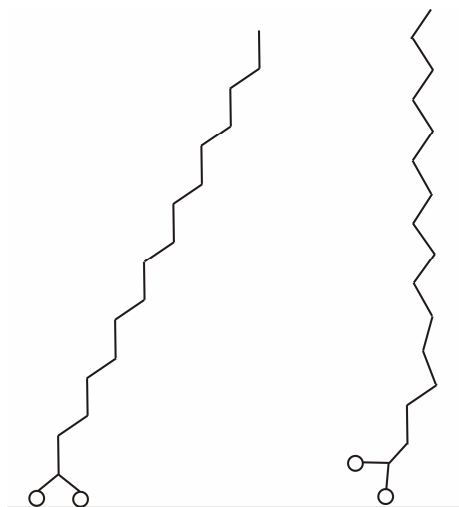
Figure 2.1 Proposed structures of n-alkanoic acid monolayers on (a) silver oxide, (b) copper oxide and aluminum oxide surfaces.[20]

Taylor *et al.* investigated the growth of octadecanoic acid on single crystal C-plane (0001) and R-plane (1$\bar{1}$02) faces of sapphire (α-Al_2O_3) by atomic force microscopy (AFM), contact angle (CA) and Fourier transform infrared spectroscopy (FTIR).[21] Since the sapphire terraces (after film formation) are distinctly visible in AFM images, monolayers are conformal. From the phase images and high contact

angle values at early stages of SAM formation, the authors claimed that the dark regions are not bare substrate but regions covered with thin layers of disordered molecules. Despite the higher reactivity of step edges, no preferential growth on these regions was observed (Figure 2.2). They claimed that the interaction between the organic molecule and the substrate surface is a weak carboxylic acid-sapphire bonding interaction enabling adsorbate mobility and defect annealing (Figure 2.2). Partial desorption upon rinsing supports the weak interaction view.
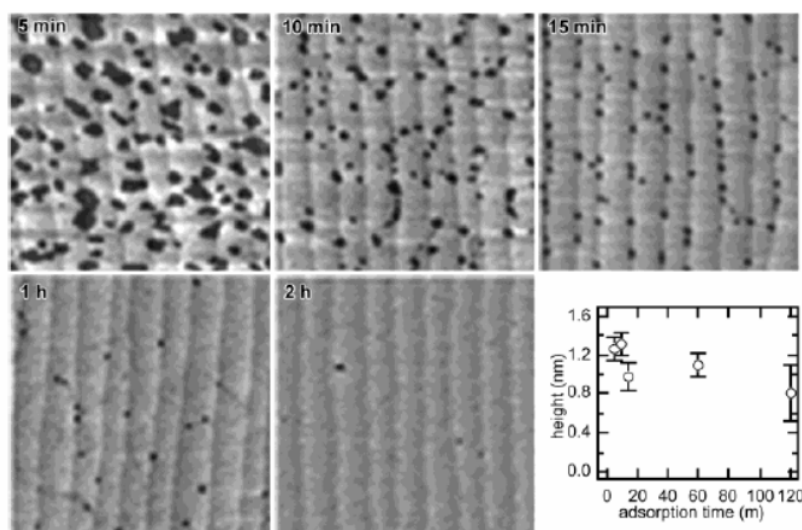
Figure 2.2 Series of ex situ, tapping mode AFM images (1 μm x1 μm) depicting octadecanoic acid monolayer growth at R-sapphire from a 1.5 mM solution in hexadecane. The adsorption times ranging from 5 min to 2 h are displayed in the images. The graph at the lower right displays the average AFM heights measured in these images.[21]

Lim *et al.* compared the bonding mechanism and the stability of stearic acid SAMs on single-crystal C-plane aluminum oxide (sapphire) and amorphous aluminum oxide (alumina).[16] For the SAM on sapphire, the XPS peaks at 284.8 and 289.0 eV were assigned to the alkyl chain (C-C) and carboxylate (-COO-) carbon atoms. No carboxylic carbon (-COOH) was detected, which shows the absence of free acid on the surface.The oxygen peak at 532.3 eV was assigned to carboxylate oxygens (Al-O-C). IR was done on SAMs on sapphire and amorphous alumina surfaces and the results were compared to bulk stearic acid spectra. In both cases there was no peak assigned to C-O-H stretches which indicated bonding with the substrate. For SAM on amorphous alumina, the peak at 1733 cm^{-1} was assigned to C=O, indicating

monodentate binding (A in Figure 2.3). Peaks at 1666 and 1621 cm^{-1} indicated the weakening of C=O into a carboxylate (B and C in Figure 2.3). The peak at 1464 cm^{-1} was attributed to the symmetric bonding mode of a carboxylate (D in Figure 2.3). For SAMs on sapphire, the spectra indicated bidentate interactions through a carboxylate (B, C, D in Figure 2.3). Based on XPS and IR the authors concluded that stearic acid makes a bidentate bonding with sapphire and both monodentate and bidentate with amorphous alumina. They explained this by the polycrystalline or the amorphous nature of the alumina surface which offers different types of adsorption sites, while sapphire has limited types of adsorption sites due to its single-crystalline nature. Stearic acid assembled on the sapphire surface was immersed into water to investigate desorption. The desorption from atomically smooth sites was faster than from sites of surface defects such as kinks, steps, and atomic vacancies probably due to weaker interaction with smooth regions (Figure 2.4).
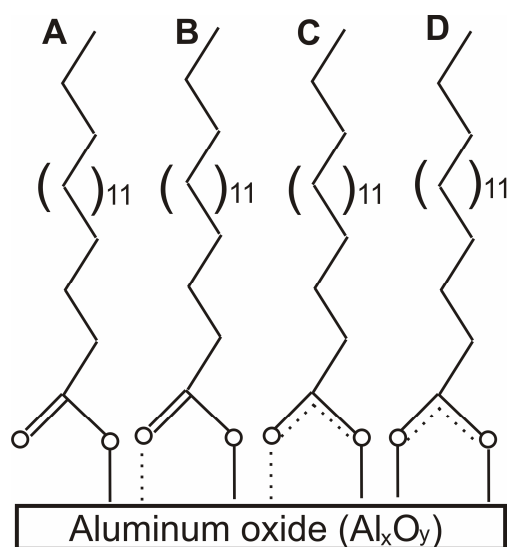
Figure 2.3 Possible interaction modes between the carboxylic acid head group and the Al$_2$O$_3$ surface with varying degrees of interaction between the carbonyl oxygen and the surface, leading to varying degrees of double bond character remaining in the head group.[16]
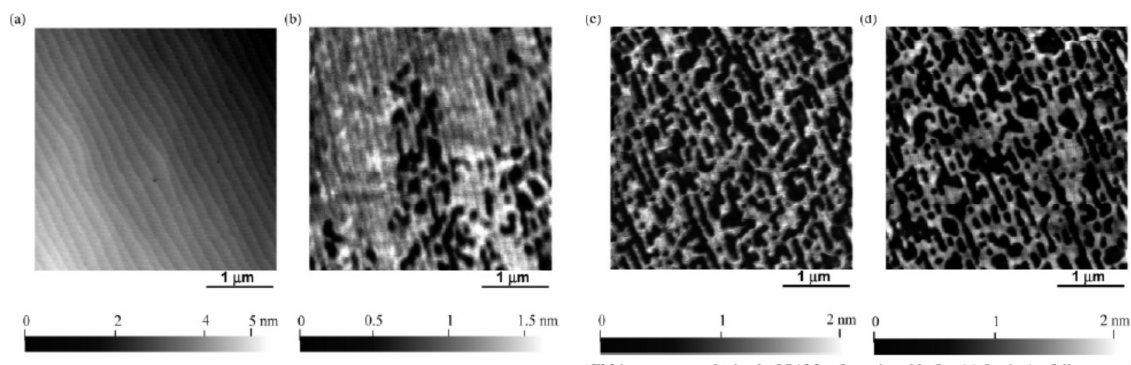
Figure 2.4 Tapping mode AFM images obtained for SAMs of stearic acid after (a) 0 min (or fully covered SAM before immersion in water), (b) 30 min, (c) 120 min, and (d) 180 min of immersion in water. [16]

Aronoff *et al.* treated aluminum oxide surfaces with an alkoxide of zirconium to improve the binding strength of the alkanoic acid which is deposited from the vapor phase and formed a semi-crystalline SAM layer.[12] The authors claimed that the formation of an interfacial zirconium carboxylate results in strong adhesion, since no carboxylic acid was detected and the IR spectra remained unchanged after two months of exposure to ambient conditions. However, they also found that the layer desorbed for 80% upon immersion in water.

2.2.2 Phosph(on)ate-based SAMs on metal oxides

Phosph(on)ate-based SAMs have been reported on different metal oxide surfaces such as Al_2O_3,[24, 28-30, 37-50] TiO_2,[26, 29, 32, 51-61], ITO[62-64] Cu_2O,[65-66] Fe_2O_3,[23, 67-71] Ta_2O_5,[31, 72] teeth,[73] nitinol,[74-75] TiO_2 and ZrO_2 powders.[18, 76-79]

Although there have been several mechanisms proposed for the phosph(on)ates binding to the metal oxides, the binding mechanism is still not completely understood partly due to the wide range of binding possibilities, monodentate[31, 46, 76], bidentate[31, 71, 80] and tridentate.[43, 56, 81] Transition metal oxides, such as TiO_2 and ZrO_2, are known to form stable phosph(on)ate-metal (P-O-M) bonds.[57, 72]

Gao *et al.*[76-77] and Pawsey *et al.*[82] have prepared highly ordered monolayers of octadecylphosphonate onto ZrO_2 and TiO_2 powders. They showed that alkyl phosphonates bind stronger and yield better oriented SAMs on ZrO_2 compared to TiO_2 and concluded that binding occurs through condensation with OH groups on the

metal oxide surfaces, based on the formation of P-O-M bonds and the disappearance of M-OH and P-OH signals in NMR and infrared spectroscopy, similar to a study by Pellerite *et al*.[46]

Hofer *et al*.[72] and Hahner *et al*.[57] studied the SAMs of alkyl phosphates on Ta_2O_5, Al_2O_3, ZrO_2, TiO_2 and Nb_2O_5, resulting in highly hydrophobic surfaces with CAs >110°, resembling the thiol/gold system, however they did not provide CA hysteresis data which could give an estimate of the degree of order of the SAMs. The authors showed that the isoelectric points (IEP) of different metal oxides did not affect SAM formation and they found that the film structures of all monolayers on the macroscopic scale were similar, in terms of packing density, inclination and molecular order, independent of the underlying oxide and the the crystallinity of the substrate. This might be due to several possible binding modes for the phosphate head group (mono, bi or tridentate) giving flexibility at orientation. XPS data showed that the phosphate headgroup is attached to the substrate surface and that the hydrocarbon tail is pointing upwards.

Textor *et al*. showed that octadecylphosphate (ODP) self-assembles on amorphous/nanocrystalline Ta_2O_5.[31] The authors used several analytical techniques to propose a binding mechanism and to construct a model of conformational arrangement for the molecules in the substrate/SAM system. They proposed a model of the ODP/Ta_2O_5 system based on near edge X-ray absorption fine structure spectra (NEXAFS) which provided information about chain order and an average tilt angle of 30-35°, while the AFM data showed nearly hexagonal order and the ToF-SIMS results showed P-O-Ta and $(-P-O-)_2Ta$ species indicating coordination of more than one phosphate to a single tantalum (Figure 2.5). The strong ToF-SIMs peaks of $Ta_aP_bO_cH_d$ and $Ta_aP_bO_cC_dH_e$ fragments suggests a strong phosphate headgroup coordination to Ta ions. If the interactions were a weak hydrogen bonding between $ROPO(OH)_2$ and Ta-O, it would be unlikely that $Ta_aP_bO_cH_d$ and $Ta_aP_bO_cC_dH_e$ species would survive. The XPS data showed a tails-up orientation, charge transfer from the substrate to ODPA, an adsorbed layer thickness of 2.2 nm, the presence of both monodentate and bidentate coordination, and the inability of a single type of coordination to explain the observed ratio between different oxygen modes. The authors claimed that the periodicity of the Ta cations is the prime factor in their model determining the order of the ODP layer.

In Figure 2.6 a schematic illustration of proposed arrangement of the phosphate groups on the Ta_2O_5 surface is shown.[31] The authors do not have direct experimental evidence for the surface complex formation mechanism but they assumed, considering the strong O-Ta bond, it is not likely that free Ta atoms are present at the surface under ambient conditions. Apparently, hydroxylation is an important initial step prior to phosphonate-based SAM formation on Al_2O_3. Along this line, they proposed a binding mechanism of monodentate and bidentate phosphate-Ta(V) interactions as shown in Figure 2.5a.
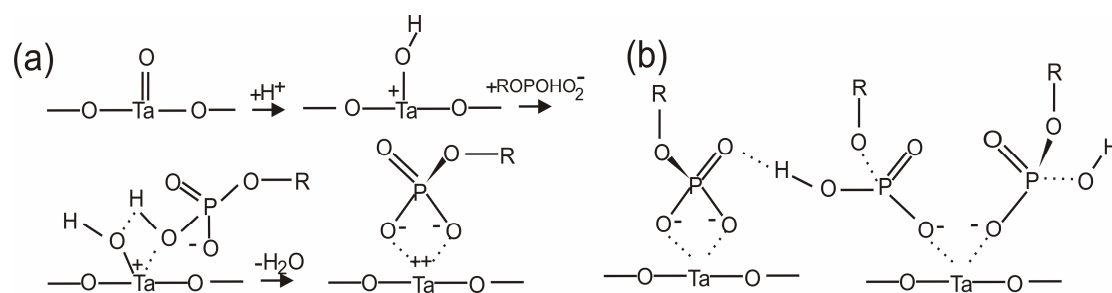
Figure 2.5 (a) Proposed reaction sequence in the displacement of oxide ligands at the Ta_2O_5 surface by alkylphosphates through intermediate hydroxide formation. (b) Bidentate (left) and monodentate (right) phosphate coordination to tantalum ions, with the possibility for the formation of intermolecular hydrogen bonding.[31]
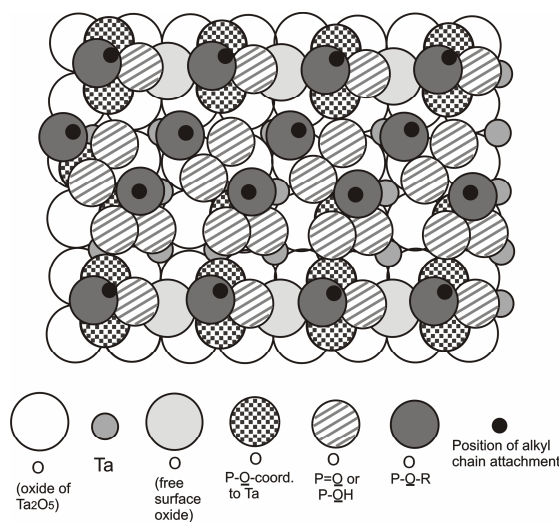
Figure 2.6 Schematic, idealized view of the arrangement and orientation of phosphate groups of ODPA at a Ta_2O_5 surface (with square substrate lattice). The phosphates are bound to the Ta ions through either monodentate or bidentate coordination. The P-O-R groups form a nearly perfect hexagonal lattice with a mean distance between the hydrocarbon (R) chains of approximately 4.9 Å.[31]

Spori *et al.* studied the influence of alkyl chain length on the properties of alkyl phosphate SAMs on amorphous TiO_2.[60] The authors claimed that the degree of order and the packing density within the monolayers were higher for alkyl chains exceeding 15 carbons. They mainly based their claims on the decreasing CA hysteresis and shift of the CH_2 stretch vibrations to lower wavenumbers with increasing chain length. Also, the tilt angle was calculated from thickness values. They stated that an ordered monolayer should have a 30° tilt and only the molecules having >14 carbon atoms showed this value. The C/Ti and P/Ti XPS ratios were increasing and the Ti-OH/P ratios were decreasing, with increasing chain length. The authors explained this by the increase in the coverage and packing density of the monolayers with increasing chain length. Regarding the presence of P=O peaks in the XPS of the SAM samples, the authors concluded that tridendate bonding is not likely to occur. They proposed partial coverage for short alkyl chains in a bidentate mode, while for longer chains, a higher coverage was found with additionally monodentate coordinated molecules at the previously empty (Ti-OH) binding sites (Figure 2.7).
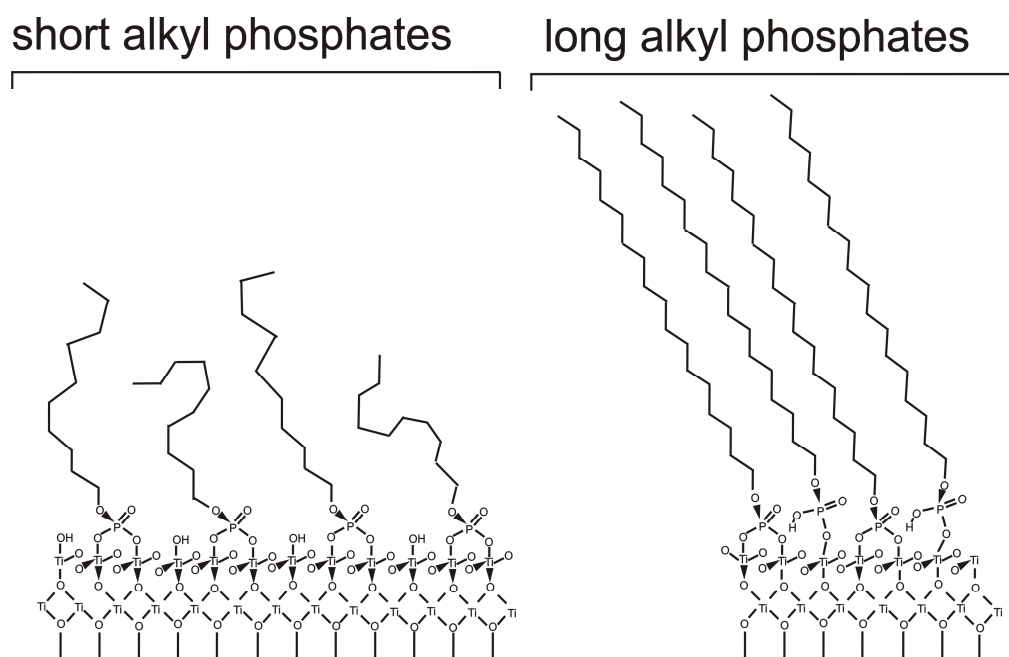
Figure 2.7 Sketch of the proposed binding structure for short (C10) and long (C18) alkyl phosphates self-assembled on TiO_2[60]

Gnauck *et al.* modified titanium oxide with carboxy-terminated oligo(ethylene glycol) (OEG)-alkylphosphate monolayers (Figure 2.8).[83] Based on the angle-resolved

XPS data they reported that the molecules were bound to the surface through the phosphate headgroup. Due to the low molecular density calculated from the ellipsometry data, they concluded that the monolayers were disordered and not densely packed.
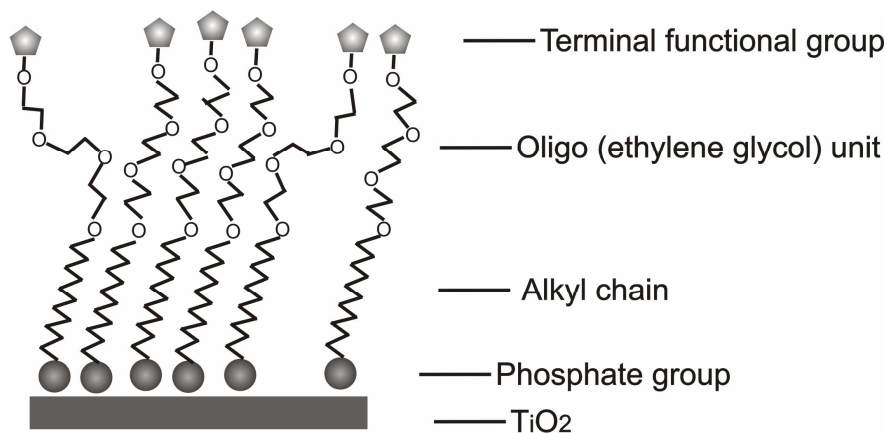
Figure 2.8 Structural model of the *w*-functionalized OEG alkylphosphate SAM on the titanium oxide substrate.[83]

Woodward *et al.* studied the formation of octadecylphosphonic acid (ODP) SAMs in situ by AFM.[84] They showed that the SAMs formed on mica by nucleation, growth and coalescence of submonolayer islands (Figure 2.9 a,b). The islands grew by aggregation at the edges which implied laying-down molecules at the lower parts. The presence of typical compact islands (Figure 2.9c) implied sufficient mobility of the ODP molecules to rearrange in order to minimize island perimeter, unlike silane-based SAMs which form fractal islands.
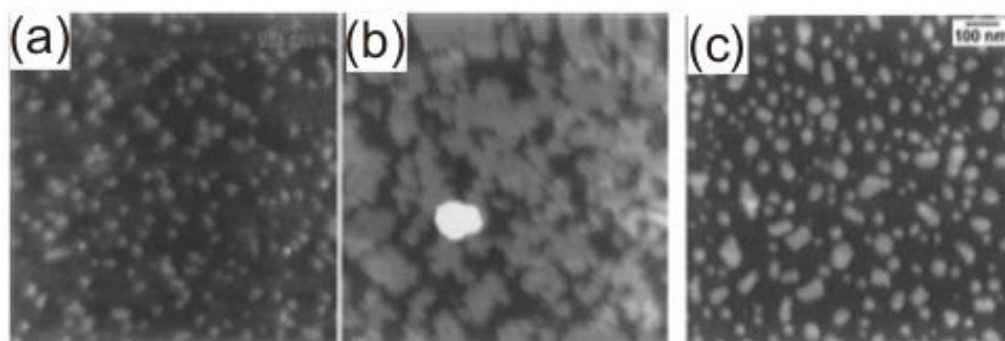
Figure 2.9 (a) AFM image obtained in situ during monolayer growth on mica in a 0.05 mM ODP solution after about 20 min of exposure. The higher areas (lighter shades of gray) correspond to submonolayer islands of ODP the tops of which are about 2 nm higher than the substrate. (b) AFM image of a different sample at a later stage of growth. The original islands have grown and coalesced. The large white particle near the center is typical of objects that were frequently seen in in situ images but were removed by rinsing since they were not observed on quenched films. They were often used as location markers during growth. (c) AFM image of a quenched monolayer that was exposed to 0.10 mM ODP in THF for 120 s.[84]

Messerschmidt *et al.*[30] found the growth characteristics of octadecylphosphonic acid SAM growth on single-crystal sapphire (α-Al_2O_3) to be highly dependent on temperature. At low temperature, growth occured as island growth, whereas at room temperature growth happened via a continuous liquid-phase film with elevated parts having poorly defined boundaries. At 15 $^{\circ}$C, both growth modes coexisted. FTIR spectra showed that during island growth at 2 $^{\circ}$C the peaks (C-H stretch region) remained in the same position, consistent with well-ordered alkyl chains, throughout film growth. However, at room temperature, the methylene stretch peak gradually shifted to lower wavenumbers, indicating a shift from disordered to ordered chains.

Kanta *et al.* investigated the growth and stability of octadecylphosphonic acid SAMs on smooth amorphous titania surfaces.[58] The water CA reached 110° in 16 h and no further increase was seen even after several days of immersion. The researchers showed that 18 h exposure to hexane, toluene and acetone had no effect on the SAMs. On the other hand, ethanol, methanol and water caused a decrease in CA. The authors explained this by the penetration of small molecular-volume solvents through the SAM. Air plasma and UV light exposure caused carbon-carbon chain

decomposition but did not affect phosphorus, as confirmed by XPS, which indicates the high stability of the phosphate-titanium bond. However, heat treatment at temperatures around 1000 ^{o}C caused the disappearence of phosphorus.

Alkylphosphonic acid-based SAMs show a high ambient stability. Sun *et al.* reported that the friction coefficient of decylphosphonic acid monolayers on aluminum oxide remained unchanged after 700 h ambient exposure.[85] Hoque *et al.* compared the tribological properties of bare and SAM–modified alumina.[40] Short (OP, C_8PO_3) and long chain (ODP, $C_{18}PO_3$) phosphonic acids were used as SAMs. Al_2O_3 had the highest friction coefficient while the long-chain SAM (ODP) had the lowest. Higher contact angle values and lower friction forces indicated that ODP forms a denser film than OP.

Foster *et al.* reported a lower friction coefficient for phosphonic acid SAMs compared to alkanoic acids with the same chain length, which shows that phosphonic acid monolayers are better ordered.[15]

Liakos et al. compared the resistance of phosphonic acid and alkanoic acid SAMs on aluminum oxide to acidic and basic solutions by using dynamic contact angle goniometry. Advancing and receding contact angle data were collected for each immersion cycle which lasted for 6 min.[28] They prepared acidic and basic solutions with deionized water using HCl and NaOH without buffer, to avoid phosphate and other species that could interfere with the process. They found that both SAMs were more stable under acidic conditions, however, phosphonic acid SAMs have a higher stability compared to alkanoic acid SAMs. The authors explained this with the stronger binding of PO_3 when compared to the binding of COOH with the substrate. An ODP ($C_{18}PO_3$) SAM had a hysteresis of 28° when compared to 50° for NDA ($C_{18}COOH$) which showed that an ODP SAM has a better packing, consistent with a higher water stability.

Pawsey *et al.* reported that carboxyalkylphosphonic acid (with 15 carbon atoms in its alkyl chain) binds ZrO_2 and TiO_2 preferentially through the phosphonic acid side showing the higher affinity of phosphonic acids to metal oxides when compared to alkanoic acids.[78]

Phosp(on)ate-based SAMs seem to dominate the other SAM types in terms of quality and stability and recent studies mainly consist of this type. The literature shows phosph(on)ate-based molecules to form more densely packed, more ordered and more stable SAMs on metal oxides when compared to alkanoic acid-based

molecules. There is a lack of studies which compare binding of phosphate and phosphonate-based SAMs.

2.3 Patterning of SAMs on metal oxides

There are few studies employing patterned SAMs on metal oxides, prepared by microcontact printing (µCP)[86-89] and photopatterning.[85, 90] Microcontact printing was used mainly because of ease of application and low cost. Typically, micron-size patterns were prepared and sometimes the pattern was transferred into the substrate by wet chemical etching.

Goetting *et al.* prepared octadecylphosphonic acid SAM patterns by microcontact printing on the native oxide surface of aluminum mounted on either a silicon or a silicon nitride-coated silicon support.[88] Patterns were visible after stamping and this indicated the formation of a multilayer. Excess ODP was rinsed off with 2-propanol as seen in Figure 2.10. Wet etching was done to selectively etch aluminum at the ODP-free regions. The line width was measured as the line width at half the thickness of the patterns by AFM. The line width of the PDMS stamp and the aluminum pattern were the same which indicates that the lateral resolution was maintained. The edge resolution of patterned aluminum was 150 nm, based on SEM images. For comparison they prepared aluminum patterns by photolithography and lift-off which resulted in an edge resolution of 50 nm. The lower limit of the patterns was not further investigated.
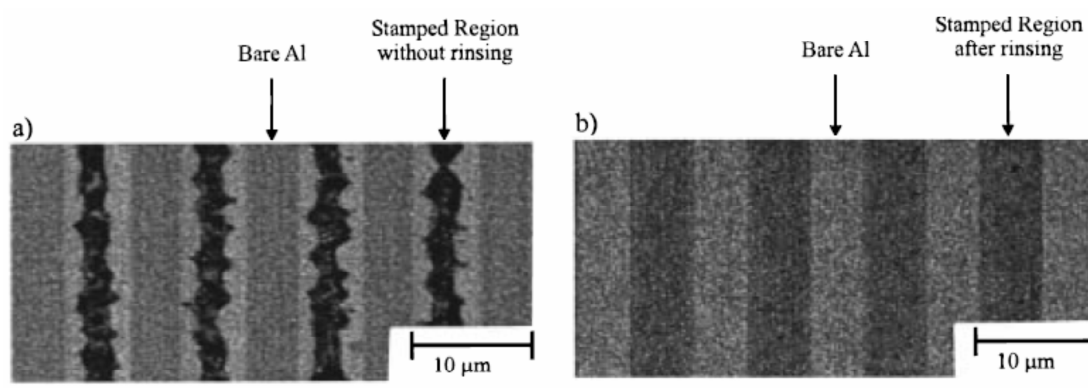
Figure 2.10 SEM images of ODP patterned by µCP on the native oxide of aluminum: (a) as stamped; (b) after rinsing the surface with 2-propanol to remove the excess of ODP. [88]

Sun *et al.* prepared micrometer and nanometer scale patterns of phosphonic acid-based SAMs on an aluminum oxide layer on aluminum-coated glass by photopatterning.[85] They used photopatterning mainly to cleave the C-P bond of SAM molecules and remove the alkyl chains, and also to prepare nanometer-scale patterns (see below). In Figure 2.11, a friction contrast of a mixed monolayer pattern is seen as prepared by exposing UV light through a photomask on an ODP-covered surface followed by filling the exposed areas with an amino-terminated phosphonic acid (ABP). Nanopatterns (~ 120 nm) were prepared by writing with a UV beam using a scanning near-field optical microscope on a SAM-covered surface. The unexposed regions were used as etch resists (Figure 2.12). Smaller features can potentially be prepared on gold with a similar technique as explained by the smaller grain size of the gold when compared to aluminum.
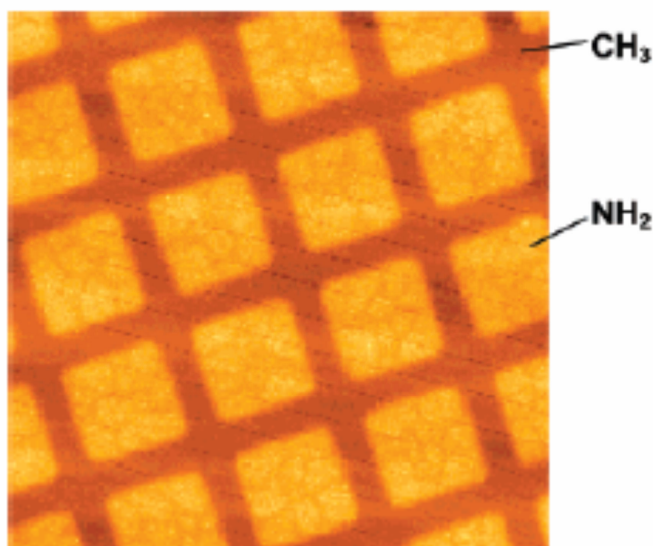
Figure 2.11 100x100 μm^2 friction force microscopy image of a patterned monolayer formed by exposure of a monolayer of octadecylphosphonic acid on Al_2O_3 to UV light for 5 min at a power of 100 mW through a photomask and subsequent immersion of the sample in a solution of aminobutylphosphonic acid in water.[85]

.
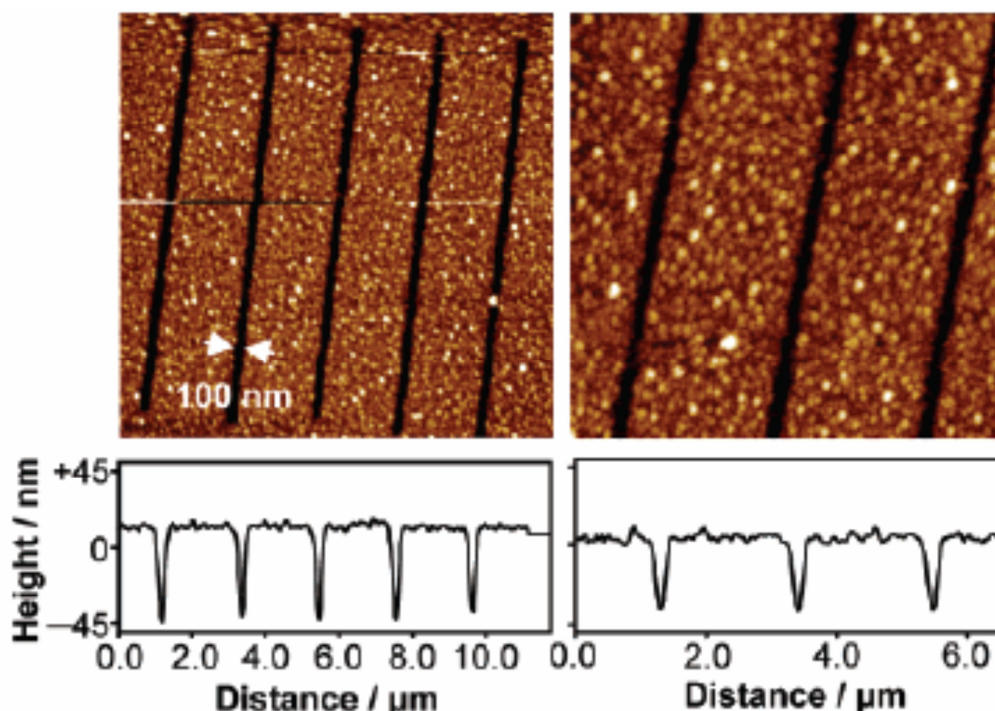
Figure 2.12. Tapping mode AFM images of nanostructures formed by using scanning near-field photolithography (SNP)-patterned phosphonic acid monolayers as resists for the wet etching of Al_2O_3.[85]

Phosph(on)ate-based SAM patterns can be prepared on metal oxide surfaces by microcontact printing and photopatterning, and the pattern can be transferred into the substrate by etching. SAMs do not seem to spread which enables lateral resolution stability during pattern transfer. Microcontact printing results in lower edge resolution when compared to photolithography. There is a lack of studies on SAM pattern preparation by nanoimprint lithography (NIL) on metal oxide substrates which would result in nano-features with high throughput.

2.4 Applications of SAMs on metal oxides

Phosph(on)ate-based SAMs have been used on metal oxide surfaces at several occasions for biomaterial[23, 59, 91-93] and electrical[25, 62-63, 94-96] applications, as etch resists[85, 87-88] and as wear inhibitors.[3]

Goetting *et al*. used octadecylphosphonic acid SAM patterns as etch resist on the native oxide surface of aluminum mounted on either a silicon or a silicon nitride-coated silicon support.[88] An etching solution was used which consisted of a combination of phosphoric, acetic and nitric acids and water in a ratio of 16:1:1:2.

The 3D AFM image shows the alumina pattern after wet etching, in which the elevated features were protected by the SAM (Figure 2.13). Prolonged etching resulted in overetching and decrease of the aluminum pattern thickness. The authors observed large circular defects on the etched pattern (>3 μm) which they explained by inadequate pattern transfer at stamping due to particles or air bubbles trapped between the PDMS stamp and the surface. They also observed small circular defects (~40 nm) in the SEM images, which remained unexplained.

The authors measured the resistance of the aluminum patterns as a function of pattern length, where the silicon nitride layer behaved as an insulator between aluminum and silicon. The results showed that the patterns were continuous and electrically conductive up to around 70 cm length and separated patterns were electrically isolated. To compare they prepared patterns with similar dimensions by photolithography and liftoff. The electrical measurement results were similar to the ones prepared by μCP and etching. They concluded that μCP of ODP is compatible with semiconductor device fabrication.
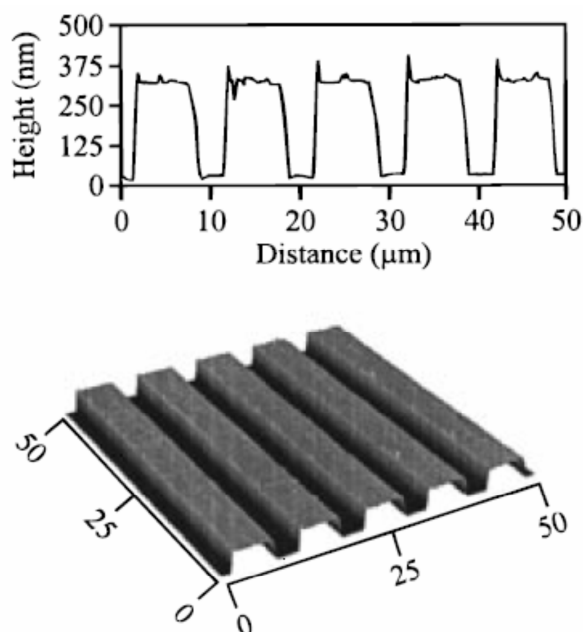
Figure 2.13 AFM image and profile of 300 nm thick aluminum, patterned by μCP of ODP, followed by baking for 10 min at 70 °C and wet etching at 35 °C.[88]

Danahy *et al.* modified the native oxide surface of Ti with diphosphonates further covered by zirconium complexes and a cell-attracting peptide derivative

(RGDC) as shown in Figure 2.14.[91] The surface loading of diphosphonates was found to be half of the loading of ODP, and IR showed that the layer was not ordered. The authors attributed this to the functional tail groups causing seperation of the chains by forming hydrogen-bonded networks. The use of diphosphonates brings the possibility of backbonding to the surface. The authors argued that this was not the case since P(2s) XPS signals had both free and surface bound-phosphonate components and IR spectra showed peaks assigned to P-O(bound) and P-O(free). The contact angle (45°) also confirmed PO_3-terminated films. As seen in Figure 2.15, the osteoblast cell growing rate on an RGDC-terminated surface is much higher than those on TiO_2 and on diphosphonic acid SAM-covered TiO_2.
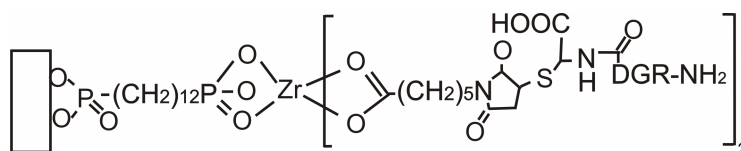
Figure 2.14 Modified titania surface with RGDC.[91]
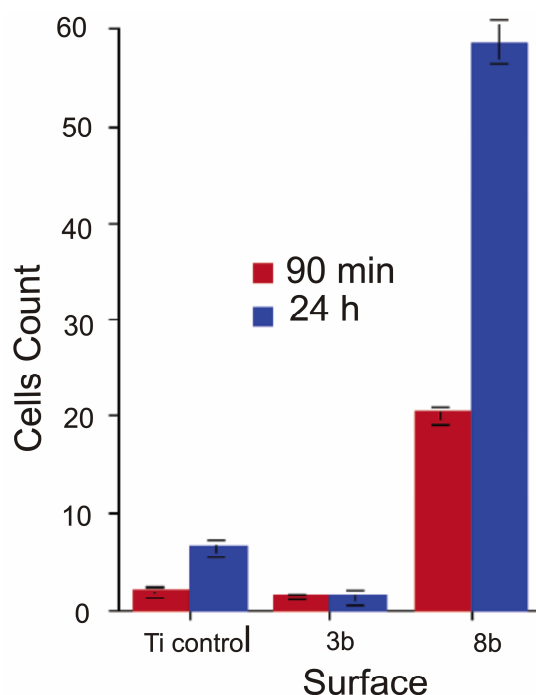
Figure 2.15 Cell counts for osteoblasts on (a) untreated TiO_2 control, (b) a diphosphonate 3(b) control, and (c) an RGD-modified surface (8b).[91]

Shannon *et al*. compared the mechanical properties of a diphosphonate SAM (SAMP), an RGD-functionalized SAM (cell attractive peptide) and hydroxyapatite (HA, natural constituent of bone) modified titanium implants 2, 4, 8, and 16 weeks after implantation.[59] The hystological results showed that more new bone formation was seen in case of SAMP and SAMP+RGD modification, compared to HA-coated implants. Apparently, SAMP and SAMP+RGD-modified implants had better mechanical properties compared to hydroxyapatite-coated ones which is accepted as the gold standard (Figure 2.16). They argued that SAMP provided an ordered, phosphate-like surface and might have facilitated bone growth similar to HA which also contains phosphate. They explained the poorer mechanical performance in case of HA compared to SAMP by the high roughness of the former. However, it was not explained how surface roughness would affect bone growth, implant fixation and mechanical properties. They also did not explain why SAMP+RGD modification gave similar results to SAMP modification. Contol experiments with an unmodified implant were not performed but it was mentioned that previous studies had shown that RGD coating enhanced fixation of Ti implants.
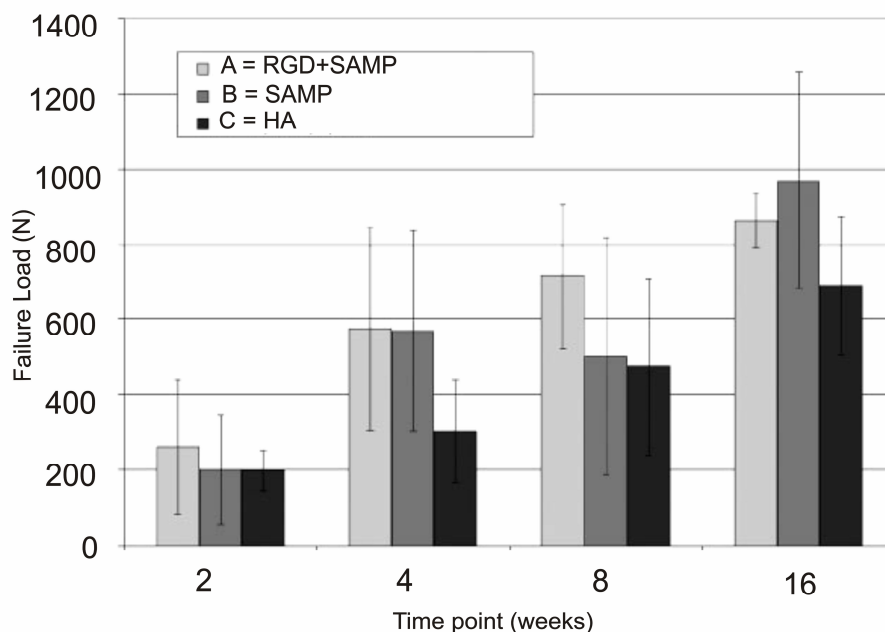
Figure 2.16 Load to failure of implants under tensile testing for titanium implants modified with SAMP+RGD, SAMP and HA.[59]

Zoulalian *et al*. prepared PEG-ylated compounds carrying phosphonate groups as binding sites to TiO_2 (Figure 2.17).[93] The substrates modified with **1**, **2** and **3**

showed much better stability against acidic and basic conditions compared to dodecylphosphate (DDPO$_4$) and PLL-g-PEG-modified reference systems due to a combined effect of multiple site attachment and presentation of PEG side chains, as explained by the authors. They used surfaces modified with **2** and **3** to prevent protein adsoption onto TiO$_2$ as shown in Figure 2.18.[93]
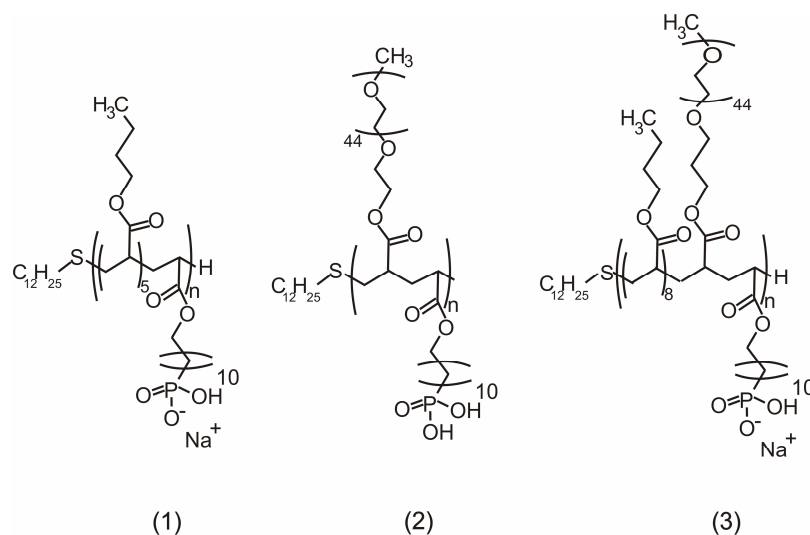
Figure 2.17 Synthesized alkylphosphonates based on statistic copolymerization: (1) copolymer C11/BMA, (2) copolymer C11/PEG, and (3) terpolymer C11/PEG/BMA.[93]
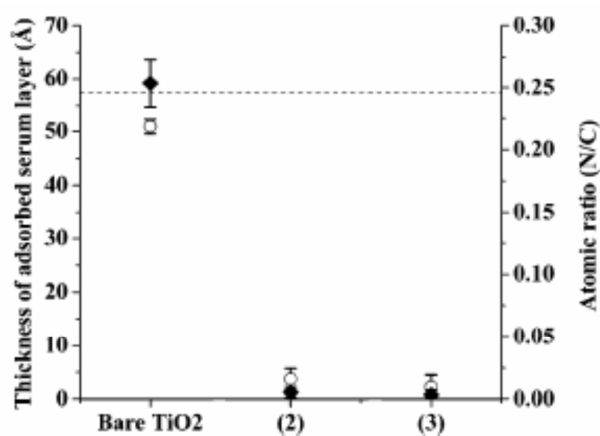
Figure 2.18 Protein adsorption to TiO$_2$ surfaces without and with a monolayer coating of polymers **2** and **3**, respectively, upon exposure to a HEPES buffer (4 h), full human serum solution (15 min) and subsequent rinsing in HEPES. The degree of protein adsorption was judged by (♦) the increase of layer thickness (ellipsometry) and (O) the atomic ratio N/C (XPS). The dashed line represents the N/C ratio calculated for albumin.[93]

Several studies have reported the modification of ITO with complex molecules having phosphonic acid binding sites[25, 62-63, 97] to control the interface between an organic semiconductor and inorganic electrodes and to improve the performance of OLEDs. Bardecker *et al.* used triarylamine-based hole-transporting molecules with PO$_3$ groups to form SAMs on an ITO surface.[25] Modified ITO was covered with a hole-transporting layer, a green-emitting polymer and electron-transporting layers to make OLED devices. The authors mentioned that SAM modification (Figure 2.19) resulted in a lowered turn-on voltage, an 18-fold increase in current density, and a 17-fold increase in brightness in case of TPD-3 when compared to bare ITO. The decrease in turn-on voltage, increase in current density and brightness were similar for TPD-1 and TPD-2, and were less than TPD-3 compared to bare ITO. The authors explained the better performance of TPD-3 compared to TPD-1 and TPD-2 with the strong hole-transport ability of this molecule since all three molecules had similar surface coverages and contact angle values.
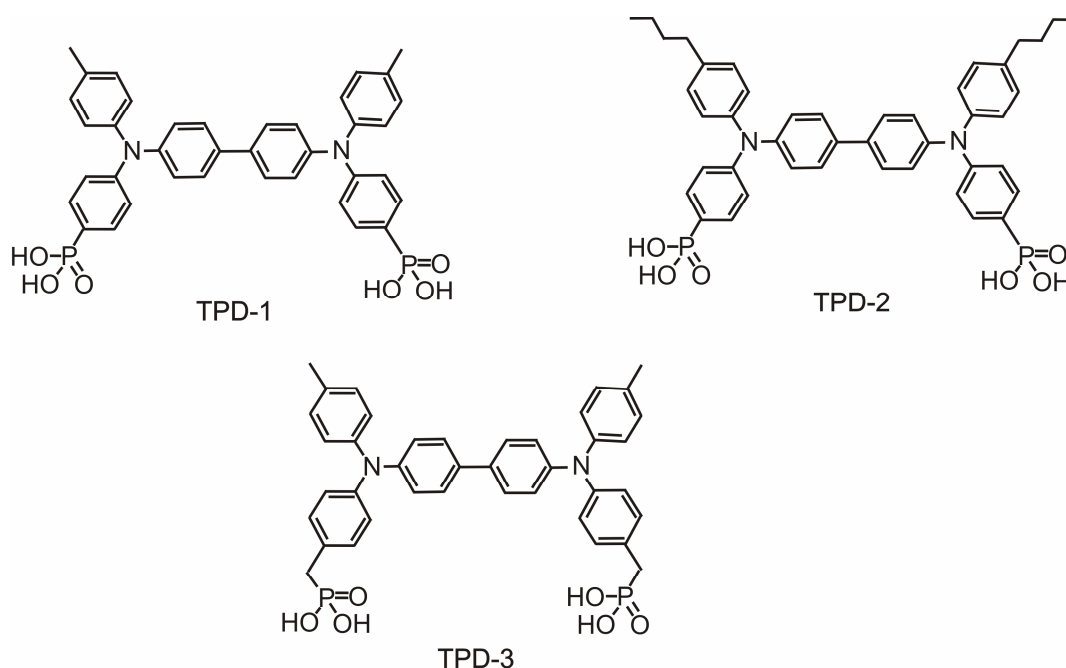
Figure 2.19 Molecules used for self-assembly on ITO.[25]

Phosph(on)ate-based SAMs have been used as a hybrid dielectric layer in combination with thin Al$_2$O$_3$[96] or HfO$_2$[95] to decrease the leakage current. Acton *et al.* modified a doped silicon surface covered with sol-gel HfO$_2$ with PO$_3$-based SAMs and prepared a pentacene-based transistor (Figure 2.20). They compared the leakage

current densities of bare SiO_2 with HfO_2 and $SAM+HfO_2$-modified ones. HfO_2 significantly decreased the leakage current compared to the bare silicon substrate (Figure 2.20). Addition of an ODP SAM on HfO_2 had a slight effect but the use of (π-σ-PA1) and (π-σ-PA2) SAMs resulted in a significant decrease in the leakage current compared to HfO_2 modification. The authors explained this by formation a more closely-packed SAM structure at (π-σ-PA1) and (π-σ-PA2) due to π-π interactions between anthryl end-groups and longer alkyl chains compared to ODP. The charge carrier properties improved with the use of SAMs with the order (π-σ-PA1) $\geq$(π-σ-PA2) > ODP. From that, the authors concluded that both the chemical compatibility and orientation of the end group were important to create a pentacene/dielectric interface.
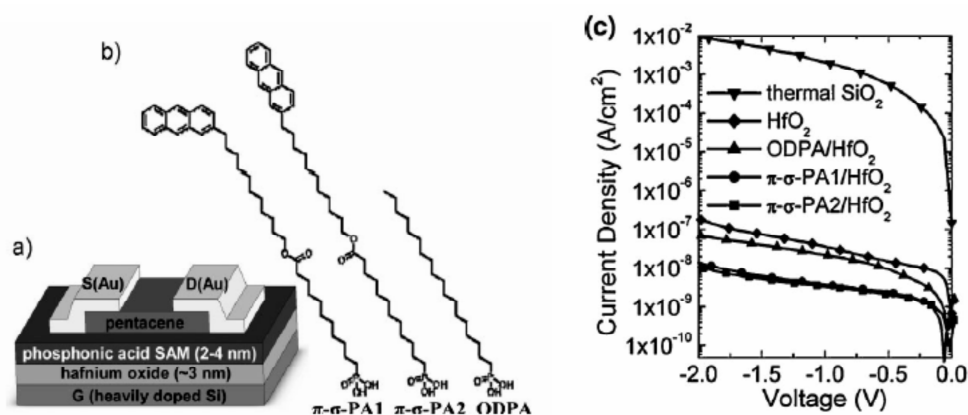
Figure 2.20 (a) Schematic view of top contact OTFT using PO_3-based SAM/hafnium oxide hybrid gate dielectrics. (b) Structures of SAMs used. (2-anthryl)undecoxycarbonyldecylphosphonic acid (π-σ-PA1), (2-anthryl)undecoxycarbonylundecylphosphonic acid (π-σ-PA2), and ODP. (c) leakage current density versus applied voltage.[95]

The literature shows that phosph(on)ate-based SAMs on metal oxides can effectively be used to protect the surface or to modify the surface properties at biomaterials or in electrical applications. The use of hybrid dielectric in electrical applications layers makes the interpretation of the contribution of the SAM layer difficult. The electrical blocking properties of SAMs on conducting oxide surfaces have not been thoroughly studied.

2.5 Conclusions

Phosp(on)ate-based SAMs on metal oxides dominate the other SAM types in terms of quality and stability. They form more densely packed, more ordered and more stable SAMs on metal oxides when compared to alkanoic acid-based molecules. There is a lack of studies which compare the binding of phosphate and phosphonate-based SAMs. Phosph(on)ate-based SAM patterns can be prepared on metal oxide surfaces by microcontact printing and photopatterning, and the pattern can be transferred by etching. However, the edge resolution in case of microcontact printing is less. There is a lack of studies on SAM pattern preparation by nanoimprint lithography (NIL) on metal oxide substrates which would result in nano features with high throughput. Phosph(on)ate-based SAMs are effective etch resists. With proper selection of chemical structure they can facilitate cell growth or prevent protein absorption at biomaterial applications. They can be used to improve the properties of OLED devices by improving the interface properties between the organic and inorganic electrodes. They can be used as additional dielectric layers at electrical applications, however the use of hybrid dielectric layers makes the assessment of the contribution of the SAM layer difficult. The electrical blocking properties of SAMs on conducting oxide surfaces have not been thoroughly studied. There is also a lack of studies to make reliable metal top contacts directly on phosph(on)ate based-SAMs for electrical applications. Moreover, there are not many studies on the use of SAMs as linkers to add functional nanoparticles or molecules to metal oxide surfaces.

2.6 References

1. Schreiber, F., *Progr. Surf. Sci.* **2000,** *65*, 151.
2. Onclin, S.; Ravoo, B. J.; Reinhoudt, D. N., *Angew. Chem. Int. Ed.* **2005,** *44*, 6282.
3. Wang, J. Q.; Yang, S. R.; Chen, M.; Xue, Q. J., *Surf. Coat. Technol.* **2004,** *176*, 229.
4. Silberzan, P.; Leger, L.; Ausserre, D.; Benattar, J. J., *Langmuir* **1991,** *7*, 1647.
5. Kropman, B. L.; Blank, D. H. A.; Rogalla, H., *Langmuir* **2000,** *16*, 1469.
6. Mitchon, L. N.; White, J. M., *Langmuir* **2006,** *22*, 6549.
7. Wang, D. H.; Ni, Y. H.; Huo, Q.; Tallman, D. E., *Thin Solid Films* **2005,** *471*, 177.
8. Yasseri, A. A.; Kobayashi, N. P.; Kamins, T. I., *Appl. Phys. A-Mater.* **2006,** *84*, 1.
9. Abelev, E.; Starosvetsky, D.; Ein-Eli, Y., *Langmuir* **2007,** *23*, 11281.
10. Allara, D. L.; Nuzzo, R. G., *Langmuir* **1985,** *1*, 45.
11. Allara, D. L.; Nuzzo, R. G., *Langmuir* **1985,** *1*, 52.

12. Aronoff, Y. G.; Chen, B.; Lu, G.; Seto, C.; Schwartz, J.; Bernasek, S., *J. Am. Chem. Soc.* **1997,** *119*, 259.
13. Chen, S. H.; Frank, C. W., *Langmuir* **1989,** *5*, 978.
14. Dote, J. L.; Mowery, R. L., *J. Phys. Chem.* **1988,** *92*, 1571.
15. Foster, T. T.; Alexander, M. R.; Leggett, G. J.; McAlpine, E., *Langmuir* **2006,** *22*, 9254.
16. Lim, M. S.; Feng, K.; Chen, X. Q.; Wu, N. Q.; Raman, A.; Nightingale, J.; Gawalt, E. S.; Korakakis, D.; Hornak, L. A.; Timperman, A. T., *Langmuir* **2007,** *23*, 2444.
17. Oberg, K.; Persson, P.; Shchukarev, A.; Eliasson, B., *Thin Solid Films* **2001,** *397*, 102.
18. Pawsey, S.; Yach, K.; Halla, J.; Reven, L., *Langmuir* **2000,** *16*, 3294.
19. Pertays, K. M.; Thompson, G. E.; Alexander, M. R., *Surf. Interf. Anal.* **2004,** *36*, 1361.
20. Tao, Y. T., *J. Am. Chem. Soc.* **1993,** *115*, 4350.
21. Taylor, C. E.; Schwartz, D. K., *Langmuir* **2003,** *19*, 2665.
22. Thompson, W. R.; Pemberton, J. E., *Langmuir* **1995,** *11*, 1720.
23. Amalric, J.; Mutin, P. H.; Guerrero, G.; Ponche, A.; Sotto, A.; Lavigne, J. P., *J Mater. Chem.* **2009,** *19*, 141.
24. Ball, J. M.; Wobkenberg, P. H.; Colleaux, F.; Heeney, M.; Anthony, J. E.; McCulloch, I.; Bradley, D. D. C.; Anthopoulos, T. D., *Appl. Phys. Lett.* **2009,** *95*.
25. Bardecker, J. A.; Ma, H.; Kim, T.; Huang, F.; Liu, M. S.; Cheng, Y. J.; Ting, G.; Jen, A. K. Y., *Adv. Funct. Mater.* **2008,** *18*, 3964.
26. Gawalt, E. S.; Avaltroni, M. J.; Koch, N.; Schwartz, J., *Langmuir* **2001,** *17*, 5736.
27. Liakos, I. L.; McAlpine, E.; Chen, X. Y.; Newman, R.; Alexander, M. R., *Appl. Surf. Sci.* **2008,** *255*, 3276.
28. Liakos, I. L.; Newman, R. C.; McAlpine, E.; Alexander, M. R., *Langmuir* **2007,** *23*, 995.
29. McIntyre, N. S.; Nie, H. Y.; Grosvenor, A. P.; Davidson, R. D.; Briggs, D., *Surf. Interf. Anal.* **2005,** *37*, 749.
30. Messerschmidt, C.; Schwartz, D. K., *Langmuir* **2001,** *17*, 462.
31. Textor, M.; Ruiz, L.; Hofer, R.; Rossi, A.; Feldman, K.; Hahner, G.; Spencer, N. D., *Langmuir* **2000,** *16*, 3257.
32. Tosatti, S.; Michel, R.; Textor, M.; Spencer, N. D., *Langmuir* **2002,** *18*, 3537.
33. Folkers, J. P.; Gorman, C. B.; Laibinis, P. E.; Buchholz, S.; Whitesides, G. M.; Nuzzo, R. G., *Langmuir* **1995,** *11*, 813.
34. Hozumi, A.; Kim, B.; McCarthy, T. J., *Langmuir* **2009,** *25*, 2875.
35. Xu, Z. H.; Ducker, W.; Israelachvili, J., *Langmuir* **1996,** *12*, 2263.
36. Huang, N. P.; Michel, R.; Voros, J.; Textor, M.; Hofer, R.; Rossi, A.; Elbert, D. L.; Hubbell, J. A.; Spencer, N. D., *Langmuir* **2001,** *17*, 489.
37. Eschner, M.; Frenzel, R.; Simon, F.; Pleul, D.; Uhlmann, P.; Adler, H., *Macromol. Symp.* **2004,** *210*, 77.
38. Esumi, K.; Fujimoto, N.; Torigoe, K., *Langmuir* **1999,** *15*, 4613.
39. Hauffman, T.; Blajiev, O.; Snauwaert, J.; van Haesendonck, C.; Hubin, A.; Terryn, H., *Langmuir* **2008,** *24*, 13450.
40. Hoque, E.; DeRose, J. A.; Kulik, G.; Hoffmann, P.; Mathieu, H. J.; Bhushan, B., *J. Phys. Chem. B* **2006,** *110*, 10855.

41. Jeon, J. S.; Sperline, R. P.; Raghavan, S.; Hiskey, J. B., *Coll. Surf. A* **1996**, *111*, 29.
42. Koutsioubas, A. G.; Spiliopoulos, N.; Anastassopoulos, D. L.; Vradis, A. A.; Priftis, G. D., *Surf. Interf. Anal.* **2009**, *41*, 897.
43. Maege, I.; Jaehne, E.; Henke, A.; Adler, H. J. P.; Bram, C.; Jung, C.; Stratmann, M., *Prog. Org. Coat.* **1998**, *34*, 1.
44. Nie, H. Y., *Anal. Chem.* **2010**, *82*, 3371.
45. Nie, H. Y.; Walzak, M. J.; McIntyre, N. S., *J. Phys. Chem. B* **2006**, *110*, 21101.
46. Pellerite, M. J.; Dunbar, T. D.; Boardman, L. D.; Wood, E. J., *J Phys. Chem. B* **2003**, *107*, 11726.
47. Sekitani, T.; Yokota, T.; Zschieschang, U.; Klauk, H.; Bauer, S.; Takeuchi, K.; Takamiya, M.; Sakurai, T.; Someya, T., *Science* **2009**, *326*, 1516.
48. Thissen, P.; Wielant, J.; Köyer, M.; Toews, S.; Grundmeier, G., *Surf. Coat. Tech.* **2010**, *204*, 3578.
49. Tsud, N.; Yoshitake, M., *Surf. Sci.* **2007**, *601*, 3060.
50. Wobkenber, P. H.; Ball, J.; Kooistra, F. B.; Hummelen, J. C.; de Leeuw, D. M.; Bradley, D. D. C.; Anthopoulos, T. D., *Appl. Phys. Lett.* **2008**, *93*.
51. Adadi, R.; Zorn, G.; Brener, R.; Gotman, I.; Gutmanas, E. Y.; Sukenik, C. N., *Thin Solid Films* **2010**, *518*, 1966.
52. Adolphi, B.; Jahne, E.; Busch, G.; Cai, X. D., *Anal. Bioanal. Chem.* **2004**, *379*, 646.
53. Bozzini, S.; Petrini, P.; Tanzi, M. C.; Zurcher, S.; Tosatti, S., *Langmuir* **2010**, *26*, 6529.
54. Ferreira, J. M.; Marcinko, S.; Sheardy, R.; Fadeev, A. Y., *J. Coll. Interf. Sci.* **2005**, *286*, 258.
55. Gawalt, E. S.; Lu, G.; Bernasek, S. L.; Schwartz, J., *Langmuir* **1999**, *15*, 8929.
56. Guerrero, G.; Mutin, P. H.; Vioux, A., *Chem. Mater.* **2001**, *13*, 4367.
57. Hahner, G.; Hofer, R.; Klingenfuss, I., *Langmuir* **2001**, *17*, 7047.
58. Kanta, A.; Sedev, R.; Ralston, J., *Coll. Surf. A* **2006**, *291*, 51.
59. Shannon, F. J.; Cottrell, J. N.; Deng, X. H.; Crowder, K. N.; Doty, S. B.; Avaltroni, M. J.; Warren, R. F.; Wright, T. M.; Schwartz, J., *J. Biomed. Mater. Res. Part A* **2008**, *86A*, 857.
60. Spori, D. M.; Venkataraman, N. V.; Tosatti, S. G. P.; Durmaz, F.; Spencer, N. D.; Zurcher, S., *Langmuir* **2007**, *23*, 8053.
61. Zwahlen, M.; Tosatti, S.; Textor, M.; Hahner, G., *Langmuir* **2002**, *18*, 3957.
62. Besbes, S.; Ben Ouada, H.; Davenas, J.; Ponsonnet, L.; Jaffrezic, N.; Alcouffe, P., *Mater. Sci. Eng. C-Biomim.* **2006**, *26*, 505.
63. Hanson, E. L.; Guo, J.; Koch, N.; Schwartz, J.; Bernasek, S. L., *J. Am. Chem. Soc.* **2005**, *127*, 10058.
64. Paramonov, P. B.; Paniagua, S. A.; Hotchkiss, P. J.; Jones, S. C.; Armstrong, N. R.; Marder, S. R.; Bredas, J. L., *Chem. Mater.* **2008**, *20*, 5131.
65. Hoque, E.; DeRose, J. A.; Bhushan, B.; Hipps, K. W., *Ultramicroscopy* **2009**, *109*, 1015.
66. Van Alsten, J. G., *Langmuir* **1999**, *15*, 7605.
67. Felhosi, I.; Telegdi, J.; Palinkas, G.; Kalman, E., *Electrochim. Acta* **2002**, *47*, 2335.
68. Jiang, S. Y.; Frazier, R.; Yamaguchi, E. S.; Blanco, M.; Dasgupta, S.; Zhou, Y. H.; Cagin, T.; Tang, Y. C.; Goddard, W. A., *J. Phys. Chem. B* **1997**, *101*, 7702.
69. Kaufmann, C. R.; Mani, G.; Marton, D.; Johnson, D. M.; Agrawal, C. M., *Biomed. Mater.* **2010**, *5*.

70. Paszternak, A.; Felhosi, I.; Paszti, Z.; Kuzmann, E.; Vertes, A.; Kalman, E.; Nyikos, L., *Electrochim. Acta* **2010,** *55*, 804.
71. Raman, A.; Dubey, M.; Gouzman, I.; Gawalt, E. S., *Langmuir* **2006,** *22*, 6469.
72. Hofer, R.; Textor, M.; Spencer, N. D., *Langmuir* **2001,** *17*, 4014.
73. D'Andrea, S. C.; Iyer, K. S.; Luzinov, I.; Fadeev, A. Y., *Coll. Surf. B-Biointerfaces* **2003,** *32*, 235.
74. Quinones, R.; Gawalt, E. S., *Langmuir* **2007,** *23*, 10123.
75. Quinones, R.; Gawalt, E. S., *Langmuir* **2008,** *24*, 10858.
76. Gao, W.; Dickinson, L.; Grozinger, C.; Morin, F. G.; Reven, L., *Langmuir* **1996,** *12*, 6429.
77. Gao, W.; Dickinson, L.; Grozinger, C.; Morin, F. G.; Reven, L., *Langmuir* **1997,** *13*, 115.
78. Pawsey, S.; Yach, K.; Reven, L., *Langmuir* **2002,** *18*, 5205.
79. Yim, C. T.; Pawsey, S.; Morin, F. G.; Reven, L., *J. Phys. Chem. B* **2002,** *106*, 1728.
80. Schwartz, J.; Avaltroni, M. J.; Danahy, M. P.; Silverman, B. M.; Hanson, E. L.; Schwarzbauer, J. E.; Midwood, K. S.; Gawalt, E. S., *Mater. Sci. Eng. C-Biomim.* **2003,** *23*, 395.
81. Gouzman, I.; Dubey, M.; Carolus, M. D.; Schwartz, J.; Bernasek, S. L., *Surf. Sci.* **2006,** *600*, 773.
82. Pawsey, S.; McCormick, M.; De Paul, S.; Graf, R.; Lee, Y. S.; Reven, L.; Spiess, H. W., *J. Am. Chem. Soc.* **2003,** *125*, 4174.
83. Gnauck, M.; Jaehne, E.; Blaettler, T.; Tosatti, S.; Textor, M.; Adler, H. J. P., *Langmuir* **2007,** *23*, 377.
84. Woodward, J. T.; Schwartz, D. K., *J. Am. Chem. Soc.* **1996,** *118*, 10944.
85. Sun, S. Q.; Leggett, G. J., *Nano Lett* **2007,** *7*, 3753.
86. Breen, T. L.; Fryer, P. M.; Nunes, R. W.; Rothwell, M. E., *Langmuir* **2002,** *18*, 194.
87. Burdinski, D.; Saalmink, M.; Van den Berg, J.; Van der Marel, C., *Angew Chem. Int. Ed.* **2006,** *45*, 4355.
88. Goetting, L. B.; Deng, T.; Whitesides, G. M., *Langmuir* **1999,** *15*, 1182.
89. Lim, H. J.; Lee, D. Y.; Oh, Y. J., *Sens. Actuat. A-Phys.* **2006,** *125*, 405.
90. Tizazu, G.; Adawi, A. M.; Leggett, G. J.; Lidzey, D. G., *Langmuir* **2009,** *25*, 10746.
91. Danahy, M. P.; Avaltroni, M. J.; Midwood, K. S.; Schwarzbauer, J. E.; Schwartz, J., *Langmuir* **2004,** *20*, 5333.
92. Zoulalian, V.; Zurcher, S.; Tosatti, S.; Textor, M.; Monge, S.; Robin, J. J., *Langmuir* **2010,** *26*, 74.
93. Zoulalian, V.; Monge, S.; Zurcher, S.; Textor, M.; Robin, J. J.; Tosatti, S., *J. Phys. Chem. B* **2006,** *110*, 25603.
94. Acton, B. O.; Ting, G. G.; Shamberger, P. J.; Ohuchi, F. S.; Ma, H.; Jen, A. K. Y., *ACS Appl. Mater. Interf.* **2010,** *2*, 511.
95. Acton, O.; Ting, G.; Ma, H.; Ka, J. W.; Yip, H. L.; Tucker, N. M.; Jen, A. K. Y., *Adv. Mater.* **2008,** *20*, 3697.
96. Klauk, H.; Zschieschang, U.; Pflaum, J.; Halik, M., *Nature* **2007,** *445*, 745.
97. Koh, S. E.; McDonald, K. D.; Holt, D. H.; Dulcey, C. S.; Chaney, J. A.; Pehrsson, P. E., *Langmuir* **2006,** *22*, 6249.

Chapter 3

Structural Characterization of Self Assembled Monolayers on Metal Oxides

Abstract

Phosph(on)ate-based self-assembled monolayers (SAMs) with CH_3, NH_2, SH, COOH terminations were prepared on single crystalline aluminum oxide (Al_2O_3) substrates. As a result, SAMs with homogeneous coverage, tails-up orientation and a certain degree of order is reproducibly obtained. A shift is observed in the X-ray photoelectron spectroscopy (XPS) P peak upon tetradecylphosphate (TDP) SAM formation on Al_2O_3 indicating charge transfer from the substrate to the phosphate headgroup. The thickness of a TDP layer is smaller than the length of an extended TDP molecule suggesting a tilt in the layer. There is no indication of in-plane registry between the surface atoms of substrates and phosph(on)ate headgroup. The TDP molecules desorbed upon immersion in water, but they are stable in organic solvents. To create chemically different regions, SAM patterns were prepared on Al_2O_3 by microcontact printing. The results indicate that the modification of metal oxide substrates with active terminated SAMs can be used for adding new functionalities to the oxide surface.

3.1 Introduction

Self–assembled monolayers (SAMs) may be defined as ordered molecular assemblies formed spontaneously by the adsorption of a surfactant with a specific affinity of its headgroup to a substrate.[1] Although SAMs are extremely thin (typically 2 nm) they are effective tools to change the surface properties [1-4] due to their chemically well controlled and structurally ordered properties. SAMs, in particular thiols on gold and silanes on SiO_2, have been studied extensively[1, 3] but SAMs on metal oxides are relatively less studied.

Alkylphosphates and alkylphosphonates form SAMs with high ambient stability on metal oxides such as Ta_2O_5 etc. without the need for controlled environmental conditions.[5-12] On the other hand, siloxanes easily polymerize resulting in a lack of order[7, 11] and need precise control over the environment during deposition. n-Alkanoic acids have weaker interactions than phosph(on)tes with the metal oxides.[8, 10] Thus, in this study, phosph(on)ates are selected as organic molecules to prepare SAMs on metal oxides.

Metal oxides have interesting electronic, optical and magnetic properties such as insulating, semiconducting, metallic, superconducting, ferroelectric, piezoelectric, ferromagnetic, etc.[13-16] To study SAMs on metal oxides, we have chosen aluminum oxide (Al_2O_3) as a model substrate. It is an important substrate because it is frequently used as dielectric material in electronic device fabrication.[11, 17-21] It has many crystalline faces available and the surface properties can easily be changed by annealing to get an ultra-smooth surface. [9, 22] The atomically flat surface may stimulate the epitaxial growth of the organic layer, resulting in an ultra-smooth SAM.

While most of the studies on binding of phosph(on)ates were done on metal oxide powders[10] or on amorphous metal oxides deposited on SiO_2[7-8, 11-12] we will focus on single crystalline substrates. The FTIR data and high hysteresis between advancing and receding CA values[5, 7-8, 12, 23-24] reported on alkyl phosph(on)ate monolayers on metal oxide surfaces suggest more disordered monolayers compared to thiols on gold. Although there have been several mechanisms proposed for the phosph(on)ates binding to the metal oxides, the binding mechanism is still not completely understood partly due to the wide range of binding possibilities from mono to tri-dentate. As generally agreed on, phosph(on)ates adsorb onto the surface through hydrogen bonding or electrostatic interactions between a deprotonated headgroup and the surface metal, followed by condensation[11, 24-25]or formation of a

surface coordination complex.[12] So far, there are few studies employing functional terminated SAMs to activate the metal oxides[11, 26] and on patterning of metal oxides by SAMs.[27-31]

Some questions that will be adressed in this study are: what is coverage, packing and orientation of phosph(on)ate-based SAMs on Al_2O_3? What is the thickness, tilt and configuration of the molecules? What is the effect of the chain length on structural properties? Is there in-plane registry between the phosphate headgroups and the crystalline surface? What is the morphology of the SAM-modified surfaces? Is there a difference between phosphate (PO_4) and phosphonate (PO_3)-based SAMs? What are the interactions between the substrate and the phosphate headgroup? What is the stability of the SAM? To address these questions the assembly of TDP on Al_2O_3 was studied. Microcontact printing was employed to pattern metal oxide substrates.

3.2 Results and discussion

3.2.1 SAM formation and basic characterization

Figure 3.1 shows the organic molecules which are used to prepare SAMs on metal oxide surfaces. Tetradecylphosphate acid (TDP) and octadecylphosphonic acid (ODP) have methyl ($-CH_3$) end groups, which form a hydrophobic layer while 11-phosphonoundecanoic acid (PUD), mercaptoundecylphosphonic acid (MUP) and aminobutylphosphonic acid (ABP) have carboxylic acid (-COOH), thiol (-SH) and amino ($-NH_2$) functionalities respectively.
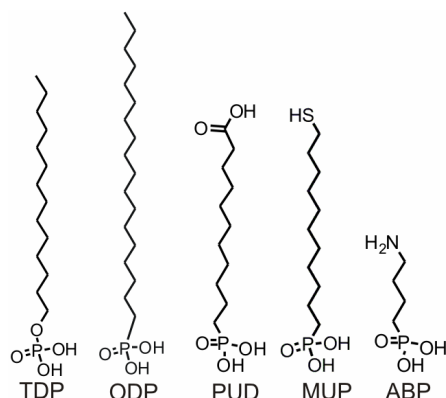

Figure 3.1 Alkylphosph(on)ates used: tetradecylphosphate (TDP), octadecylphosphonic acid (ODP), 11-phosphonoundecanoic acid (PUD), mercaptoundecylphosphonic acid (MUP) and aminobutylphosphonic acid (ABP).

The preparation and characterization of monolayer-modified Al_2O_3 substrates was performed according to procedures reported in the literature.[5-6, 8-12] It is important to have a well defined cleaning procedure to have SAMs with good properties. CA and FTIR did not suggest a difference between TDP SAMs prepared from oxygen plasma-cleaned or annealed substrates other than morphological differences. Annealing was performed when well-defined terraces and step edges are needed, otherwise oxygen plasma cleaning was used. Cleaned Al_2O_3 substrates were immersed into solutions of ABP, PUD, MUP, ODP or TDP for 2 days at room temperature, rinsed afterwards with solvent and dried under a flow of N_2 to yield amino-, carboxylic acid-, thiol- and methyl-functionalized substrates, respectively. CA goniometry is a crude but quite powerful tool to estimate the properties such as coverage and order of SAMs. The water contact angle of oxygen plasma-cleaned or annealed Al_2O_3 was below 10° which increased to 70°, 60°, 87°, 115° and 115° for SAMs of ABP, PUD, MUP, TDP and ODP, respectively. The high CA value (115°) of TDP and ODP SAMs indicates the quite hydrophobic surface which confirms a CH_3 termination.[7-8] We observed hysteresis of about 45° between advancing and receding CA values of TDP SAMs on Al_2O_3. These hystereses indicate a relatively disordered layer.[32] Thus, SAMs on metal oxide surfaces are more disordered than alkyl thiols on gold.

Figure 3.2 shows atomic force microscopy (AFM) images of SAM-functionalized and bare alumina surfaces. As clearly seen in Figure 3.2a and 3.2b thermal annealing of an alumina substrate results in well-defined step edges and smooth surfaces. On both annealed and unannealed samples, TDP SAM formation follows the surface topography faithfully, the step edges remain clearly visible, and the step height (0.3 nm) remains the same. This confirms homogeneous and full SAM formation. The same was also observed in case of MUP, PUD and ABP SAMs which have thiol, carboxylic acid and amino endgroups, respectively (data not shown). SAM formation of TDP on other substrates (TiO_2, STO, LAO, LSMO) gave similar FTIR, CA and AFM results (data not shown). Also, SAM formation of TDP on Al_2O_3 achieved by microcontact printing (µCP) using a flat PDMS stamp provided a similar layer quality.
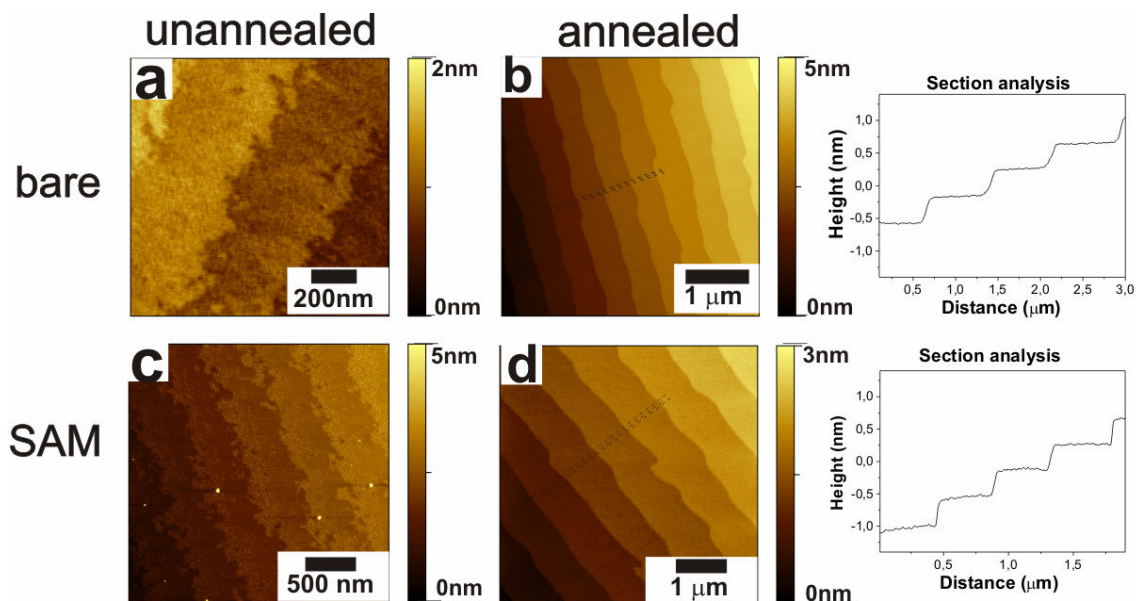
Figure 3.2 AFM height images of blank and SAM-functionalized Al_2O_3 surfaces (a) blank, unannealed. (b) blank, annealed at 1000 ^{o}C for 2 h. (c) TDP SAM on unannealed alumina. (d)TDP SAM on annealed alumina.
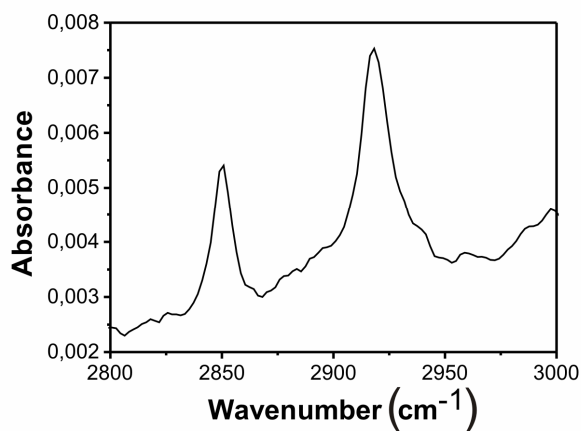
Figure 3.3 FTIR of aTDP SAM on an Al_2O_3 substrate

Fourier transform infrared spectroscopy (FTIR) was performed by scanning a TDP SAM-covered alumina substrate and subtracting the background signal of bare alumina. The spectrum (Figure 3.3) shows the CH_2 asymmetric and symmetric stretch vibrations of the alkyl chains around 2919 and 2851 cm^{-1}, respectively. In line with the relatively high hysteresis between advancing and receding contact angle values, these are indications of the semicrystalline character of the alkyl chains.[5, 33]

Al$_2$O$_3$ has several crystal faces, each having different atomic configuration and different surface energy.[9] To observe the effect of different atomic configuration and the crystal face on SAM quality and to see if there is a registry between the surface atomic configuration and PO$_4$ headgroup, TDP SAMs were prepared on C and R-faces of Al$_2$O$_3$ which have different Al interspacings. AFM, CA and FTIR did not indicate any difference on the quality of SAMs on the two crystal faces. No difference was found between alkyl phosphate SAMs with chain lengths of 14, 16 or 18 on Al$_2$O$_3$ (not shown). Also, there was no difference regarding the structural properties between phosphate and phosphonate based SAMs on Al$_2$O$_3$.

3.2.2 XPS analysis of TDP SAMs on alumina

XPS measurements proved that all the expected elements were present on the surface for all SAMs and in the expected ratios except for ABP which had more carbon content probably due to contamination in air (Table 3.1). Bulk TDP (C$_{14}$PO$_4$), as

Table 3.1 Selected XPS data of bulk TDP and of SAMs on Al$_2$O$_3$ substrates.

SAM	C%/P%	N%/P%	S%/P%
TDP$_{bulk}$(C$_{14}$PO$_4$)	13	-	-
TDP (C$_{14}$PO$_4$)	15	-	-
ODP (C$_{18}$PO$_3$)	19	-	-
MUP(SC$_{11}$PO$_3$)	12	-	0.6
PUD(C$_{11}$PO$_5$)	11	-	-
ABP (C$_4$NPO$_3$)	12	0.8	-

reference and a TDP SAM, assembled on alumina from a 0.125 mM TDP solution in hexane:isopropanol by 2 days immersion, was analysed by XPS. In Figure 3.4 curve fittings of elements at alumina, TDP, TDP SAM on alumina and in Table 3.2 binding energies obtained from the curve fittings are shown. The binding energies correspond the literature values which shows the succesful SAM formation.[12, 20, 34]

Table 3.2 XPS binding energies of elements in Al_2O_3, TDP and TDP SAMs on alumina

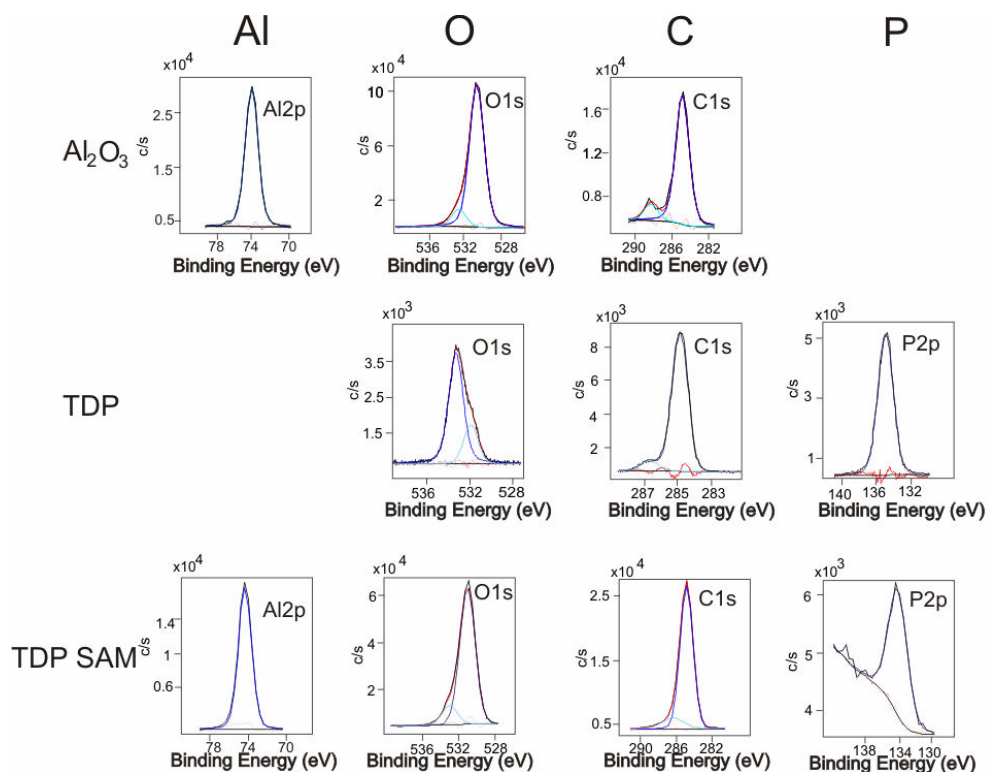| Elements	Binding Energy (eV)		
	TDP	Al_2O_3	TDP on Al_2O_3
Al2p		73.9	74.3
P2p	135.0		134.1
O1s -1		530,5	531.0
O1s -2		532.3 (minor)	
O1s-3	532.1(minor)		
O1s-4	533.4		533.0
C1s	284.9	284.9	284.7
	286.5(minor)	288.5(minor)	286.2

Figure 3.4 XPS curve-fittings of Al, O, C and P for Al_2O_3, TDP bulk and TDP SAM on alumina.

For bulk TDP, element ratios were 13.3:3.7:1, and thus in agreement with the expected C:O:P ratio of 14:4:1. The O1s curve is fitted with two curves, the small

peak (532.1 eV) is very close to the small peak of O1s at alumina (532.3) but the major peaks of O1s at TDP (533.4 eV) and alumina (530.5 eV) have distinct values which makes it possible to distinguish between the contributions of alumina substrate and TDP, later, on a TDP-SAM on alumina. The higher binding energy component of O1s in TDP (533.4 eV) can be assigned to hydroxy groups (P-O-H) and ester bonds (P-O-C), and the other component (532.1 eV) can be assigned to (P=O).[12] The ratio of these two contributions is 3.3:1, in good agreement with the expected value. The C1s signal has two contributions, a major one (284.9 eV) is assigned to the alkyl chain and the small peak is assigned to C-O-P bond (286.5 eV). The ratio of these two contributions 12.3 is quite close to the expected value (13).
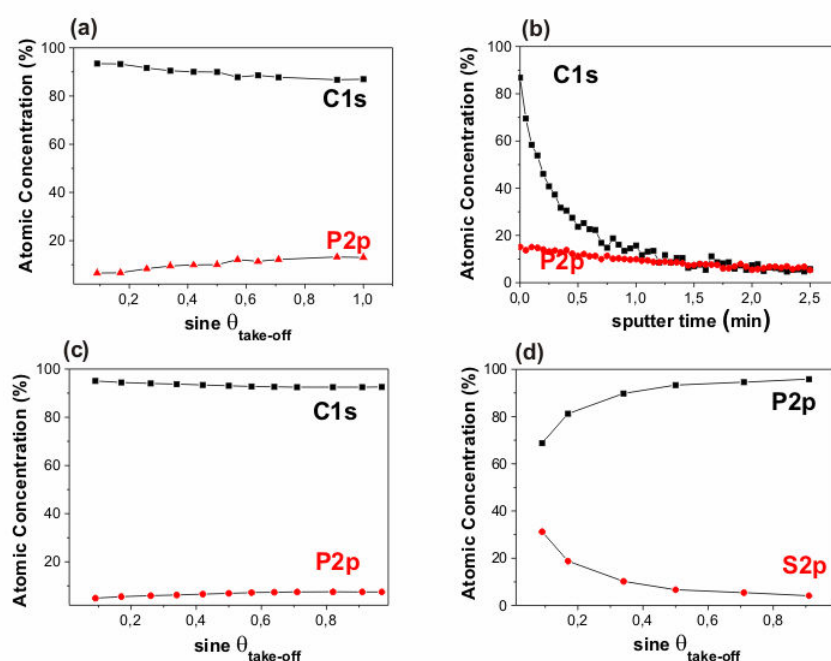
Figure 3.5 TDP SAM modified alumina (a) angle-dependent XPS, (b) XPS sputtering for depth profiling. Angle-dependent XPS of (c) PUD and (MUP) SAM modified alumina. Atomic concentration values are normalized to C+P.

The shape of the C1s curve on TDP SAM covered alumina looks similar to the C1s curve of bulk TDP, rather than C1s curve of carbon contamination on alumina. Moreover, the C/P ratio on SAM modified alumina is quite close to the expected value (15). The small O1s components of both alumina and TDP were very close to each other and could not be resolved. O1s curve was fitted with two contributions corresponding to the major peaks from alumina and bulk TDP. As shown in Table

3.2, shifts to higher binding energy values were observed at all substrate related peaks (Al2p, O1s-1) and to lower binding energies at all TDP originating peaks (P2p, O1s-4, C1s) which indicates deprotonation of PO_4 headgroup and a charge transfer from alumina substrate to the TDP during SAM formation.[12]

To observe the orientation of TDP, PUD and MUP in their SAMs on alumina, angle-dependent XPS was performed and the results are given in Figure 3.5 a,c,d. The electron take-off angles varied between 5-90 $^{\circ}$ (angle values are relative to the surface plane). The results show a clear dependence of the elemental peak intensities on the detection angle. As the detection angle increases, the amount of C1s from the alkyl chain decreases and the contribution of P from the headgroup increases. This indicates that P is located in the inner part of the SAM which is closer to the substrate surface when compared to C[12] and confirms the expected coordination of the phosphate group to the surface.[5, 12, 33] PUD and MUP have functional terminations and yet they still bind to alumina through phosph(on)ate headgroup.

To obtain additional information on the configuration of the TDP SAM, the monolayer was sputter-etched stepwise with Ar ions within the XPS chamber, and XPS analysis was done after each sputtering step. From Figure 3.5b the gradual decrease of the C content is observed upon sputtering, while P largely remains on the surface.

In summary, all the AFM, CA, FTIR and XPS measurements indicate the successful formation of the monolayers on alumina with a homogeneous coverage and semicrystalline order. Since phosph(on)ate SAMs with similar properties were prepared on various metal oxide substrates, TDP on Al_2O_3 can be used as a model system to study alkylphosph(on)ate SAMs on metal oxide surfaces.

3.2.3 Thickness of TDP SAM on alumina

Thickness will provide information on the orientation and tilt of the molecules. AFM has been typically employed to measure depth of pin-hole defects or islands of octadecylphosphonic acid (ODP) on oxide surfaces where they found values of 0.8-1.7 nm.[5, 9, 35] To measure the SAM thickness we used AFM, XPS and microcontact printing. A TDP layer on Al_2O_3 substrate was scratched by an AFM tip in contact mode (CM) by applying force and imaging orthogonally to the scratch (Figure 3.6). The thickness of the alkylphosphate layer on Al_2O_3 was calculated from the XPS data

according to the literature procedure.[36] The height of the TDP patterns were measured by AFM (Figure 3.7).
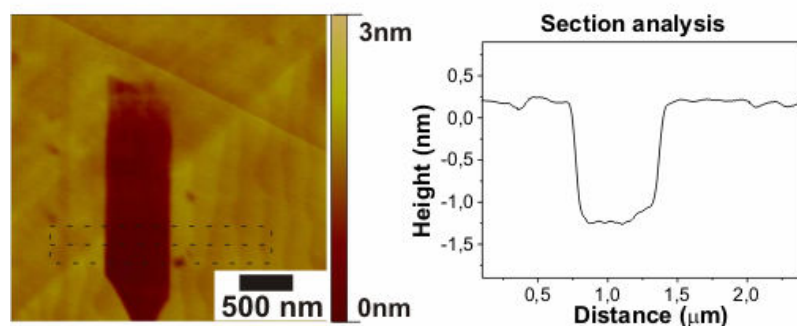
Figure 3.6 Contact Mode AFM height image of TDP layer on Al_2O_3 scratched by AFM tip. Depth:1.5 nm
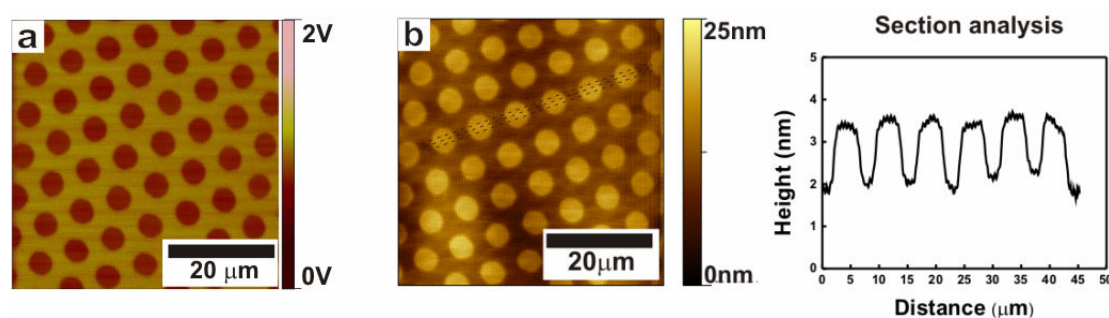
Figure 3.7 Contact mode AFM images of TDP pattern on alumina prepared by microcontact printing with 5 min contact time (a) friction (b) height.

The darker places in the friction image (Figure 3.7a) corresponds to lower friction force between surface and the AFM tip, allowing to distiguish between chemically different regions, while the bright parts in the height image correspond to elevated places which are TDP layers

The thickness for tetradecylphosphate (TDP, 14 Carbons) of 1,6 ± 0,1 nm found by XPS, is quite close to the values obtained from the scratching experiment (Figure 3.6) and microcontact printing (Figure 3.7). The XPS thickness of octadecylphosphonic acid (ODP, 18 Carbons) is 2,4 ± 0,2 nm. The XPS method gives an estimate of the thickness and is able to distinguish between two SAM layers having different chain lengths. The height of the TDP features (1.5 nm) is somewhat lower

than the extended adsorbate length (2.1 nm), which indicates a tilt in the SAM layer similar to various alkylphosph(on)ate SAMs on metal oxides.[5, 9, 12, 33]

3.2.4 Stability of TDP SAMs on alumina
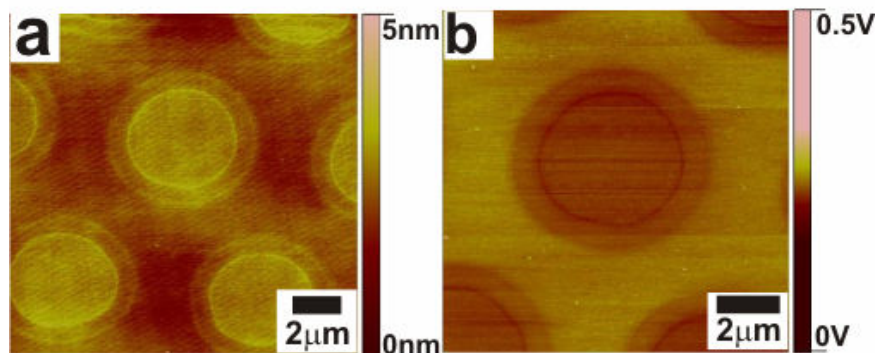
Figure 3.8 Contact mode AFM images of TDP patterns on alumina prepared by microcontact printing with 60 min contact time, (a) height, (b) friction.

There are several studies on diffusion of thiols on gold surfaces.[37-38] However, no work has been done to understand the diffusion mechanism of phosph(on)ates on metal oxide surfaces. To see the effect of contact time on resulting pattern and diffusion, TDP was printed for 60 min, much longer than the usual contact time which is 5 min. As seen in Figure 3.8, molecules diffuse to all directions. The step edges and terraces have different surface energies but it did not cause a preferential diffusion along the step edges detecteble within the lateral resolution of AFM. The diffusion is probably via the surface where inked PDMS patterns in contact with the surface act as reservoir of molecules and there is no indication of TDP deposition from vapor phase at non-contacting areas, which would have caused the loss of contrast in friction image (Figure 3.8b).

Patterns of TDP, ODP, ABP and MUP were prepared on R or C faces of alumina as well as on titania (AFM, not shown) by microcontact printing. The morphology was similar after 3 weeks. No loss in the resolution or no diffusion of molecules were observed within the resolution of AFM (not shown) which shows that the spreading of the molecules only occur during the stamping stage.

AFM, FTIR and CA confirmed the stability of TDP SAMs on alumina after 20 days of ambient exposure. Water immersion caused partial desorption of TDP SAM on alumina after 3180 min (Figure 3.9) due to its low stability in water especially at

basic conditions.[8] However, the TDP SAMs are stable in apolar organic solvents such as hexane and toluene as confirmed by stable CA values. In terms of water stability no qualitative difference was found between printed TDP and TDP SAM (Figure 3.9). The desorption is not homogeneous and seems to start at certain parts which may be due to lack of order in the SAM, while some regions remain intact which may correspond to well-ordered regions. Ordered and disordered regions cannot be distinguished so well by AFM as with the other surface characterization techniques (CA, FTIR and XPS) which are based on overall properties. To better understand the adsorption-desorption chracteristics of the SAMs, real time AFM can be done by using a liquid cell.
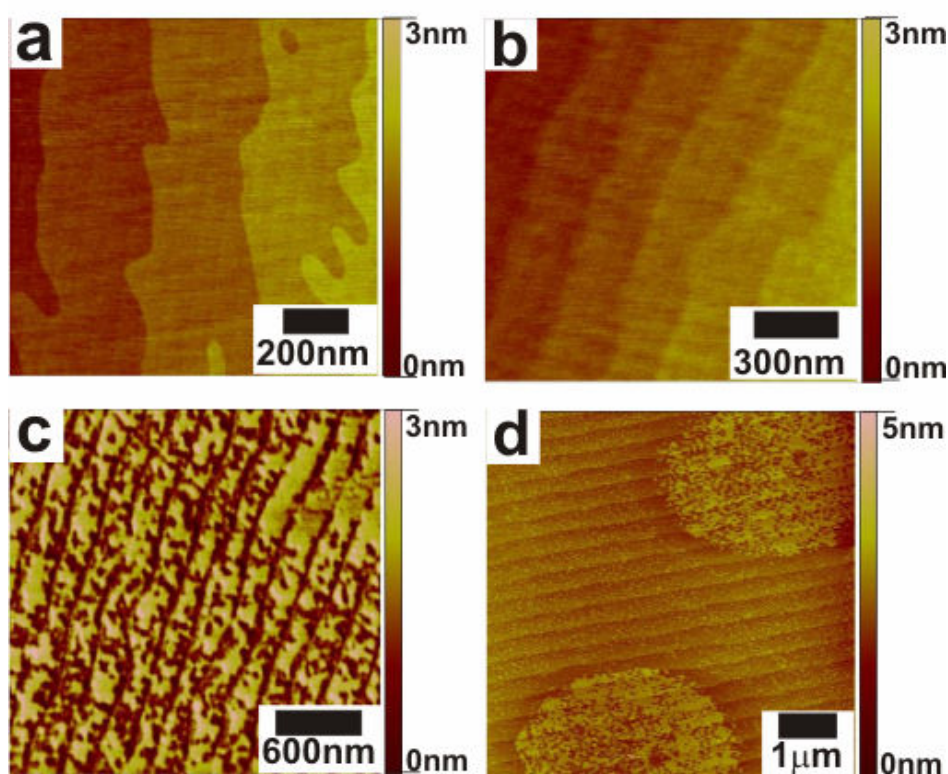
Figure 3.9 Contact mode AFM images of (a) TDP on Al_2O_3. After immersion in H_2O for (b) 10 min. (c) 180 min. (d) Printed TDP on Al_2O_3 after H_2O immersion for 60 min.

3.3 Conclusions

Several complementary techniques are applied to obtain information on structure and on different aspects of SAMs on metal oxides as well as of the assembly process. Phosph(on)ate SAMs cover the Al_2O_3 surface homogeneously having tails-up

orientation, with high coverage, and with a certain degree of order (AFM, CA, XPS, FTIR). There is no indication of in-plane registry between the surface atoms of substrates and phosph(on)ate headgroup. Phosphate and phosphonate based molecules showed similar properties. The molecules are tilted (AFM, XPS). There is indication of a charge transfer from the substrate to phosphate headgroup (XPS). The TDP molecules desorb upon immersion in water, however they are stable in organic solvents. Patterning has been applied to create chemically different regions. Functional terminated SAM provides the possibility to add new materials to the surface. The outcome of this chapter indicates that modification and patterning of metal oxide surfaces with phosph(on)ate-based SAMs provides suitable tools for fabrication.

3.4 Experimental
Materials

Polished substrates of R-($1\bar{1}02$) Al_2O_3 (1x10x10 mm), (100) TiO_2 (1x10x10 mm), (100) $SrTiO_3$ were purchased from SurfaceNet GmbH, Germany. These substrates were cut into 5x5 mm^2 pieces with a diamond saw and cleaned by ultrasonication in acetone and ethanol for 30 min each. Tetradecylphosphoric acid (TDP) was supplied by A. Wagenaar and J. Engbersen (RUG, Groningen). Aminobutylphosphonic acid (ABP, purity 99%) and 11-phosphonoundecanoic acid (PUD, purity 96%) were purchased from Sigma-Aldrich. ODP was purchased from ALFA AESAR. Mercaptoundecyl phosphonic acid (MUP) was synthesized according to a literature method.[39]

Sample preparation

Oxygen plasma-cleaned or annealed Al_2O_3, TiO_2, etched and annealed $SrTiO_3$, PLD grown $La_{0.67}Sr_{0.33}MnO_3$-$SrTiO_3$ and $LaAlO_3$-$SrTiO_3$ substrates were immersed into 1 mM ABP solution in 100:1 v/v hexane:isopropanol, a 1 mM PUD solution in 50:50 v/v ethanol:H_2O, 0.125 mM ODP solution in 100:1 v/v hexane:isopropanol or a 0.125 mM TDP solution in 100:1 v/v hexane:isopropanol for 2 days at room temperature. Afterwards, the samples were rinsed with the corresponding pure solvents or solvent mixtures, and dried under a flow of N_2.

Microcontact Printing

Silicon masters with micrometer-sized features were fabricated by photolithography. PDMS stamps were prepared from commercially available Sylgard-184 poly(dimethylsiloxane) (Dow Corning). The curing agent and the prepolymer were manually mixed in a 1:10 volume ratio and cured overnight at $60^{o}C$ against the master. The cured stamp was peeled off from the master at the curing temperature. Before printing, the stamps were rinsed with pure ethanol and dried under a flow of N_2. The stamps were inked with a few drops of solutions of TDP, ODP, MUP in ethanol or ABP in water. In the case of ABP, an oxidized stamp was used. The stamps were dried with N_2 and brought into conformal contact with alumina substrates for 5-60 min. After removing the stamps, the samples were rinsed with ethanol to wash off excess ink followed by drying under nitrogen.

Measurements

Atomic Force Microscopy (AFM): The morphology of the substrates was observed by a digital multimode Nanoscope III (Digital Instruments, Santa Barbara, CA) scanning force microscope, equipped with a J-scanner. All measurements were done at ambient in tapping mode or contact mode.

X-Ray Photoelectron Spectroscopy (XPS): Elemental composition was analysed by a Physical Electronics Quantera Scanning X-ray Multiprobe instrument, equipped with a monochromatic Al Kα X-ray source operated at 1486.7 eV and 25 W. Spectra were referenced to the main C1s peak at 284.80 eV.

Fourier Transform Infrared Spectroscopy (FTIR): Reflection-FTIR spectra of 1024 scans at 4 cm^{-1} were obtained using a BioRad FTS-60A spectrometer with a liquid nitrogen-coolded cryogenic mercury cadmium telluride detector and RAS accessory (BIO-RAD).

Contact Angle (CA): Measurements were done with a Kruss G10 goniometer, equipped with a CCD camera. Contact angles were determined automatically during growth of the droplet by a drop shape analysis. Milli-Q water (18.4 MOhm.cm) was used as a probe liquid.

3.5 References

1.   Schreiber, F., *Prog. Surf. Sci.* **2000,** *65*, 151.
2.   Love, J. C.; Estroff, L. A.; Kriebel, J. K.; Nuzzo, R. G.; Whitesides, G. M., *Chem. Rev.* **2005,** *105*, 1103.
3.   Onclin, S.; Ravoo, B. J.; Reinhoudt, D. N., *Angew Chem. Int. Ed.* **2005,** *44*, 6282.
4.   Tosatti, S.; Michel, R.; Textor, M.; Spencer, N. D., *Langmuir* **2002,** *18*, 3537.
5.   Gawalt, E. S.; Avaltroni, M. J.; Koch, N.; Schwartz, J., *Langmuir* **2001,** *17*, 5736.

6.   Gnauck, M.; Jaehne, E.; Blaettler, T.; Tosatti, S.; Textor, M.; Adler, H. J. P., *Langmuir* **2007,** *23*, 377.

7.   Hahner, G.; Hofer, R.; Klingenfuss, I., *Langmuir* **2001,** *17*, 7047.

8.   Liakos, I. L.; Newman, R. C.; McAlpine, E.; Alexander, M. R., *Langmuir* **2007,** *23*, 995.

9.   Messerschmidt, C.; Schwartz, D. K., *Langmuir* **2001,** *17*, 462.

10.   Pawsey, S.; Yach, K.; Reven, L., *Langmuir* **2002,** *18*, 5205.

11.   Sun, S. Q.; Leggett, G. J., *Nano Lett* **2007,** *7*, 3753.

12.   Textor, M.; Ruiz, L.; Hofer, R.; Rossi, A.; Feldman, K.; Hahner, G.; Spencer, N. D., *Langmuir* **2000,** *16*, 3257.

13.   Ahn, C. H.; Triscone, J. M.; Mannhart, J., *Nature* **2003,** *424*, 1015.

14.   Dagotto, E., *Science* **2005,** *309*, 257.

15.   Hwang, H. Y., *MRS Bull.* **2006,** *31*, 28.

16.   Schlom, D. G.; Chen, L. Q.; Pan, X. Q.; Schmehl, A.; Zurbuchen, M. A., *J. Am. Ceram. Soc.* **2008,** *91*, 2429.

17.   Kita, T.; Chiba, D.; Ohno, Y.; Ohno, H., *Appl. Phys. Lett.* **2007,** *90*, 3.

18.   Oleynik, II; Tsymbal, E. Y., *Interf. Sci* **2004,** *12*, 105.

19.   Schmalhorst, J.; Reiss, G., *J. Magn. Magn. Mater.* **2004,** *272*, E1485.

20.   Wang, D. X.; Nordman, C.; Daughton, J. M.; Qian, Z. H.; Fink, J., *IEEE Trans. Magn.* **2004,** *40*, 2269.

21.   Yuasa, S.; Nagahama, T.; Suzuki, Y., *Science* **2002,** *297*, 234.

22.   Yoshimoto, M.; Maeda, T.; Ohnishi, T.; Koinuma, H.; Ishiyama, O.; Shinohara, M.; Kubo, M.; Miura, R.; Miyamoto, A., *Appl. Phys. Lett.* **1995,** *67*, 2615.

23.   Brovelli, D.; Hahner, G.; Ruiz, L.; Hofer, R.; Kraus, G.; Waldner, A.; Schlosser, J.; Oroszlan, P.; Ehrat, M.; Spencer, N. D., *Langmuir* **1999,** *15*, 4324.

24.   Gao, W.; Dickinson, L.; Grozinger, C.; Morin, F. G.; Reven, L., *Langmuir* **1996,** *12*, 6429.

25.   Pawsey, S.; McCormick, M.; De Paul, S.; Graf, R.; Lee, Y. S.; Reven, L.; Spiess, H. W., *Journal of the American Chemical Society* **2003,** *125*, 4174.

26.   Lim, H. J.; Lee, D. Y.; Oh, Y. J., *Sensors and Actuators a-Physical* **2006,** *125*, 405.

27.   Breen, T. L.; Fryer, P. M.; Nunes, R. W.; Rothwell, M. E., *Langmuir* **2002,** *18*, 194.

28.   Burdinski, D.; Saalmink, M.; Van den Berg, J.; Van der Marel, C., *Angew Chem. Int. Ed.* **2006,** *45*, 4355.

29.   Falconnet, D.; Pasqui, D.; Park, S.; Eckert, R.; Schift, H.; Gobrecht, J.; Barbucci, R.; Textor, M., *Nano. Lett.* **2004,** *4*, 1909.

30.   Goetting, L. B.; Deng, T.; Whitesides, G. M., *Langmuir* **1999,** *15*, 1182.

31.   StJohn, P. M.; Craighead, H. G., *Appl. Phys. Lett.* **1996,** *68*, 1022.

32.   Fadeev, A. Y.; McCarthy, T. J., *Langmuir* **1999,** *15*, 3759.

33.   Spori, D. M.; Venkataraman, N. V.; Tosatti, S. G. P.; Durmaz, F.; Spencer, N. D.; Zurcher, S., *Langmuir* **2007,** *23*, 8053.

34.   Mitchon, L. N.; White, J. M., *Langmuir* **2006,** *22*, 6549.

35.   Hanson, E. L.; Schwartz, J.; Nickel, B.; Koch, N.; Danisman, M. F., *J. Am. Chem. Soc.* **2003,** *125*, 16074.

36.   ter Maat, J.; Regeling, R.; Yang, M.; Mullings, M. N.; Stacey, F. B.; Zuilhof, H., *Langmuir* **2009**.

37.   Gannon, G.; Larsson, J. A.; Greer, J. C.; Thompson, D., *Langmuir* **2009,** *25*, 242.

38.   Salazar, R. B.; Shovsky, A.; Schonherr, H.; Vancso, G. J., *Small* **2006,** *2*, 1274.

39.   Lee, T. R.; Carey, R. I.; Biebuyck, H. A.; Whitesides, G. M., *Langmuir* **1994,** *10*, 741.

Chapter 4

Electrochemical Stability of Self-Assembled Alkylphosphate Monolayers on Conducting Metal Oxides

Abstract

Alkylphosphate self-assembled monolayers (SAMs) were prepared on Nb-doped SrTiO$_3$ (Nb-STO) conducting metal oxide substrates. Unlike thiols on gold, the alkylphosphate SAMs on Nb-STO showed electrochemical stability over a wide voltage range of -2 to 2V. Cyclic voltammetry showed that SAM modification inhibited electrochemical activity of the conducting substrate with an efficiency dependent of the chain length. Impedance spectroscopy showed that SAM-modified Nb-STO substrates have higher resistance than bare substrates.

4.1 Introduction

There has been a vast interest into self-assembled monolayers (SAMs) owing to their ease of preparation, precise control of structure at a molecular level and wide variety of functionalities allowing a versatile manipulation of surface and interface properties.[1-4] Electrochemical techniques such as electrochemical impedance spectroscopy (EIS) and cyclic voltammetry (CV) are widely used to observe the properties of SAM-modified electrode surfaces[5-7] usually by comparing it with the bare electrode.[4, 7-10] SAMs reduce the electrochemical activity of the surface by forming effective insulating barriers to electron transfer and ion penetration.[4, 6-14]

SAMs of thiols on gold and silanes **on** SiO_2, have been studied extensively,[15-16] but SAMs on metal oxides are relatively new.[17] Alkylphosphates and alkylphosphonates form SAMs with very high ambient stability on metal oxides such as Ta_2O_5, Al_2O_3, ZrO_2 and TiO_2 without the need for controlled environmental conditions.[17-25]

Most of the electrochemical studies on SAMs involve thiols on gold.[3, 6, 26] However, upon repetitive CV cycles or by extending the operational potential windows during CV, thiol molecules desorb from the surface, leading to destruction of the monolayer.[3, 11, 27-29] Octadecyltrichlorosilane monolayers on gold have been reported to be electrochemically unstable as well.[1] There are few studies about alkylphosphonates in electrochemistry, such as on nitinol[7] or on ITO[4] in which case they were studied within a rather narrow potential range of -0.5 to 1 V.

Here, the electrochemical behavior and stability of alkylphosphate SAMs with different chain lengths assembled on conducting metal oxide Nb-doped $SrTiO_3$ (Nb-STO) is investigated by using CV and EIS.

4.2 Results and discussion

4.2.1. SAM formation

Previously, we have shown the detailed characterization of a tetradeclylphosphate (TDP) SAM on alumina which resulted in the successful formation of a homogeneous SAM with a high coverage (See Chapter 3).[17] The height of the TDP layer was around 1.5 nm. This is somewhat lower than the extended adsorbate length (2 nm), which indicates a tilt in the SAM layer similar to various alkyl phosph(on)ate SAMs on metal oxides[17-18, 22, 25]

The preparation of monolayer-modified Nb-STO substrates was performed according to literature procedures.[17-18, 22, 24-25] Clean Nb-STO substrates were immersed into alkylphosphate (with 10 (DP), 14 (TDP), 18 (ODP) C atoms) solutions for two days at room temperature, rinsed afterwards with solvent and dried under a flow of N_2 to yield an alkyl-functionalized substrate. The water contact angle (CA) of oxygen plasma-cleaned Nb-STO was below 10°, which increased to 115° after alkylphosphate SAM modification for all chain lengths. The high CA value indicates a quite hydrophobic surface and this confirms a methyl-terminated SAM. XPS measurements showed that all the expected elements were present on the surface in the expected ratios.

4.2.2 Electrochemistry

Cyclic voltammetry (CV) was performed on bare and alkylphosphate (DP, TDP, ODP) modified Nb-STO substrates. The samples were placed in a 0.1 M tetrabutylammonium hexafluorophosphate ($Bu_4N^+PF_6^-$) solution in acetonitrile and data were collected with 100-200 mV/s scan rates within potential ranges of either -0.1 to 1 V or -2 V to 2 V. All recorded data are averages of five scans.

Figure 4.1 shows the effect of changing the scan rate from 100 to 200 mV/s on the bare and TDP-modified Nb-STO substrates within the -0.1 to 1 V range. Since not much difference was seen between these scan rates, 200 mV/s was used was used in further experiments. More importantly, the comparison between the bare and TDP-covered substrates shows a clear blocking effect of the SAM.
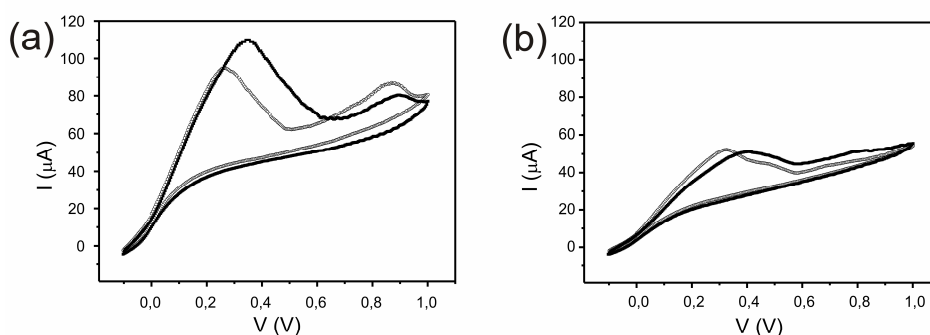

Figure 4.1 Cyclic voltammograms on (a) bare and (b) TDP SAM-modified Nb-STO, performed at 100 (o) and 200 mV/s (■) scan rates.
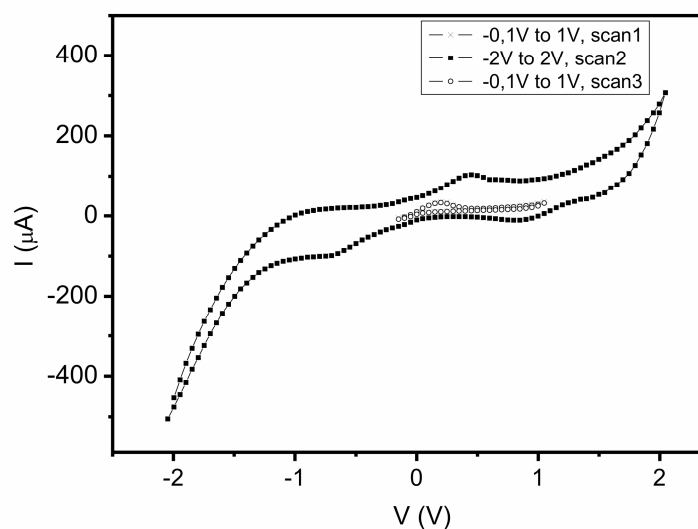
Figure 4.2 Cyclic voltammograms of TDP SAM-modified Nb-STO performed from -0.1 to 1 V (scan 1) and back, then -2 V to 2 V (scan 2) and back followed by another cycle from -0.1 to 1 V (scan 3), all at a 200 mV/s scan rate.

To check the electrochemical stability of a TDP SAM on Nb-STO, the sample was subjected to CV between -0.1 to 1 V, then the potential window was widened to -2 to 2 V, and another measurement was done. Finally, the sample was measured again at the initial potential window (-0.1 to 1V). As seen in Figure 4.2, the first and the third measurements are identical, which means that the TDP SAM on Nb-STO is stable over a voltage range of as wide as -2 V to 2 V. There appears to be no noticable change, damage or desorption of the SAM. This marks a clear contrast with thiols on gold which have a rather limited potential window at which they are stable.[30] The high stability of phosphate SAMs on Nb-STO may be due the different nature of the bond between the phosphate headgroup and metal oxide surface, and potentially to the absence of oxidative and reductive desorption pathways.
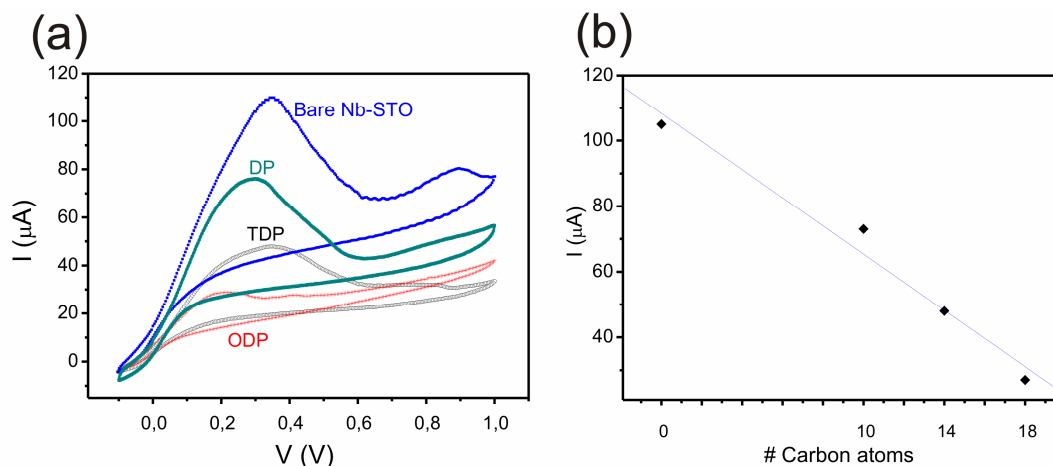
Figure 4.3 (a) Cyclic voltammograms of bare and of alkylphosphate SAM modified Nb-STO substrates. (b) Current at 0.3 V vs alkyl chain length. The linear fit is a guide to the eye, not a result of a model.

Figure 4.3 shows a comparison of the CVs of a bare substrate and substrates modified with alkylphosphate SAMs of different chain lengths. The CVs of bare and modified Nb-STO have similar shapes, showing a single oxidative peak around 0.3 V, but with reduced height for the SAM-modified samples. Since the samples were scanned five times each, with no apparent change to the shape and height of the CV graph, SAMs are stable and resistant to oxidative desorption.[7] The SAMs block the electrochemical activity of the substrate and effectively insulate it from the environment. The longer chain alkylphosphates seem to be more efficient compared to shorter ones. If the coverage is assumed similar and pin hole defects are negligible for all SAMs, the currents would reflect quantum-mechanical tunneling with a monotonic dependence on chain length,[4] which seems to be the case here (Figure 4.3b).

Electrochemical impedance spectroscopy (EIS) was performed in the range of 10 kHz to 10 mHz at a potential of -0.2V. Bare Nb-STO, DP- and TDP modified Nb-STO were compared. EIS provides a measure of the resistance and quality of the coating on a conducting substrate.[7] Figure 4.4 shows the impedance (Nyquist) plots of bare, DP and TDP-modified Nb-STO substrates. As seen in the figure, the impedance semicircle of TDP is larger than that of DP, which indicates that TDP has a higher resistance (~100 kΩ vs ~50 kΩ) and forms a better barrier in insulating the conducting metal oxide. This is expected since TDP has a longer chain. Although we

51

have no quantitative values, the resistances follow $R_{NbSTObare} < R_{DP} < R_{TDP}$, according to EIS. The capacitance values can be estimated as 5.5×10^{-7} and 3.7×10^{-7} F for DP and TDP, respectively.
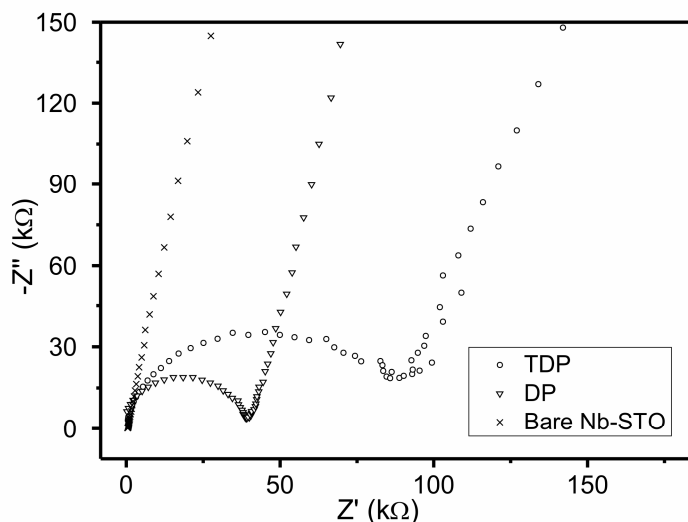

Figure 4.4 Impedance spectroscopy (Nyquist plots) of bare and DP and TDP modified Nb-STO substrates.

4.3 Conclusions

Electrochemistry (CV and EIS) has shown that alkylphosphate SAMs inhibit the electrochemical activity of the Nb-STO conducting metal oxide substrate. The inhibition efficiency increased with increasing chain length of the SAM. Unlike thiols on gold, the alkylphosphate SAMs on Nb-STO show electrochemical stability over a voltage range as wide as -2 to 2 V. The resistance of a SAM layer is much higher than of the bare substrate and increases with chain length. The described system opens new possibilities to study electrochemical properties of semiconductors functionalized with various phosphate-based adsorbates.

4.4 Experimental
Materials

Polished substrates of (100) 0.5wt% niobium-doped $SrTiO_3$ (Nb-STO) (1x10x10 mm) were purchased from SurfaceNet GmbH, Germany. These substrates were cut into 5x5 mm^2 pieces with a diamond saw and cleaned by ultrasonication in acetone and

ethanol for 30 min each. Decylphosphoric acid (DP), tetradecylphosphoric acid (TDP) and octadecylphosphoric acid (ODP) were supplied by A. Wagenaar and J. Engbersen (RUG, Groningen).

SAM formation

Oxygen plasma-cleaned Nb-STO substrates were immersed into 0.125 mM alkyl phosphoric acid solutions in 100:1 v/v hexane:isopropanol for two days at room temperature. Afterwards, the samples were rinsed with the pure solvent mixture, and dried under a flow of N_2.

Measurements

Electrochemistry: Cyclic voltammetry (CV) measurements were performed with an AUTOLAB PGSTAT10, at 100-200 mV/s scan rates in a voltage range of -2 V to 2 V. Measurements were performed on bare or SAM-modified Nb-STO in 0.1 M tetrabutylammonium hexafluorophosphate ($Bu_4N^+PF_6^-$) in acetonitrile using Ag/AgCl, and Pt as the reference and counter electrodes, respectively. All scans shown are averages over five measurements. Electrochemical impedance measurements were performed in the same setup within the range of 10 kHz to 10 mHz at -0.2 V.

X-Ray Photoelectron Spectroscopy (XPS): Elemental composition was analyzed by a Physical Electronics Quantera Scanning X-ray Multiprobe instrument, equipped with a monochromatic Al Kα X-ray source operated at 1486.7 eV and 25 W. Spectra were referenced to the main C1s peak at 284.80 eV.

Contact Angle (CA): Measurements were done with a Kruss G10 goniometer equipped with a CCD camera. Contact angles were determined automatically during growth of the droplet by a drop shape analysis. Milli-Q water (18.4 MOhm.cm) was used as a probe liquid.

4.5 References

1. Finklea, H. O.; Robinson, L. R.; Blackburn, A.; Richter, B.; Allara, D.; Bright, T., *Langmuir* **1986,** *2*, 239.
2. Sabatani, E.; Rubinstein, I., *J. Phys. Chem.* **1987,** *91*, 6663.
3. Shervedani, R. K.; Hatefi-Mehrjardi, A.; Babadi, M. K., *Electrochim. Acta* **2007,** *52*, 7051.
4. Jedaa, A.; Burkhardt, M.; Zschieschang, U.; Klauk, H.; Habich, D.; Schmid, G.; Halik, M., *Org. Electron.* **2009,** *10*, 1442.
5. Campuzano, S.; Pedrero, M.; Montemayor, C.; Fatas, E.; Pingarron, J. M., *J. Electroanal. Chem.* **2006,** *586*, 112.
6. Ganesh, V.; Pal, S. K.; Kumar, S.; Lakshminarayanan, V., *J. Coll. Interf. Sci.* **2006,** *296*, 195.

7. Quinones, R.; Gawalt, E. S., *Langmuir* **2008,** *24*, 10858.
8. Diao, P.; Jiang, D. L.; Cui, X. L.; Gu, D. P.; Tong, R. T.; Zhong, B., *J. Electroanal. Chem.* **1999,** *464*, 61.
9. Finklea, H. O.; Snider, D. A.; Fedyk, J., *Langmuir* **1990,** *6*, 371.
10. Porter, M. D.; Bright, T. B.; Allara, D. L.; Chidsey, C. E. D., *J. Am. Chem. Soc.* **1987,** *109*, 3559.
11. Finklea, H. O.; Avery, S.; Lynch, M.; Furtsch, T., *Langmuir* **1987,** *3*, 409.
12. Janek, R. P.; Fawcett, W. R.; Ulman, A., *Langmuir* **1998,** *14*, 3011.
13. Ma, H. Y.; Yang, C.; Chen, S. H.; Jiao, Y. L.; Huang, S. X.; Li, D. G.; Luo, J. L., *Electrochim. Acta* **2003,** *48*, 4277.
14. Rubinstein, I.; Steinberg, S.; Tor, Y.; Shanzer, A.; Sagiv, J., *Nature* **1988,** *332*, 426.
15. Onclin, S.; Ravoo, B. J.; Reinhoudt, D. N., *Angew. Chem. Int. Ed.* **2005,** *44*, 6282.
16. Schreiber, F., *Progr. Surf. Sci.* **2000,** *65*, 151.
17. Yildirim, O.; Gang, T.; Kinge, S.; Reinhoudt, D. N.; Blank, D. H. A.; van der Wiel, W. G.; Rijnders, G.; Huskens, J., *Int. J. Mol. Sci.* **2010,** *11*, 1162.
18. Gawalt, E. S.; Avaltroni, M. J.; Koch, N.; Schwartz, J., *Langmuir* **2001,** *17*, 5736.
19. Gnauck, M.; Jaehne, E.; Blaettler, T.; Tosatti, S.; Textor, M.; Adler, H. J. P., *Langmuir* **2007,** *23*, 377.
20. Hahner, G.; Hofer, R.; Klingenfuss, I., *Langmuir* **2001,** *17*, 7047.
21. Liakos, I. L.; Newman, R. C.; McAlpine, E.; Alexander, M. R., *Langmuir* **2007,** *23*, 995.
22. Messerschmidt, C.; Schwartz, D. K., *Langmuir* **2001,** *17*, 462.
23. Pawsey, S.; Yach, K.; Reven, L., *Langmuir* **2002,** *18*, 5205.
24. Sun, S. Q.; Leggett, G. J., *Nano Lett.* **2007,** *7*, 3753.
25. Textor, M.; Ruiz, L.; Hofer, R.; Rossi, A.; Feldman, K.; Hahner, G.; Spencer, N. D., *Langmuir* **2000,** *16*, 3257.
26. Mekhalif, Z.; Riga, J.; Pireaux, J. J.; Delhalle, J., *Langmuir* **1997,** *13*, 2285.
27. Hobara, D.; Ota, M.; Imabayashi, S.; Niki, K.; Kakiuchi, T., *J. Electroanal. Chem.* **1998,** *444*, 113.
28. Schneider, T. W.; Buttry, D. A., *J. Am. Chem. Soc.* **1993,** *115*, 12391.
29. Walczak, M. M.; Popenoe, D. D.; Deinhammer, R. S.; Lamp, B. D.; Chung, C. K.; Porter, M. D., *Langmuir* **1991,** *7*, 2687.
30. Beulen, M. W. J.; Kastenberg, M. I.; van Veggel, F.; Reinhoudt, D. N., *Langmuir* **1998,** *14*, 7463.

<div align="right">

Chapter 5

</div>

Electrical Properties of Self-Assembled Monolayers on Conducting Metal Oxides

Abstract

Pt top contacts were deposited by pulsed laser deposition (PLD) on bare Nb doped $SrTiO_3$ (Nb-STO) and on the same type of substrate modified with a tetradecylphosphate self-assembled monolayer (SAM). Afterwards samples were checked by electrochemical Cu deposition which occured only at the places where electrical shorts existed between the top contact and the substrate. Nearly 100% yield of top contacts without shorts were prepared, which shows the dense packing and robustness of the SAM. The SAM decreases the leakage current about 500 times compared to the bare substrate. Alkylphosphate SAMs on conducting metal oxide substrates can therefore be used as dielectric thin films for device fabrication.

5.1 Introduction

Recently the use of self-assembled monolayers (SAMs) at nanometer scale electronic devices has become a very important topic in the field of molecular electronics and nanotechnology.[1-3] There has been research on macroscale electronic properties of SAMs,[1-3] or use of SAMs in nanoscale transistors (OTFTs, OFETs).[2, 4-6] Since SAMs are easily prepared with low cost and have only a few nanometers thickness, SAMs have proven to be excellent candidates to be used as the gate dielectrics in organic thin-film transistors.[1, 4, 7] They change the semiconductors electronic properties and decrease leakage current drastically[7-8] compared to a thin SiO_2 layer.[9]

SAMs as dielectric layers were studied before. However, in most of these studies hybrid dielectric layers composed of SAM and Al_2O_3 or SiO_2 were used on Al or doped Si bottom electrodes.[1-4, 6-11] This makes the interpretation of the contribution of the SAM layer difficult.[11] Thus, we use a conducting metal oxide which do not contain any additional inorganic dielectric layer. $SrTiO_3$ is an insulator perovskite oxide but can become an n-type semiconductor or metallic conductor by suitable doping with niobium (Nb).[12] In order to use SAMs on such oxides in electronic or spintronic devices, the electrical properties of such SAMs need to be studied.

To study the electronic properties of SAMs, top contacts usually need to be prepared. However, conventional metal contact deposition methods often damage the thin organic layer and cause electrical short circuits.[5, 13-15] Several approaches were applied to avoid shorts such as using a Hg droplet as a top contact,[15] inserting a conducting polymer layer between SAM and top contacts,[13-14] or approaching the substrate with a conducting AFM tip.[16] Pulsed laser deposition (PLD) was used as a gentle metal top contact deposition method as well, on thiol SAMs on gold, which resulted in a 15% yield of isolated top and bottom electrodes for an octadecanethiol SAM.[5]

Here, we demonstrate a method for low kinetic energy deposition of Pt top contacts on alkylphosphate SAMs by pulsed laser deposition and electrical characterization of the alkylphosphate SAMs on conducting Nb-STO metal oxide susbtrate by I-V measurements and electrochemical Cu deposition.

5.2 Results and discussion

In order to test the electrical properties, a TDP organic thin film is used as a dielectric barrier layer. To have a thicker organic layer, a TDP-modified substrate was covered with a thin poly(ethyleneimine) (PEI) layer. For comparison, a bare Nb-STO substrate and a substrate covered with a PLD deposited thin Al_2O_3 inorganic dielectric layer were prepared. Pt top contacts were deposited on the samples by PLD. The samples were further checked for electrical shorts with electrochemical Cu deposition and the electrical behaviour of samples were studied with I-V measurements. The samples are shown in Figure 5. 1.
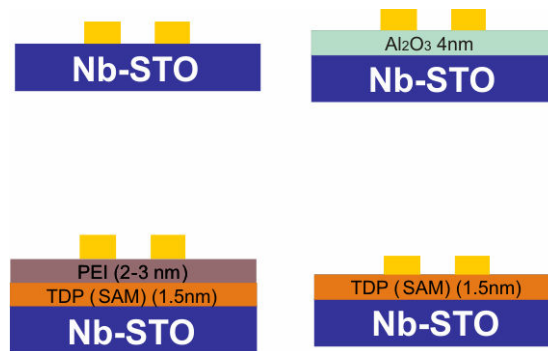

Figure 5.1 The schematics of bare, Al_2O_3 covered, PEI+TDP SAM-covered and TDP SAM-covered Nb-STO, with Pt top contacts.

5.2.1 Sample preparation

In our previous work, (see chapter 3) we have shown the detailed characterization of TDP SAMs on alumina which resulted in the successful formation of a homogeneous TDP SAM with a high coverage.[17] The height of the TDP features was around 1.5 nm. This is somewhat lower than the extended adsorbate length (2 nm), which indicates a tilt in the SAM layer similar to various alkylphosph(on)ate SAMs on metal oxides.[18-20]

The preparation of monolayer-modified Nb-STO substrates was performed according to literature procedures. [17-20] Clean Nb-STO substrates were immersed into TDP solutions for two days at room temperature, rinsed afterwards with solvent and dried under a flow of N_2 to yield a SAM-functionalized substrate. For subsequent PEI adsorption, TDP-functionalized Nb-STO substrates were immersed into a PEI solution for 5 min and then dipped in ethanol several times to wash off excess PEI. Similar treatment of an alumina substrate with PEI resulted in a homogeneous layer of

PEI with around 3.0 nm thickness.[17] Atomic force microscopy (AFM) and scanning tunnelling microscopy (STM) confirmed the smooth surface without any defects upon SAM formation (data not shown). The water contact angle (CA) of oxygen plasma-cleaned Nb-STO was below 10°, which increased to 115° and 45° for TDP-SAM and PEI-covered surface respectively. The high CA value for TDP indicates a quite hydrophobic surface and this confirms the CH_3 termination. In conclusion, the measurements indicate the successful formation of the TDP SAM on Nb-STO. By measuring the height of PLD deposited Al_2O_3 patterns by AFM, deposition rates were determined and the deposition time was adjusted in order to have a 4 nm alumina layer on Nb-STO.

5.2.2 Pt Top Contact Fabrication and Electrochemical Cu Deposition

In this study, Si_3N_4 membranes embedded in a silicon chip were used as stencils for the patterned deposition of metals on SAMs by pulsed laser deposition (PLD) as described before.[5, 21] Figure 5.2 a shows the PLD procedure, in which the Nb-STO substrate is placed parallel to a Pt target.[22] The laser hits the target and creates a plasma of the target material in the presence of Ar background gas with reduced pressure. At low background pressure, the mean free path (mfp) of the ablated species (Pt) is larger than the distance between target and the substrate, which results in high energy Pt atoms[5] and potentially leading to a damage of the SAM. When high Ar background pressure is used, the mfp of Pt is smaller than the target-substrate distance which results in thermalized and low energy Pt atoms. This is especially critical not to damage the organic thin film layer.[5]

By clamping a stencil on a bare or modified substrate, Pt is deposited only through the stencil apertures and Pt top contact pattern is created (Figure 5.2 b). At low pressure more directional deposition and thus a sharp pattern is expected and at high pressure a broadened pattern may be expected.[23]
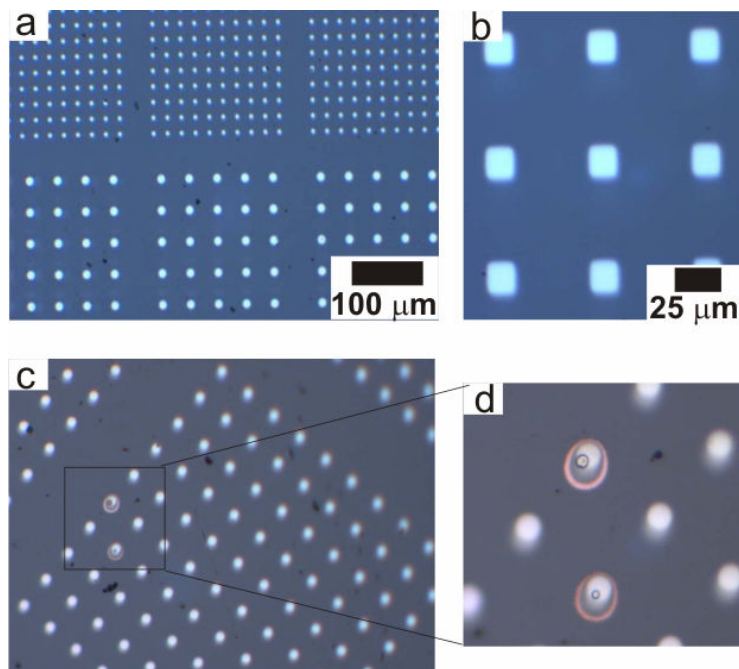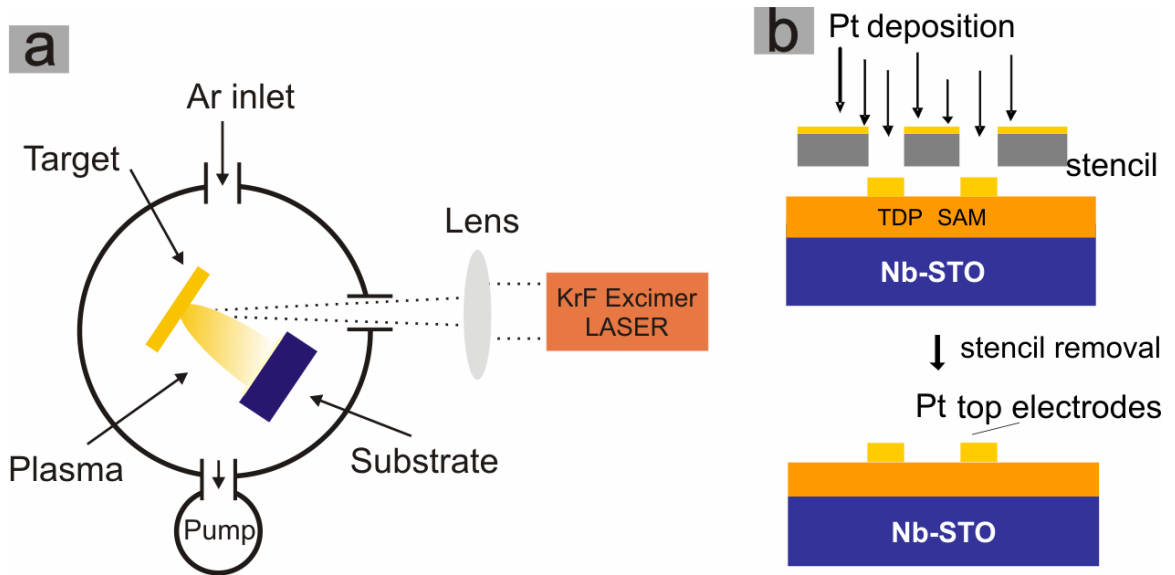
Figure 5.2 (a) Schematic picture of the PLD system used. (b) Schematic representation of stencil deposition of Pt top contacts on TDP ($C_{14}PO_4$) SAM modified Nb-STO substrate.

Figure 5.3 Optical images of (a,b) Pt top contacts on TDP SAM-modified Nb-STO after stencil deposition by PLD with high pressure. (c,d) Same sample after electrochemical Cu growth, with the zoom-in to the region where Cu growth was seen (d). The yield of Pt top contacts without Cu growth, thus without shorts is 99%.

Figures 5.3 and 5.4 show the Pt patterned TDP SAM-modified Nb-STO surface before and after electrochemical Cu deposition. Stencil deposition by PLD

created clean, uniform and well defined Pt patterns with 17nm height, on TDP-SAM covered Nb-STO (Figure 3a,b, 4a). After electrochemical Cu deposition, almost all of the patterns remained unchanged which shows Pt top contacts without any shorts with a yield of almost 100% were succcessfully prepared. Only at a few places out of hundreds, shorts between the top contact and the substrate could be seen, as indicated by Cu growth[5] (Figure 5.3c,d, 5.4b). The Cu non-uniform Cu deposits are 30-300 nm in height. The patterns without shorts are clean and have a similar height as before electrochemical deposition, which indicates that no deposition had occurred onto these (Figure 5.4b).
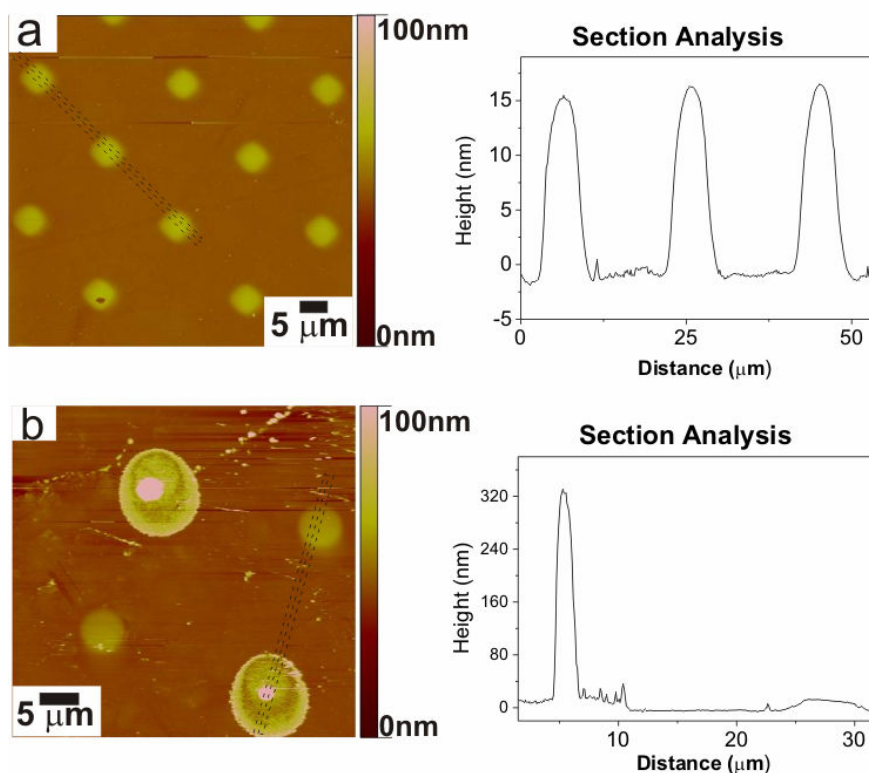

Figure 5.4 AFM height images, with section analysis of (a) Pt top contacts on TDP SAM-modified Nb-STO after stencil deposition by PLD with high pressure. (b) Same sample after electrochemical Cu growth focussed on the area where Cu growth was seen.
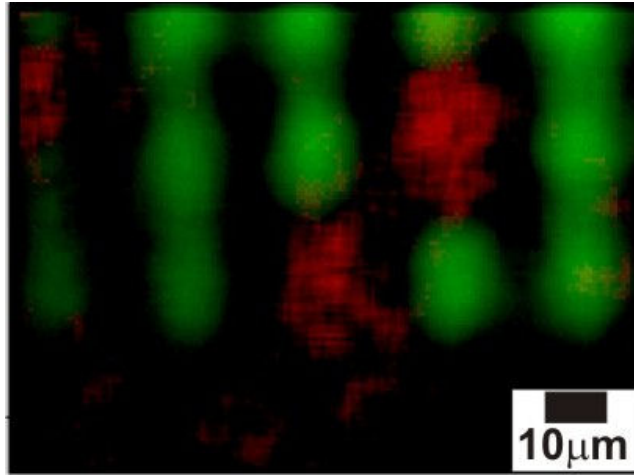
Figure 5.5 XPS mapping showing the Pt rich regions (green) and Cu rich regions (red). The resolution in the x direction is better because of the dispersive properties of the analyzer in the Quantera XPS

Figure 5.5 shows the XPS mapping of Pt and Cu after electrochemical Cu growth on the region shown in Figure 5.4b. The red parts representing Cu match well with the elevated parts seen in the AFM (Figure 5.4b). Similar to AFM images, the Pt patterns (green) are much more uniform than the Cu patterns, and do not contain Cu

Optical microscopy, AFM and XPS all confirmed the formation of isolated Pt top contacts on TDP-modified Nb-STO substrates with a high yield of almost 100%. Similar attempts of Au top contact growth on octadecanethiol-modified Au substrates yielded 15% isolated islands.[5] The background pressure and sample target distance were similar to ours. Possible explanation of high success in our system may be due to the smoothness of metal oxides over large distances unlike gold surface which has deep trenches. Although thiols form densely-packed and well-ordered monolayers, the overall structure may not be smooth over large areas. However, the difference could also be due to the substrate since in our procedure a metal oxide is used which has a much higher resistivity (~35 Ω.cm) than gold (~2x10^{-6} Ω.cm). To investigate if low conductivity of Nb-STO results in low Cu growth although there might be shorts, we performed more experiments.

As control experiments, Pt patterns were deposited on bare Nb-STO and on TDPSAM-modified Nb-STO by the same method (PLD, stencil deposition) under harsh deposition conditions (low pressure). Pt patterns after deposition are shown in Figure 5.6 a, d and 5.7 a, b).

Optical images and AFM confirm uniform Cu growth on all of the Pt top contacts at bare substrate after electrochemical Cu growth, with very high density (Figures 5.6b,c and 5.7c). On these substrates, the Pt patterns are in direct contact with the substrate. No Cu growth was observed on the bare substrate regions indicating the necessity of Pt to initiate Cu growth. This experiment clearly proves that if a Pt pattern is in contact with bottom electrode (Nb-STO), Cu growth occurs. In case of Pt patterns deposited on a TDPSAM-modified Nb-STO with harsh deposition conditions, Cu growth was seen on most of the Pt dots after electrochemical Cu growth, but with lower density when compared to bare substrates (Figures 5.6e,f and 5.7e). In this case, the SAM layer still acts as a barrier between the conducting substrate and the top contacts to some degree. In conclusion, high pressure deposition enables the fabrication of isolated metal top contacts without damaging the SAM layer.
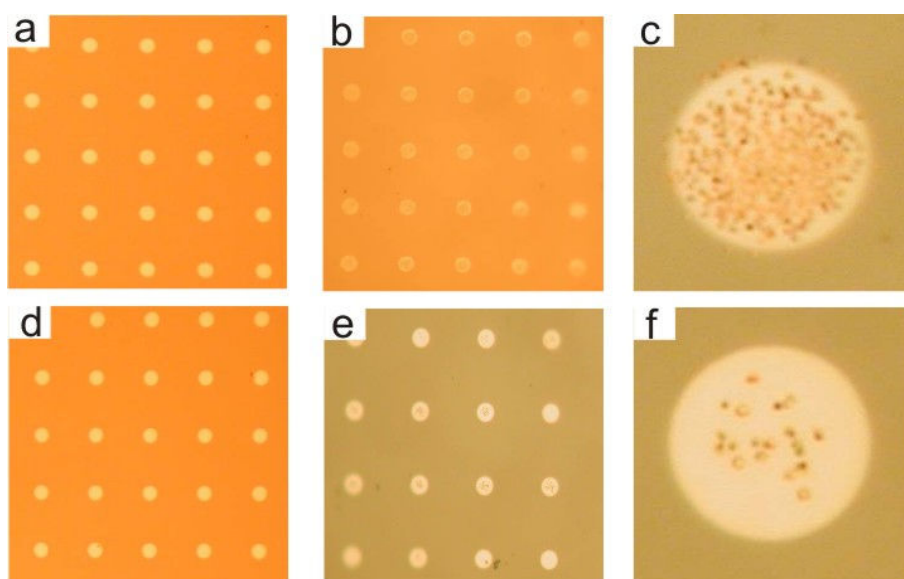

Figure 5.6 Optical images of Pt top contacts of (a) bare Nb-STO after stencil deposition by PLD with conditions for harsh landing. (b, c) Same sample after electrochemical Cu deposition, with the zoom-in to a region where Cu growth was seen (c). Optical images of Pt (d) top contacts of TDPSAM-modified Nb-STO after stencil deposition by PLD with conditions for harsh landing. (e,f) Same sample after electrochemical Cu deposition, with the zoom-in to a region where Cu growth was seen (f).
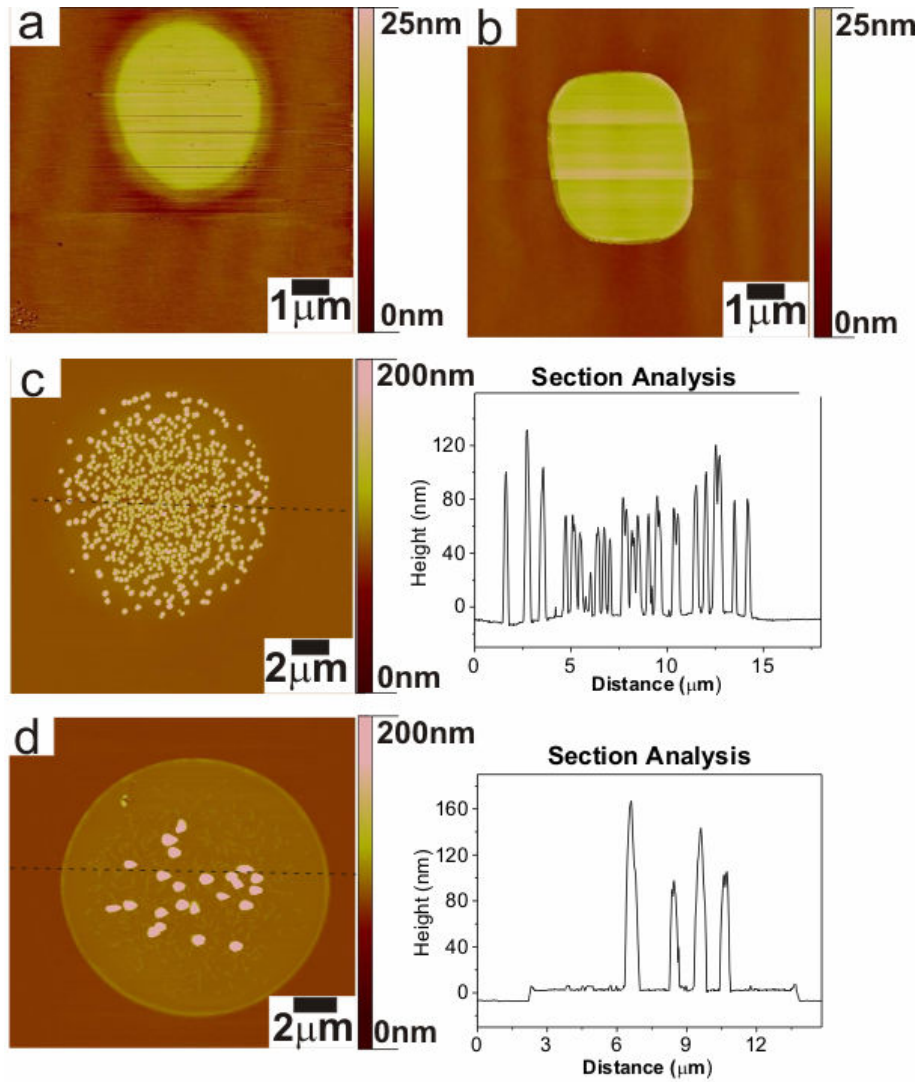
Figure 5.7 AFM height images: Pt top contacts after PLD on (a) bare Nb-STO, (b) Pt TDPSAM-modified Nb-STO. Pt top contacts after electrochemical Cu deposition, with section analysis on, (c) bare Nb-STO (d) TDP-SAM modified Nb-STO.

5.2.3 Electrical Properties of the TDP-SAM layer on Nb-STO

In order to asses the electrical properties of SAMs on conducting metal oxides, Pt patterns were deposited at high pressure on bare and SAM-modified conducting Nb-STO substrates as described above (Figure 5.1). Top-top J-V measurements were performed (Figure 5.8). A TDP SAM and a SAM with additional PEI were used as a dielectric barrier between the Nb-STO bottom electrode and the Pt top contact. For comparison, Pt was deposited on a bare Nb-STO substrate and a substrate modified with a thin (4nm) Al_2O_3 inorganic dielectric layer.
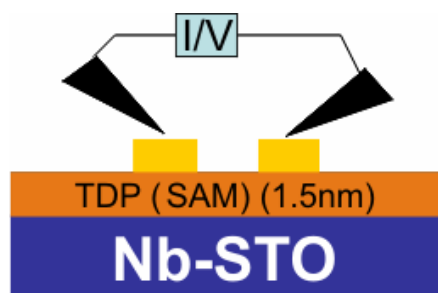
Figure 5.8. The Schematics of top contacts and top-top measurement configuration on TDPSAM-modified Nb-STO.

Figure 5.9 shows the J-V measurements of bare and modified Nb-STO substrates. The leakage current of the TDP organic thin film is three orders of magnitude less than that of the bare Nb-STO substrate. When a thicker organic layer is formed, here accomplished by adsorption of PEI onto a TDP SAM, there is a small additional decrease of the leakage current. SAMs on conducting single crystal metal oxide can be robust and densely packed although extremely thin (1.5nm) resulting in a dramatic decrease in the leakage current comparable with a 4 nm Al_2O_3 layer.
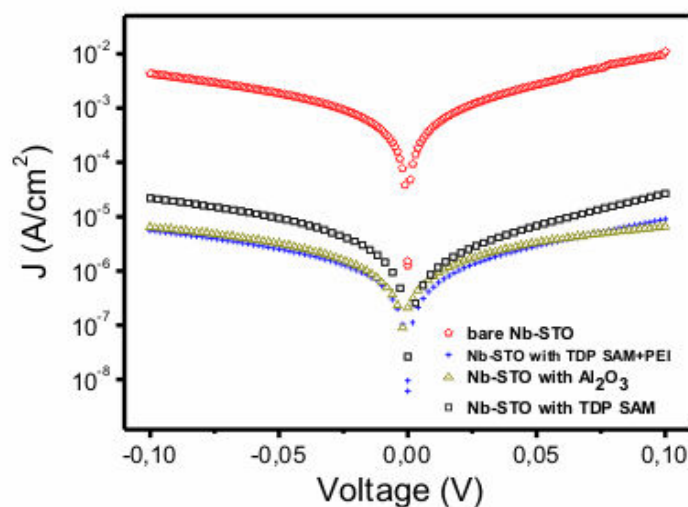

Figure 5.9 J-V curves of bare, TDPSAM-modified, Al_2O_3-covered and TDP SAM+PEI covered Nb-STO substrates.

The nature of contact between the substrate, SAM and Pt is not known. To determine the electron transport mechanism and the type of barrier, more experiments should be done, in a wider voltage range and at different temperatures.

5.3 Conclusions

Stencil deposition combined with PLD allows to create many features in a single deposition step. Increasing the background pressure enables metal top contact deposition without damaging the SAM layer and without causing shorts with almost 100% yield. SAMs on conducting single crystal metallic oxide are therefore concluded to be densely packed and robust. Smoothness of metal oxide substrate may also have contributed to avoiding shorts. Electrochemical metal deposition is a fast and easy way to check shorts of large number of top contacts. SAM modification results in a dramatic decrease in the leakage current comparable with a 4 nm Al_2O_3 layer. Increasing the organic layer thickness by additional thin polymer layer results in a further decrease of the leakage current. Thus alkylphosphate SAMs on conducting metal oxide substrates can be used as dielectric thin films.

5.4 Experimental
Materials

Polished substrates of (100) 0.5wt% niobium-doped $SrTiO_3$ (Nb-STO) (1x10x10 mm) were purchased from SurfaceNet GmbH, Germany. These substrates were cut into 5x5 mm^2 pieces with a diamond saw and cleaned by ultrasonication in acetone and ethanol for 30 min each. Tetradecylphosphoric acid (TDP) was supplied by A. Wagenaar and J. Engbersen (RUG, Groningen). Poly(ethyleneimine) (PEI) was purchased from Fluka. The stencils were purchased from C2V (Enschede, NL) fabricated according to a published procedure. [24]

SAM formation

Oxygen plasma-cleaned Nb-STO substrates were immersed into a 0.125 mM TDP solution in 100:1 v/v hexane:isopropanol for two days at room temperature. Afterwards, the samples were rinsed with the solvent mixture, and dried under a flow of N_2. In the case of additionally adsorbed PEI, TDP-modified substrates were immersed in a 20 mg/ml PEI solution in chloroform for 5 min and then dipped in ethanol several times to wash off the excess PEI.

Pulsed laser deposition

Pt deposition

A Compex 205 KrF excimer laser of Lambda Physik emitting 25 ns pulses at 248 nm was used. Deposition pressures of 10^{-2} mbar to $3x10^{-3}$ mbar were used with argon as background gas. An argon flow was used from 0.2 [1] to 7.5 mlmin^{-1} depending on the

working pressure. A laser fluence of 5 J cm^{-2} was used, with a spot size of ~ 1.95 mm^2. The laser beam entered the vacuum chamber at an angle of 45° with respect to the target normal. The substrate was placed parallel to the target at a distance of 48 mm. The pulse frequency was 5-10 Hz. The (99.99 % pure) Pt target was obtained from Engelhard-CLAL (Drijfhout B.V.) Netherlands.

Alumina deposition

A deposition pressure of 10^{-1} mbar was used with oxygen as background gas. A laser fluence of 3 J cm^{-2} was used, with a spot size of ~ 2.8 mm^2. The laser beam entered the vacuum chamber at an angle of 45° with respect to the target normal. The substrate was placed parallel to the target at a distance of 62 mm. The pulse frequency was 4 Hz.

Electrochemical Cu deposition

The substrates after PLD were used as working electrode and an aqueous solution of $CuSO_4$ (10 mM) and H_2SO_4 (10 mM) as the electrolyte. A Pt mesh functioned as a counter electrode and a 3M KCl Ag/AgCl (Radiometer Analytical REF321) reference electrode was used. The deposition was performed with a BANK Electrotechnik POS73 potentiostat. Cu deposition occurred at 0.05 V vs. reference potential at short-circuited islands. Same deposition conditions were used for the samples.

Measurements

Atomic force microscopy (AFM): The morphology of the nanoparticle-covered surfaces was observed by a digital multimode Nanoscope III (Digital Instruments, Santa Barbara, CA) scanning force microscope, equipped with a J-scanner. All measurements were done at ambient in tapping mode.

Scanning Tunneling Microscopy (STM): The morphology of SAM modified Nb-STO was observed by an EasyScan 2 STM at ambient and at room temperature.

X-Ray Photoelectron Spectroscopy (XPS): Elemental composition was analyzed by a Physical Electronics Quantera Scanning X-ray Multiprobe instrument, equipped with a monochromatic Al Kα X-ray source operated at 1486.7 eV and 25 W. Spectra were referenced to the main C1s peak at 284.80 eV.

Contact Angle (CA): Measurements were done with a Krüss G10 goniometer equipped with a CCD camera. Contact angles were determined automatically during growth of the droplet by a drop shape analysis. Milli-Q water (18.4 MOhm.cm) was used as a probe liquid.

Electrical Measurements: The leakage current density-electric field (J-V) measurements were carried out by applying a dc bias voltage. Measurements of the leakage currents were performed using a Süss MicroTech PM300 Test Systems manual probe station equipped with a Keithley 4200 Semiconductor characterization system (Keithley Instruments GmbH / Germany).

5.5 References

1. Acton, O.; Ting, G.; Ma, H.; Ka, J. W.; Yip, H. L.; Tucker, N. M.; Jen, A. K. Y., *Adv. Mater.* **2008,** *20*, 3697.
2. Collet, J.; Tharaud, O.; Chapoton, A.; Vuillaume, D., *Appl. Phys. Lett.* **2000,** *76*, 1941.
3. Fukuda, K.; Hamamoto, T.; Yokota, T.; Sekitani, T.; Zschieschang, U.; Klauk, H.; Someya, T., *Appl. Phys. Lett.* **2009,** *95*.
4. Acton, O.; Osaka, I.; Ting, G.; Hutchins, D.; Ma, H.; McCullough, R. D.; Jen, A. K. Y., *Appl. Phys. Lett.* **2009,** *95*.
5. Speets, E. A.; Ravoo, B. J.; Roesthuis, F. J. G.; Vroegindeweij, F.; Blank, D. H. A.; Reinhoudt, D. N., *Nano Lett.* **2004,** *4*, 841.
6. Wobkenber, P. H.; Ball, J.; Kooistra, F. B.; Hummelen, J. C.; de Leeuw, D. M.; Bradley, D. D. C.; Anthopoulos, T. D., *Appl. Phys. Lett.* **2008,** *93*.
7. Park, Y. D.; Kim, D. H.; Jang, Y.; Hwang, M.; Lim, J. A.; Cho, K., *Appl. Phys. Lett.* **2005,** *87*.
8. Klauk, H.; Zschieschang, U.; Pflaum, J.; Halik, M., *Nature* **2007,** *445*, 745.
9. Collett, J.; Vuillaume, D., *Appl. Phys. Lett.* **1998,** *73*, 2681.
10. Halik, M.; Klauk, H.; Zschieschang, U.; Schmid, G.; Dehm, C.; Schutz, M.; Maisch, S.; Effenberger, F.; Brunnbauer, M.; Stellacci, F., *Nature* **2004,** *431*, 963.
11. Jedaa, A.; Burkhardt, M.; Zschieschang, U.; Klauk, H.; Habich, D.; Schmid, G.; Halik, M., *Org. Electron.* **2009,** *10*, 1442.
12. Guo, X. G.; Chen, X. S.; Sun, Y. L.; Sun, L. Z.; Zhou, X. H.; Lu, W., *Phys. Lett. A* **2003,** *317*, 501.
13. Akkerman, H. B.; Blom, P. W. M.; de Leeuw, D. M.; de Boer, B., *Nature* **2006,** *441*, 69.
14. Akkerman, H. B.; Kronemeijer, A. J.; van Hal, P. A.; de Leeuw, D. M.; Blom, P. W. M.; de Boer, B., *Small* **2008,** *4*, 100.
15. Shpaisman, H.; Salomon, E.; Nesher, G.; Vilan, A.; Cohen, H.; Kahn, A.; Cahen, D., *J. Phys. Chem. C* **2009,** *113*, 3313.
16. Wold, D. J.; Frisbie, C. D., *J. Am. Chem. Soc.* **2000,** *122*, 2970.
17. Yildirim, O.; Gang, T.; Kinge, S.; Reinhoudt, D. N.; Blank, D. H. A.; van der Wiel, W. G.; Rijnders, G.; Huskens, J., *Int. J. Mol. Sci.* **2010,** *11*, 1162.
18. Gawalt, E. S.; Avaltroni, M. J.; Koch, N.; Schwartz, J., *Langmuir* **2001,** *17*, 5736.
19. Messerschmidt, C.; Schwartz, D. K., *Langmuir* **2001,** *17*, 462.
20. Textor, M.; Ruiz, L.; Hofer, R.; Rossi, A.; Feldman, K.; Hahner, G.; Spencer, N. D., *Langmuir* **2000,** *16*, 3257.
21. Speets, E. A.; Riele, P. T.; van den Boogaart, M. A. F.; Doeswijk, L. M.; Ravoo, B. J.; Rijnders, G.; Brugger, J.; Reinhoudt, D. N.; Blank, D. H. A., *Adv. Funct. Mater.* **2006,** *16*, 1337.
22. Speets, E. A. Deposition of metal islands, metal clusters and metal containing single molecules on self-assembled monolayers. PhD Thesis,University of Twente, Enschede, 2005.
23. te Riele, P. Direct Patterning of Oxides by Pulsed Laser Stencil Deposition. PhD Thesis, University of Twente, Enschede, 2008.

24.   van Rijn, C. J. M.; Veldhuis, G. J.; Kuiper, S., *Nanotechnology* **1998,** *9*, 343.

Chapter 6

Monolayer-directed Assembly and Magnetic Properties of FePt Nanoparticles on Patterned Aluminum Oxide[*]

Abstract: FePt nanoparticles (NPs) were assembled on aluminum oxide substrates, and their ferromagnetic properties were studied before and after thermal annealing. For the first time, phosph(on)ates were used as an adsorbate to form self-assembled monolayers (SAMs) on alumina to direct the assembly of NPs onto the surface. The Al_2O_3 substrates were functionalized with aminobutylphosphonic acid (ABP) or phosphonoundecanoic acid (PUD) SAMs or with poly(ethyleneimine) (PEI) as a reference. FePt NPs assembled on all of these monolayers, but much less on unmodified Al_2O_3, which shows that ligand exchange at the NPs is the most likely mechanism of attachment. Proper modification of the Al_2O_3 surface and controlling the immersion time of the modified Al_2O_3 substrates into the FePt NP solution resulted in FePt NPs assembly with controlled NP density. Alumina substrates were patterned by microcontact printing using aminobutylphosphonic acid as the ink, allowing local NP assembly. Printing NPs using PDMS stamps resulted in ring patterns of the particles. Thermal annealing under reducing conditions ($96\%N_2/4\%H_2$) led to a phase change of the FePt NPs from the disordered FCC phase to the ordered FCT phase. This resulted in ferromagnetic behavior at room temperature. Such a process can potentially be applied in the fabrication of spintronic devices.

6.1 Introduction

Recently, ferromagnetic nanoparticles (FePt NPs) have attracted interest due to their high chemical stability, magnetic properties and small size. This renders them potential candidates for application in spintronic devices, magnetic sensing and ultra-high density data storage.[1-14] FePt NPs have a high magnetocrystalline anisotropy (10^8 erg/cm^3), which should allow the use of small, thermally stable magnetic grains.[1-7] In addition, FePt NPs have a higher chemical stability than other hard magnetic materials.[1] Their well-defined boundaries and small size are very suitable to reach ultra-high storage densities with reduced noise[2,15] in the order of terabit/inch^2. For the use of FePt NPs in magnetic applications, it is necessary to have a well-controlled assembly process and to cover a sizeable area with high packing density.[1-2,10,13] One method used to attach the particles on the surface is by self-assembly with the help of a coupling layer such as poly (ethyleneimine) (PEI)[1] or an aminosilane.[13]

Metal oxides have interesting electronic, optical and magnetic properties and can be insulating, semiconducting, metallic, superconducting, ferroelectric, piezoelectric, ferromagnetic, non-linear optic, colossal magnetoresistant, *etc*.[16-19] They can be grown epitaxially by pulsed laser deposition to have well controlled interfaces.[18,20-23] So far, all studies on the assembly of FePt NPs have focused on SiO$_2$ substrates.[1-5,8-10,13,24] However, for application of nanoparticles in spintronic devices, Al$_2$O$_3$ is an important substrate because it is the dielectric material of choice in electronic device fabrication[25] and the most used dielectric in magnetic tunneling junctions (MTJs).[26-30] The latter consist of two ferromagnetic electrodes separated by an insulating barrier, and they are promising candidates for spintronic devices, in which signal detection is achieved via tunneling magnetoresistance (TMR).[27] The surface properties of Al$_2$O$_3$ can easily be changed by annealing to get an ultra-smooth surface.[31-32]

Self-assembled monolayers (SAMs), in particular thiols on gold and silanes on SiO$_2$, have been studied extensively,[33-34] but SAMs on metal oxides are relatively new. Alkyl phosphates and alkyl phosphonates form SAMs with high ambient stability on metal oxides such as Ta$_2$O$_5$, Al$_2$O$_3$, ZrO$_2$ and TiO$_2$ without the need for controlled environmental conditions.[25,31,35-40]

In this study, we show the assembly of FePt NPs on Al$_2$O$_3$ substrates via ligand exchange on SAMs of PEI, aminobutylphosphonic acid (ABP), or phosphonoundecanoic acid (PUD). The adsorbate molecules are used to direct the

assembly of the FePt NPs on the alumina surface. The FePt coverage is controlled by the surface functionalization and by change of the immersion time. The NPs are assembled onto patterned regions of the substrate by employing microcontact printing. Alumina substrates were patterned by microcontact printing using aminobutylphosphonic acid as the ink, allowing local NP assembly. Microcontact printing was applied to create nano-sized ring patterns of the particles. Thermal annealing is used to achieve a phase transition of the FePt NPs and to provide ferromagnetic behavior at room temperature.[1] Ferromagnetic properties of the NPs are addressed by measuring the magnetic moment (M) as a function of the strength of an applied magnetic field, with a vibrating sample magnetometer (VSM) before and after thermal annealing.

6.2 Results and discussion

FePt NPs were assembled on modified Al2O3 substrates in two steps. Activation of the substrate was induced by a coupling layer, followed by ligand exchange between the surfactants around the NPs and functional groups of the adsorbate on the modified Al$_2$O$_3$ substrates. The NPs are stabilized with the surfactants oleic acid and oleyl amine (Figure 6.1). Oleyl amine binds to Pt through the amino group and oleic acid binds to Fe through the carboxylic acid group.[9] They can be replaced by other acids or amines, or by surfactants with a higher affinity to either Fe or Pt.[9] Thus, adsorbates with terminal amine or carboxylic acid functional groups were chosen (Figure 1). PEI and [3-(2-aminoethylamino)propyl]trimethoxysilane have been used before for binding of particles through ligand exchange.[1, 10, 13]
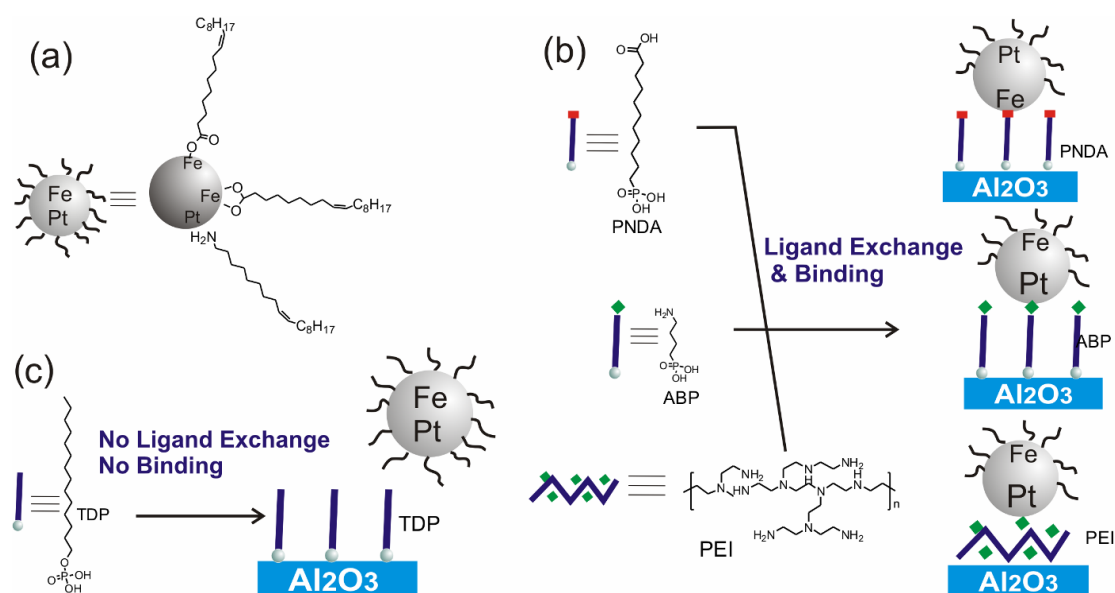
Figure 6.1 (a) FePt NPs stabilized with oleic acid and oleyl amine. (b) Adsorption of FePt NPs occurs through ligand exchange onto amino (aminobutylphosphonic acid, ABP, or poly(ethyleneimine), PEI) and carboxylic acid (phosphonoundecanoic acid, PUD) functionalized monolayer-modified substrates. (c) In case of a methyl-terminated monolayer, (tetradecyl phosphate, TDP), no ligand exchange occurs.

6.2.1 FePt nanoparticles

FePt NPs were prepared by reduction of Pt(acac)$_2$ and decomposition of iron pentacarbonyl in the presence of oleyl amine and oleic acid surfactants, followed by precipitation of the NPs by using ethanol and redispersion in hexane. A drop of a solution of the NPs in hexane was deposited on a carbon-coated copper grid for TEM analysis. The particle size was determined to be 10 ± 2.3 nm as shown in Figure 6.2.
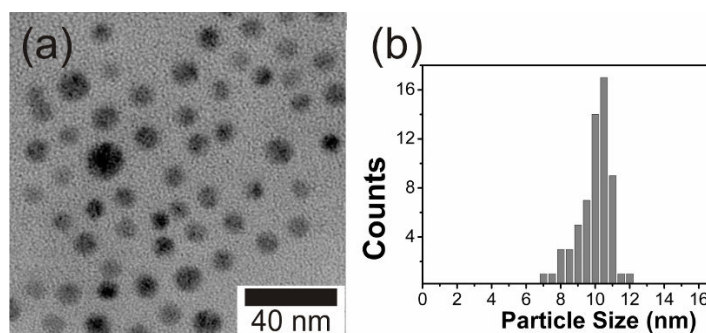

Figure 6.2 (a) TEM image of FePt NPs. (b) Histogram of FePt NPs stabilized with oleyl amine and oleic acid.

To analyze the elemental composition of the NPs, a PEI-covered Al2O3 substrate was immersed into a FePt solution to bind the FePt NPs. After evaporation of the solvent, the sample was analyzed by X-ray photoelectron spectroscopy (XPS), which showed an elemental composition of $Fe_{0.58}Pt_{0.42}$. Due to PEI, C and N were also detected. The ratio of Fe:Pt is close to 1:1, as expected from the synthesis procedure.[1]

6.2.2 SAM formation

The preparation and characterization of monolayer-modified Al_2O_3 substrates was performed according to literature procedures.[25, 31, 35-36, 38-40] Clean Al_2O_3 substrates were immersed into ABP, PUD or TDP solutions for two days at room temperature, rinsed afterwards with solvent and dried under a flow of N_2 to yield amino, carboxylic acid and methyl-functionalized substrates, respectively. Clean Al_2O_3 substrates were immersed into a PEI solution for five minutes and then dipped in ethanol several times to wash off excess PEI to yield amino-functionalized substrates. In the case of PEI-covered alumina, AFM results showed that the surface was smooth and homogeneous (not shown), and XPS verified the presence of C and N. After scratching the PEI layer with an AFM tip, the measured thickness of the PEI layer was around 3.0 nm (not shown). In conclusion, all measurements (Chapter 3) indicate the successful formation of the monolayers on alumina with a high coverage.

6.2.3. Assembly of FePt NPs

Figure 6.3 shows the morphologies of the samples after immersion in the FePt NPs solution. Table 6.1 gives the nanoparticle densities for different surfaces with different immersion times. Figure 3e and a show that NPs are assembled on surfaces with NH_2 and COOH-terminated SAMs, respectively. The section analysis in Figure 6.3e shows that the heights of NPs are around 10 nm, which is in good agreement with particle sizes obtained from TEM. The section analyses of other AFM images indicate similar particle sizes (not shown). Figure 6.3d shows a relatively high coverage and homogeneous distribution of FePt NPs on a PEI-modified Al_2O_3 surface. In case of 15 min immersion time, the density of particles on PEI-modified substrates (Figure 6.3b) is two times higher than the density of the particles at ABP-modified substrates (Figure 6.3c) as shown in Table 1. PEI, with its branched

structure, forms a continuous film on the substrate (Chapter 3), and probably exposes more NH_2 functional groups than an ABP SAM. PEI might have a sloppier packing, thus some chains may stick out to bind the NPs. These resulted in binding of more particles on the PEI-modified surface than on the ABP-modified surface after the same immersion time.

For 10 nm NPs, a maximum coverage of around 40×10^{10} NPs/cm^2 is expected for random packing (assuming half of hexagonal packing). However, the maximum NP coverage reached is about one twentieth of this value. The organic monolayers have high coverage on the alumina substrate and the low degree of particle adsorption is therefore not due to the SAM layer. An increased NP coverage with time is observed (Figure 6.3 and Table 1), indicating the process is not yet over after 90 min immersion. The coverage can potentially be further increased by longer immersion times or by increasing the NP concentration. Additionally, some form of surface aggregation might have occurred due to necking of two or more NPs during NP adsorption, which cannot be resolved by AFM. AFM therefore can give only lower limits, and higher coverages have not been attempted here since AFM analysis would have become useless. As shown in Figure 6.3g, no particles are present on a TDP-modified surface after 90 min immersion. FePt NPs did adsorb on bare Al_2O_3 (Figure 6.3f) but less compared to functionalized surfaces. Of the phosph(on)ate SAMs, PUD-modified Al_2O_3 substrates provide relatively high coverages. The relative rates of binding of NPs on modified surfaces follow ABP<PEI~PUD. The difference in binding kinetics between COOH and NH_2-covered substrates, as between PUD (Figure 6.3a) and ABP (Figure 6.3c) for 15 min immersion, is most likely due to a higher the ligand exchange rate for COOH groups.
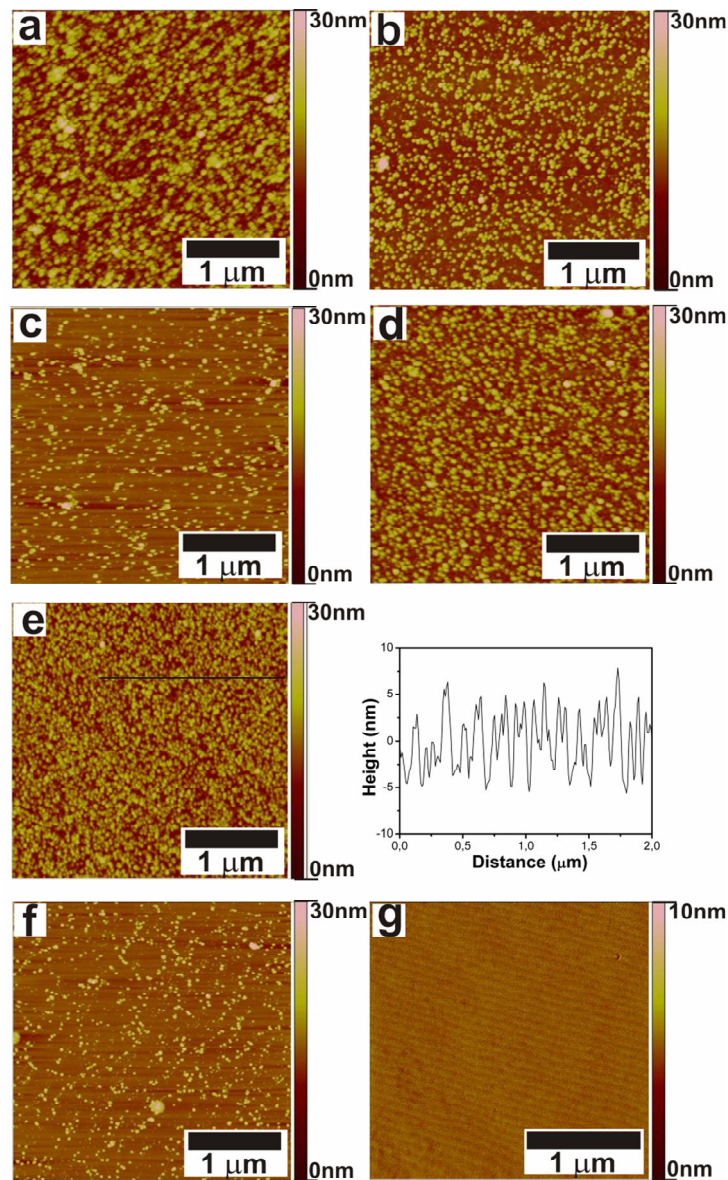
Figure 6.3 AFM images of FePt NPs assembled on (a) PUD-modified Al$_2$O$_3$ substrate, 15 min immersion. (b) PEI-modified Al$_2$O$_3$ substrate, 15 min immersion. (c) ABP-modified Al$_2$O$_3$ substrate, 15 min immersion. (d) PEI-modified Al$_2$O$_3$ substrate, 90 min immersion. (e) ABP-modified Al$_2$O$_3$ substrate, 90 min immersion, with section analysis. (f) Bare Al$_2$O$_3$ substrate, after 90 min immersion. (g) TDP-modified Al$_2$O$_3$ substrate, 90 min immersion.

Table 6.1. FePt NP densities on modified alumina surfaces.

Surface modification	Immersion time (min)	NP density x10^{10} (NPs/cm^2)	Saturation magnetization M (nAm^2)
PUD	15	1.8±0.1	32
PEI	15	1.8±0.1	n.m
ABP	15	1.0±0.05	n.m
PEI	90	2.0±0.1	100
ABP	90	2.2±0.1	32
Bare Al$_2$O$_3$	90	0.8±0.04	n.m
TDP	90	0.0	n.m

*n.m.: not measured

Figure 6.4 shows that individual NPs can still be distinguished after thermal annealing. The apparent NP density after annealing is $(1.27±0.06) \times 10^{10}$ NPs/cm^2 which is lower than the value before annealing which may indicate a certain degree of aggregation. Aggregation of the particles upon annealing is a common problem and the use of linkers to anchor the particles partly prevents this.[9] Yu et. al.[13] have shown that a self-assembled [3-2-aminoethylamino)propyl]trimethoxysilane monolayer was effective to stabilize the FePt NPs on SiO$_2$ surfaces and to prevent coalescence of particles upon annealing.
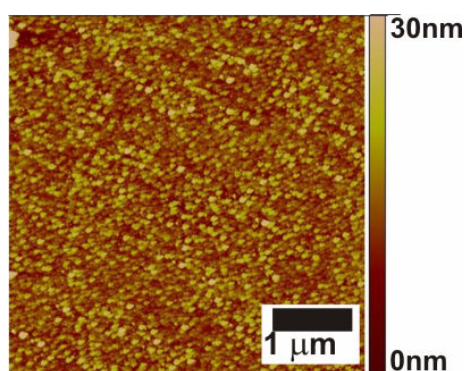

Figure 6.4 AFM image of FePt NPs assembly (90 min) on an ABP-modified Al$_2$O$_3$ substrate, after annealing under reducing environment (96%N$_2$/4%H$_2$) for 1 h at 800 °C.

Microcontact printing was employed to create NP patterns in two different ways. NPs are either printed on ABP functionalized substrate or assembled on a pre-patterned surface prepared by microcontact printing. Figure 6.5 shows the FePt ring patterns on Al_2O_3 substrates prepared by printing the particles onto ABP-modified alumina. The height of the FePt ring corresponds to 2-3 NP layer and the width of patterns is 150-250 nm. By using PDMS with circular patterns in micron range, ring patterns of FePt NPs in nano-scale was produced. The ring shape is achieved probably upon swelling of PDMS due to hexane however control of the resulting pattern size needs optimization of the process.
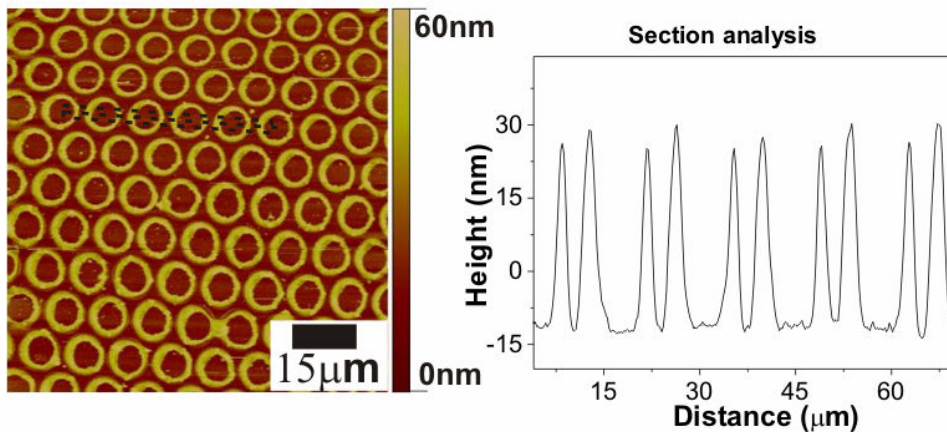

Figure 6.5 AFM images of FePt ring patterns on alumina prepared by printing NPs onto ABP-functionalized monolayer-modified substrate, with section anlysis.

The affinity contrast between bare and ABP-modified alumina was employed to create FePt patterns on the substrate. Printed ABP-patterned alumina substrates were immersed in a FePt solution for 120 min. As seen in Figure 6.6, there is a clear contrast between ABP-covered regions and bare parts due to the preferential assembly of the FePt NPs on the NH_2-terminated areas. NP density at the printed region is $(1.92\pm0.1)\times1010$ NPs/cm^2, similar to the value for ABP-modified Al_2O_3 substrate with 90 min immersion, and at the non-printed region the density is $(0.44\pm0.02)\times1010$ NPs/cm^2. This shows that microcontact printing is an efficient tool to create patterns of FePt NPs by directed assembly.
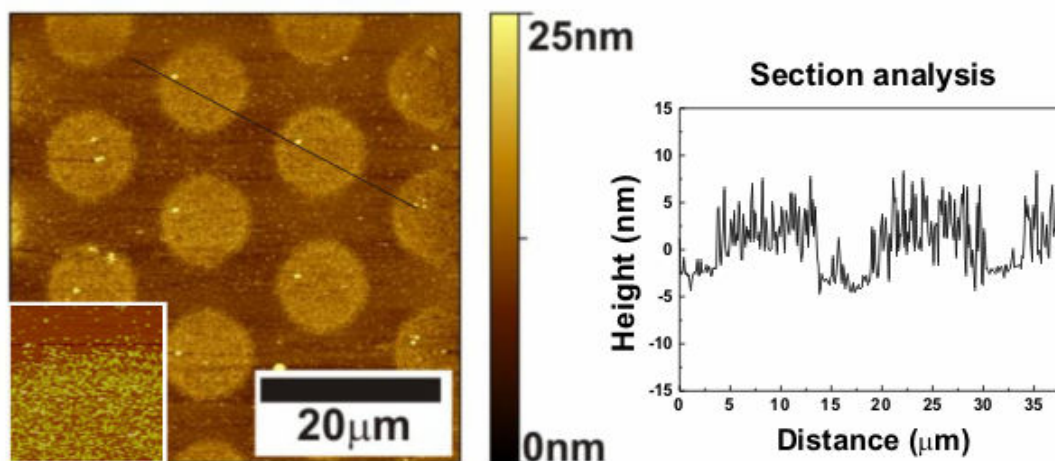
Figure 6.6 AFM image of FePt NPs assembled onto an Al^2O^3 substrate patterned with ABP by microcontact printing, inset is a 3x3 μ^2 AFM image of the same sample at the pattern boundary.

6.2.4 Structural and magnetic properties

To investigate the effect of thermal annealing on the particle crystallinity, a thick layer of FePt NPs was prepared by casting a 20 mg/ml FePt solution on a glass substrate followed by evaporation of the solvent without rinsing and by using the same annealing procedure as described above. Figure 6.7 shows the XRD patterns of the FePt multilayers before and after annealing for 1 h at 800 ^{o}C. It shows the evolution of the superlattice peaks (001) and (110), as well as the fundamental peak (002), which indicates the transformation of the lattice from FCC to FCT ($L1_0$). [41-43]

The magnetic properties of the NPs are related to the crystal structure of the material. To study the effect of phase change upon annealing on the magnetic properties, vibrating sample magnetometer (VSM) measurements were performed. VSM measurements of the annealed FePt NPs on monolayer-covered substrates indicate the distinct ferromagnetic behavior of the NPs at room temperature (Figure 6.8). Upon annealing, all samples showed a considerable increase in coercivity to 200-450 Oe. This shows that the magnetic properties are not related to the type of chemical functionality on the alumina substrates. The values are small compared to reported coercivity values.[1, 13, 41] This may be due to an incomplete phase transformation of the nanoparticles, which might be improved by extension of the annealing time. On the other hand, Skomski et. al.[44] have reported that the decrease of the coercivity for FePt NPs with large particle sizes (> 10 nm) is of micromagnetic

origin, associated with structural imperfections such as polycrystallinity and reduced anisotropy at the surface.
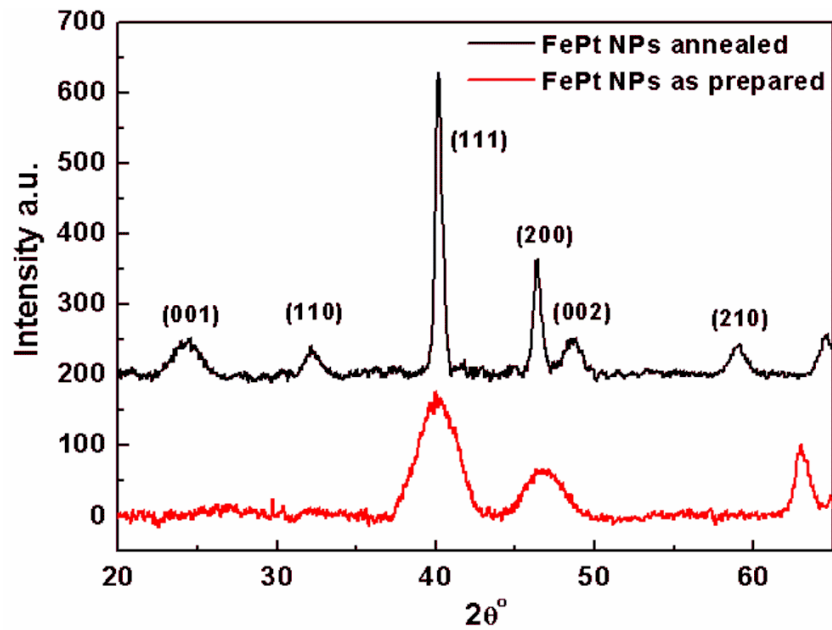

Figure 6.7 XRD patterns of FePt NPs on a glass substrate before (red) and after (black) annealing for 1 h at 800 °C.

For a densely packed monolayer, the expected saturation magnetization *M*, which is related to the volume of FePt, is around 120 nAm^2 based on the momentum density of bulk FePt (1140 emu/cc).[24] The measured intensity of *M* values for the samples are below this value (Table 1, Figure 6.8) which shows that the coverage is on the order of magnitude of a monolayer. Thus, VSM results indicate the actual coverage would be higher than calculated by counting the NPs from AFM images, indicating some degree of aggregation.
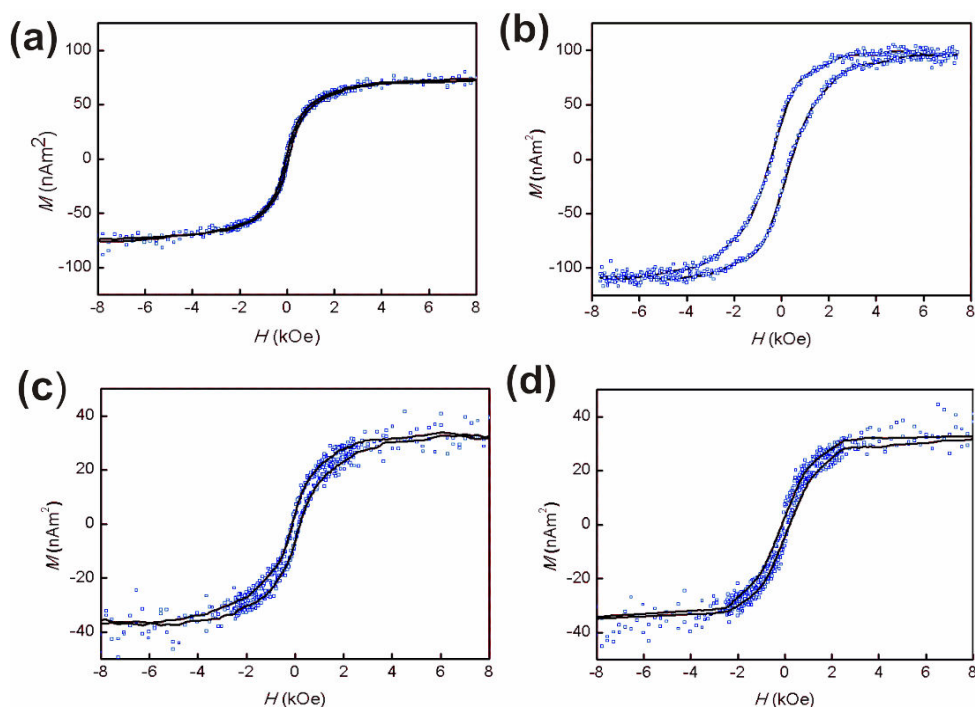
Figure 6.8 In-plane field hysteresis loops of FePt NPs assembled on (a) PEI-modified Al_2O_3 before annealing. (b) PEI-modified Al_2O_3 substrate after annealing. (c) ABP-modified Al_2O_3 substrate after annealing. (d) PUD-modified Al_2O_3 substrate after annealing. Samples were annealed under reducing conditions (96%N_2/4%H_2) for 1 h at 800 $^{\circ}$C

6.3 Conclusions

The NP coverage on Al_2O_3 substrates modified with organic monolayers can be controlled by varying the immersion time into a FePt NPs solution. FePt NPs assemble on ABP, PUD and PEI SAMs, which have NH_2 or COOH functionalities, probably by ligand exchange. This gives the possibility to control the adhesion of NPs on surfaces by changing the surface chemistry. The assembly process results in moderately packed FePt monolayers on SAM-covered Al_2O_3 substrates. Microcontact printing provides the possibility to direct the NP assembly to designated areas of the substrate. Thermal annealing provides phase transition of FePt NPs which results in ferromagnetic behavior at RT. To prevent non-specific adsorption of the NPs on bare substrate regions, making patterned and backfilled monolayers by two types of SAMs may be a suitable way. The here developed process may be used in the fabrication of spintronic devices.

6.4 Experimental

Materials

Polished substrates of R-(1$\bar{1}$02) Al$_2$O$_3$ (1x10x10 mm) were purchased from SurfaceNet GmbH, Germany. These substrates were cut into 5x5 mm^2 pieces with a diamond saw and cleaned by ultrasonication in acetone and ethanol for 30 min each. Tetradecylphosphoric acid (TDP) was supplied by A. Wagenaar and J. Engbersen (RUG, Groningen). Aminobutylphosphonic acid (ABP, purity 99%), phosphonoundecanoic acid (PUD, purity 96%), poly(ethyleneimine) (PEI), Pt(acac)$_2$ and oleic acid were purchased from Sigma-Aldrich. Oleyl amine was purchased from Fluka. Hexadecanediol and iron pentacarbonyl were purchased from ABCR.

Synthesis of FePt NPs

Monolayer-protected FePt NPs were synthesized via a modified method reported by *Sun et al.*[1] A solution of 0.25 mmol Pt(acac)$_2$ and 0.75 mmol 1,2-hexadecanediol in 20 mL octyl ether was heated to 80°C, and to this solution 0.5 mmol oleic acid, 0.5 mmol oleyl amine and 0.5 mmol Fe(CO)$_5$ were added via a syringe under a fume hood. Caution: the decomposition of Fe(CO)$_5$ produces CO, which is potentially lethal. The mixture was further heated to 150°C for 1 h. The black product was precipitated using ethanol and the particles were redispersed in hexane. This procedure was reported to yield a 1:1 Fe:Pt ratio in the NPs. [1, 9]

Sample Preparation

Oxygen plasma cleaned Al$_2$O$_3$ substrates were immersed into 1 mM ABP solution in 100:1 v/v hexane:isopropanol, a 1 mM PUD solution in 50:50 v/v ethanol:H$_2$O, or a 0.125 mM TDP solution in 100:1 v/v hexane:isopropanol for two days at room temperature. Afterwards, the samples were rinsed with the corresponding pure solvents or solvent mixtures, and dried under a flow of N$_2$. In the case of PEI, clean substrates were immersed in a 20 mg/ml PEI solution in chloroform for five min and then dipped in ethanol several times to wash off excess PEI.

Microcontact Printing

Silicon masters with micrometer-sized features were fabricated by photolithography. PDMS stamps were prepared from commercially available Sylgard-184 poly(dimethylsiloxane) (Dow Corning). The curing agent and the prepolymer were manually mixed 1:10 volume ratio and cured overnight at 60 °C against the master. The cured stamp was peeled off from the master at the curing temperature. Before printing, the stamps were rinsed with pure ethanol and dried under a flow of N$_2$. The

stamps were inked with a few drops of solutions of ABP in water. For ABP, an oxidized stamp was used.[45-46] The stamps were dried with N_2 and brought into conformal contact with alumina substrates for five min. After removing the stamp, the sample was rinsed with ethanol to wash off excess ink followed by drying under nitrogen.

Nanoparticle Assembly

Al_2O_3 substrates covered with a self-assembled monolayer (SAM) of TDP, ABP, PUD, a thin layer of PEI or with a printed ABP pattern were immersed into a FePt (1 mg/ml) solution for 15-120 min to assemble FePt NPs on the modified Al_2O_3 surfaces. As a control experiment, a bare alumina substrate was also immersed into the FePt solution for 90 min. Subsequently, the samples were rinsed with pure hexane to wash off physisorbed particles and imaged by AFM.

Thermal Annealing

To obtain the chemically ordered face-centered tetragonal (FCT) $L1_0$ phase, which results in ferromagnetic behavior at room temperature, the FePt-covered substrates were annealed in a reducing environment ($96\%N_2/4\%H_2$) for 1 h at 800 ^{o}C.

Measurements

Atomic force microscopy (AFM): The morphology of the nanoparticle-covered surfaces was observed by a digital multimode Nanoscope III (Digital Instruments, Santa Barbara, CA) scanning force microscope, equipped with a J-scanner. All measurements were done at ambient in tapping mode or contact mode.

The approximate nanoparticle densities were calculated by counting particles at a certain area. For instance, in the case of assembly on a PEI modified Al_2O_3 substrate with 90 min immersion time, counting was done on the AFM image at three different areas, the average densities were calculated, and a standard deviation of 5% was found, which was assumed similar for the other samples.

Vibrating Sample Magnetometer (VSM): Magnetic studies were carried out using a DMS Vibrating Sample Magnetometer (model VSM10) with fields up to 1500 kA/m and a sensitivity of 10^{-6} mAm^2. Measurements were done on NP assemblies on ABP, PUD and PEI-modified Al_2O_3 substrates.

X-Ray Diffractometry (XRD): The nanoparticle samples after annealing were analyzed by powder XRD analysis using a Philips X'Pert diffractometer ($CuK_\alpha \lambda = 1.5418$ Å).

X-Ray Photoelectron Spectroscopy (XPS): Elemental composition was analyzed by a Physical Electronics Quantera Scanning X-ray Multiprobe instrument, equipped with

a monochromatic Al Kα X-ray source operated at 1486.7 eV and 25 W. Spectra were referenced to the main C1s peak at 284.80 eV.

Fourier Transform Infrared Spectroscopy (FTIR): Reflection-FTIR spectra of 1024 scans at 4 cm^{-1} were obtained using a BioRad FTS-60A spectrometer with a liquid nitrogen-cooled cryogenic mercury cadmium telluride detector and RAS accessory (BIO-RAD).

Contact Angle (CA): Measurements were done with a Kruss G10 goniometer equipped with a CCD camera. Contact angles were determined automatically during growth of the droplet by a drop shape analysis. Milli-Q water (18.4 MOhm.cm) was used as a probe liquid.

High-Resolution Transmission Electron Microscopy (HRTEM): Particle sizes were analyzed by TEM (Philips CM-30 Twin operating at 200 kV voltage). A drop of NP solution in hexane was deposited on a carbon-coated copper grid.

6.5 References

1. Sun, S. H.; Anders, S.; Thomson, T.; Baglin, J. E. E.; Toney, M. F.; Hamann, H. F.; Murray, C. B.; Terris, B. D., J. Phys. Chem. B 2003, 107, 5419.
2. Acet, M.; Mayer, C.; Muth, O.; Terheiden, A.; Dyker, G., J. Cryst. Growth 2005, 285, 365.
3. Huang, T. W.; Huang, Y. H.; Tu, T. H.; Lee, C. H., J. Magn. Magn. Mater. 2004, 282, 127.
4. Huang, T. W.; Yu, K. L.; Liao, Y. F.; Lee, C. H., Coll. Surf. A 2006, 284, 603.
5. Huang, T. W.; Yu, K. L.; Liao, Y. F.; Lee, C. H., J. Appl. Crystallogr. 2007, 40, S480.
6. Hyeon, T., Chem. Commun. 2003, 927.
7. Jeong, U.; Teng, X. W.; Wang, Y.; Yang, H.; Xia, Y. N., Adv. Mater. 2007, 19, 33.
8. Lee, S. J.; Yu, A. C. C.; Lo, C. C. H.; Fan, M., Phys. Status. Solidi. A-Appl. Res. 2004, 201, 3031.
9. Sun, S. H., Adv. Mater. 2006, 18, 393.
10. Sun, S. H.; Anders, S.; Hamann, H. F.; Thiele, J. U.; Baglin, J. E. E.; Thomson, T.; Fullerton, E. E.; Murray, C. B.; Terris, B. D., J. Am. Chem. Soc. 2002, 124, 2884.
11. Sun, S. H.; Murray, C. B.; Weller, D.; Folks, L.; Moser, A., Science 2000, 287, 1989.
12. Tartaj, P.; Morales, M. P.; Gonzalez-Carreno, T.; Veintemillas-Verdaguer, S.; Serna, C. J., J. Magn. Magn. Mater. 2005, 290, 28.
13. Yu, A. C. C.; Mizuno, M.; Sasaki, Y.; Inoue, M.; Kondo, H.; Ohta, I.; Djayaprawira, D.; Takahashi, M., Appl. Phys. Lett. 2003, 82, 4352.
14. Zeng, H.; Sun, S. H.; Sandstrom, R. L.; Murray, C. B., J. Magn. Magn. Mater. 2003, 266, 227.
15. Schrefl, T.; Hrkac, G.; Suess, D.; Scholz, W.; Fidler, J., J. Appl. Phys. 2003, 93, 7041.
16. Ahn, C. H.; Triscone, J. M.; Mannhart, J., Nature 2003, 424, 1015.
17. Dagotto, E., Science 2005, 309, 257.
18. Hwang, H. Y., MRS Bull. 2006, 31, 28.
19. Schlom, D. G.; Chen, L. Q.; Pan, X. Q.; Schmehl, A.; Zurbuchen, M. A., J. Am. Ceram. Soc. 2008, 91, 2429.

20. Delage, T.; Champeaux, C.; Catherinot, A.; Seaux, J. F.; Madrangeas, V.; Cros, D.; Pailloux, F.; Gaboriaud, R. J., Thin Solid Films 2004, 453, 273.
21. Huijben, M.; Rijnders, G.; Blank, D. H. A.; Bals, S.; Van Aert, S.; Verbeeck, J.; Van Tendeloo, G.; Brinkman, A.; Hilgenkamp, H., Nat. Mater. 2006, 5, 556.
22. Yamaki, T.; Sumita, T.; Yamamoto, S.; Miyashita, A., J. Cryst. Growth 2002, 237, 574.
23. Zhao, H.; Hu, L. Z.; Wang, Z. Y.; Wang, Z. J.; Zhang, H. Q.; Zhao, Y.; Liang, X. P., J. Cryst. Growth 2005, 280, 455.
24. Kinge, S.; Gang, T.; Naber, W. J. M.; Boschker, H.; Rijnders, G.; Reinhoudt, D. N.; van der Wiel, W. G., Nano Lett. 2009, 9, 3220.
25. Sun, S. Q.; Leggett, G. J., Nano Lett. 2007, 7, 3753.
26. Kita, T.; Chiba, D.; Ohno, Y.; Ohno, H., Appl. Phys. Lett. 2007, 90, 3.
27. Oleynik, II; Tsymbal, E. Y., Interface Sci. 2004, 12, 105.
28. Schmalhorst, J.; Reiss, G., J Magn Magn Mater 2004, 272, E1485.
29. Wang, D. X.; Nordman, C.; Daughton, J. M.; Qian, Z. H.; Fink, J., IEEE Trans. Magn. 2004, 40, 2269.
30. Yuasa, S.; Nagahama, T.; Suzuki, Y., Science 2002, 297, 234.
31. Messerschmidt, C.; Schwartz, D. K., Langmuir 2001, 17, 462.
32. Yoshimoto, M.; Maeda, T.; Ohnishi, T.; Koinuma, H.; Ishiyama, O.; Shinohara, M.; Kubo, M.; Miura, R.; Miyamoto, A., Appl. Phys. Lett. 1995, 67, 2615.
33. Onclin, S.; Ravoo, B. J.; Reinhoudt, D. N., Angew. Chem. Int. Ed. 2005, 44, 6282.
34. Schreiber, F., Prog Surf. Sci. 2000, 65, 151.
35. Gawalt, E. S.; Avaltroni, M. J.; Koch, N.; Schwartz, J., Langmuir 2001, 17, 5736.
36. Gnauck, M.; Jaehne, E.; Blaettler, T.; Tosatti, S.; Textor, M.; Adler, H. J. P., Langmuir 2007, 23, 377.
37. Hahner, G.; Hofer, R.; Klingenfuss, I., Langmuir 2001, 17, 7047.
38. Liakos, I. L.; Newman, R. C.; McAlpine, E.; Alexander, M. R., Langmuir 2007, 23, 995.
39. Pawsey, S.; Yach, K.; Reven, L., Langmuir 2002, 18, 5205.
40. Textor, M.; Ruiz, L.; Hofer, R.; Rossi, A.; Feldman, K.; Hahner, G.; Spencer, N. D., Langmuir 2000, 16, 3257.
41. Harrell, J. W.; Nikles, D. E.; Kang, S. S.; Sun, X. C.; Jia, Z.; Shi, S.; Lawson, J.; Thompson, G. B.; Srivastava, C.; Seetala, N. V., Scr. Mater. 2005, 53, 411.
42. Kang, S. S.; Jia, Z. Y.; Nikles, D. E.; Harrell, J. W., IEEE Trans. Magn. 2003, 39, 2753.
43. Yu, C. H.; Caiulo, N.; Lo, C. C. H.; Tam, K.; Tsang, S. C., Adv. Mater. 2006, 18, 2312.
44. Skomski, R.; Liu, J. P.; Rong, C. B.; Sellmyer, D. J., J. Appl. Phys. 2008, 103, 3.
45. Rozkiewicz, D. I.; Kraan, Y.; Werten, M. W. T.; de Wolf, F. A.; Subramaniam, V.; Ravoo, B. J.; Reinhoudt, D. N., Chem. Eur. J. 2006, 12, 6290.
46. Rozkiewicz, D. I.; Ravoo, B. J.; Reinhoudt, D. N., Langmuir 2005, 21, 6337.

Chapter 7

Nano-patterned monolayer and multilayer structures of FePtAu nanoparticles on aluminum oxide prepared by nanoimprint lithography and nanomolding in capillaries

Abstract: Owing to the superior dielectric property of aluminum oxide, precise patterning of self-assembled monolayers (SAMs) and nanoparticles (NPs) on aluminum oxide substrates is highly interesting for generating SAM or NP-based electronic devices. This study employed nanoimprint lithography (NIL) and nanomolding in capillaries (NAMIC) for patterning magnetic NPs on aluminum oxide substrates. We demonstrated the fabrication of structured arrays of various SAMs and NPs in micrometer and nanometer ranges. The polymer template generated by NIL behaved as a physical barrier and defined the pattern areas on the substrate. FePtAu NPs were assembled on phosph(on)ate SAM-modified polymer patterned substrates. After polymer removal, nano and micro scale, line and dot NP patterns, with controlled layer thickness, were obtained on aluminum oxide substrates. Thick nanolines of NPs were obtained by NAMIC. PO_3-terminated FePtAu NPs were assembled on alumina without need of a linker. Applying an external magnetic field during the assembly of ferromagnetic FePtAu NPs on aminobutylphosphonic acid (ABP) modified $SrTiO_3$ (STO) resulted in angle-dependent magnetic properties which shows partial alignment of the NPs. The magnetic properties of the ferromagnetic NPs were addressed by vibrating sample magnetometry (VSM) and those of the patterned NPs by magnetic force microscopy (MFM).

7.1 Introduction

The nano/micro particle-based magnetic tunnel junctions have attracted special attention since an enhanced magnetoresistance was observed compared to thin multilayer-based magnetic tunnel junctions.[1] The core component of such devices is a multilayer of granular magnetic particles embedded in an insulating matrix such as aluminum oxide.[1]

Practically, nanoparticle assemblies with small size distributions and shape variations may lead to ultra small magnetic devices.[2-3] However, energy and cost efficient production of such magnetic nanoparticle-based devices is still an issue. The chemically synthesized FePt magnetic nanoparticles offer a new possibility to address this. Chemically prepared FePt nanoparticles have high chemical stability, strong magnetic properties and very small size distributions.[4-5] The size of these nanoparticles is from a few nanometers to tens of nanometers. To make magnetic devices out of these nanoparticles, it is essential to have a well-controlled patterning and assembly method[6-9] to position the magnetic nanoparticles on highly insulating substrates such as aluminum oxide which is widely used as the dielectric material in magnetic tunneling junctions (MTJs).

Photo-patterned SAMs on metal oxides have been used to grow inorganic films, as etch resists or to attach nanoparticles.[10-11] A contact printing method was demonstrated to create $Pt@Fe_2O_3$ core-shell nanoparticle patterns on silicon substrates.[12] In this case the dimension, thickness and shape of the patterns are limited by the constraints of the fabrication process. In Chapter 6, the directed assembly of nanoparticles on pre-patterned alumina substrates was introduced where the assembly of FePt NPs took place preferentially on the chemically active patterned regions. However, also some nonspecific binding occurred on the bare substrate areas.

Given the above problems, high resolution and robust patterning of magnetic nanoparticles with high contrast on bare and NP-patterned regions on aluminum oxide substrates is important. In this study, we show the preparation of ferromagnetic FePtAu NP patterns in the micrometer and nanometer scale on aluminum oxide by combining SAM and NIL. An external magnetic field is applied during assembly to attempt to magnetically align the FePtAu nanoparticles. PO_3-terminated FePtAu NPs are assembled on alumina in order to avoid the need for a linker. Ferromagnetic

properties of the NPs and NP patterns were addressed with a vibrating sample magnetometre (VSM) and magnetic force microscopy (MFM), respectively.

7.2 Results and discussion

To prepare patterns of SAMs and FePt or FePtAu NPs on Al_2O_3 substrates, a combined NIL and self-assembly method was used. NIL enables high resolution and prevents non-specific assembly. The NPs were stabilized with the surfactants oleic acid and oleyl amine (Figure 7.1). Oleyl amine binds to Pt through the amino group and oleic acid binds to Fe through the carboxylic acid group.[13] They can be replaced by other acids or amines, or by surfactants with a higher affinity to either Fe or Pt.[13] Thus, adsorbates with amine or carboxylic acid terminations were chosen (Figure 7.1). By using FePtAu NPs instead of FePt, thermal annealing after assembling the NPs on the surface is not necessary to obtain ferromagnetic properties at room temperature,[4] preventing possible aggregation which has been reported as a common problem due to thermal annealing.[6, 14-15]
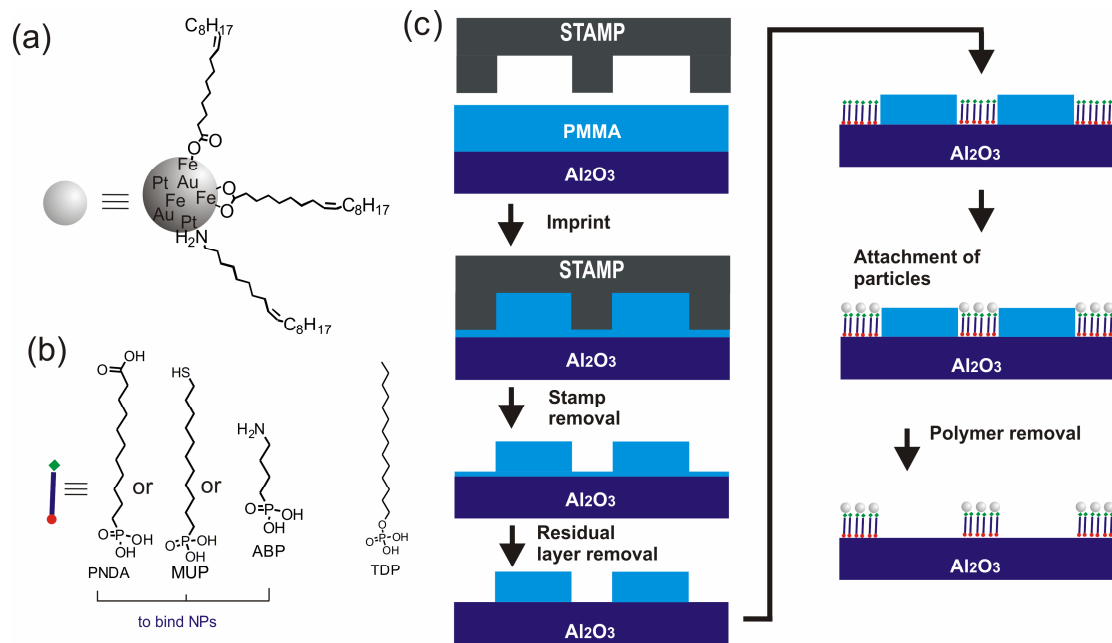

Figure 7.1 (a) FePtAu NPs stabilized with oleic acid and oleyl amine. (b) The organic molecules used to attach NPs. (c) Patterns of NPs are formed by attachment through ligand exchange onto amino (aminobutylphosphonic acid, ABP), carboxylic acid (phosphonoundecanoic acid, PUD), and thiol (mercaptoundecylphosphonic acid, MUP) functionalized monolayer-modified substrates.

7.2.1 FePtAu nanoparticles

NPs were prepared by reduction of $Pt(acac)_2$ and $Au(acac)$, decomposition of iron pentacarbonyl in the presence of oleyl amine and oleic acid surfactants and solution annealing, followed by precipitation of the NPs by using ethanol and redispersion in hexane. A drop of a solution of the NPs in hexane was deposited on a carbon-coated copper grid for TEM-EDX analysis. EDX analysis showed an elemental composition of $Fe_{57}Pt_{31}Au_{12}$. The particle size was determined by TEM to be ~4 nm (Figure 7.2b). From Scherrer analysis from an XRD measurement made on a thick layer of FePtAu, a diameter of 3.56 nm was calculated, close to the TEM value (Figure 7.2a) (NPs prepared by casting a 20 mg/ml FePtAu solution on a glass substrate followed by evaporation of the solvent without rinsing). FePtAu NP assembly on an MUP-modified Al_2O_3 substrate resulted in a monolayer coverage of NPs with a density of $(1.44\pm0.1)x10^{10}$ NPs/cm^2 (AFM not shown). FePtAu NPs assembled on MUP-modified Al_2O_3 were ferromagnetic, as studied by VSM, at room temperature without annealing (75 Oe).
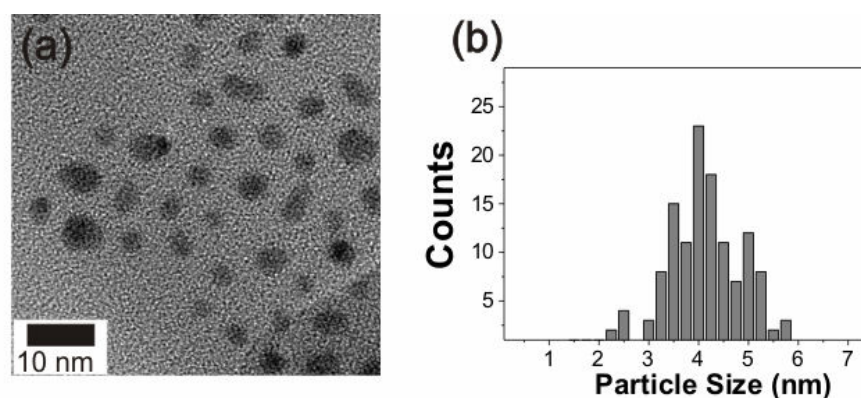

Figure 7.2 (a) TEM image of FePtAu NPs. (b) Histogram of FePtAu NPs stabilized with oleyl amine and oleic acid.

7.2.2 PO$_3$-terminated FePtAu nanoparticles (PO$_3$-NPs)

The PO$_3$-NPs were prepared from methyl-terminated FePtAu NPs (Figure 7.1a) through ligand exchange with MUP (Figure 7.1b) using a modification of the procedure reported by Bagaria *et al.*[16] The particles were dispersed in ethanol:Et$_3$N (10:1). The particle size is assumed to be the same as the FePtAu NPs (~ 4 nm).

FePt nanoparticles with ~ 4 nm diameter and 10 kOe coercivity after annealing, were prepared by a similar method as described in chapter 6.

7.2.3 SAM formation

The preparation and characterization of TDP, ABP, MUP and PUD monolayer-modified Al$_2$O$_3$ substrate were discussed in Chapter 3, and were performed according to literature procedures.[11, 17-21]

7.2.4 Assembly of FePtAu NPs under magnetic field

An ABP-modified SrTiO$_3$ substrate was immersed in a dilute FePtAu NP solution 30 h at 4 $^{\circ}$C in a magnetic field of 7000 Oe in order to align the NPs during assembly on the substrate surface. The NPs were ferromagnetic (75 Oe coercivity) before assembly. The magnetic field was applied in a direction parallel to the surface of the substrate. ABP functionalization of the substrate surface is preferred since it provides lower binding kinetics for NPs compared to PUD or MUP. This is expected to favor the magnetic alignment of the NPs since there is more time for the NPs to rotate in the solution before they are fixed to the surface by ABP. Afterwards the sample was rinsed with hexane to remove physisorbed particles. Angle-dependent VSM was performed to investigate the effect of the external magnetic field during assembly on the alignment of the NPs. Figure 7.3a shows two important magnetic properties, coercivity H_c and remanence M_r,[13] as a function of the angle of the magnetic field during the VSM measurement, applied in the plane of the sample. The observed angle dependence of H_c and M_r means that at least some particles are aligned along their easy axis, most likely due to the effect of the external magnetic field applied during assembly. [22]

As a control experiment, the magnetic properties of a similar sample with particles assembled without any external magnetic field were determined. As seen in Figure 7.3b, the magnetic properties show no dependence on measurement angle, which indicates the particles are randomly oriented on the surface. This is expected when there is no external driving force to align the NPs.

The H_c vs field angle data were fitted with a model[23-24] that describes the coercive field strength by domain wall pinning, taking into account magnetization rotation in the magnetic domains, which is influenced by the anisotropy strength K_u. The H_c curve observed is typical for this behavior: H_c increases when the angle of the applied field with the easy axis increases, and drops towards zero for an angle close to the hard axis orientation. This behavior is opposite to that of a system where

magnetization reversal is governed by coherent rotation, in which H_c decreases to zero with increasing field angle.
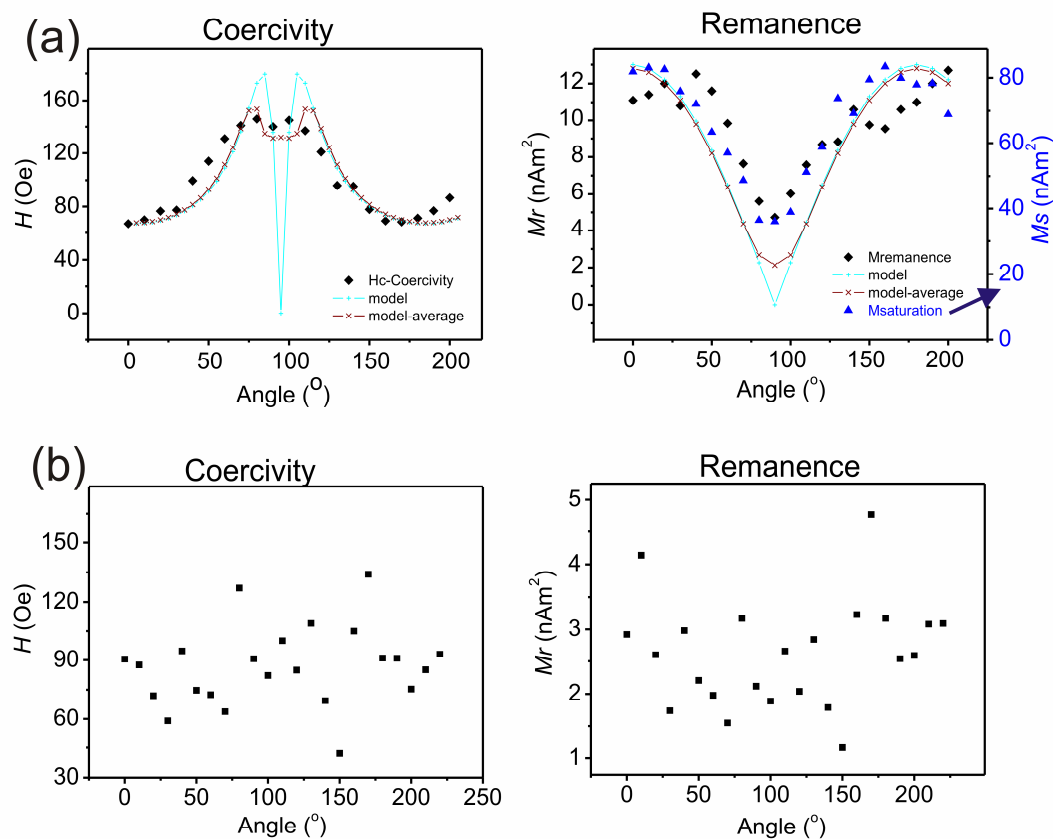

Figure 7.3 The angular dependence of coercivity and remanence for partially ferromagnetic FePtAu NPs assembled on ABP-modified $SrTiO_3$ in the presence (a) or absence (b) of a 7000 Oe external magnetic field. In the model for M_r and H_c one uniaxial easy axis is assumed and in the average model, easy axis is assumed to spread over a range (-12 to 12 degrees).

Here, each NP is assumed as a single spherical domain. It is possible that some of the NPs are fixed to the substrate before they are fully aligned. Therefore, the uniaxial direction is assumed to be spread over a range of approximately -12 to 12 degrees. The averaging over easy axis directions rounds the sharp minimum of the models for M_r and H_c fits, but the order of magnitude of the obtained K_u value does not change much by the averaging. Assuming that a fraction of the NPs are ferromagnetic with literature saturation magnetization values[22] (M_s=1.14 MA/m) the anisotropy energy is found as K_u=7.35 MJ/m^3 which is nearly equal to the bulk value

reported in literature.[22] For M$_r$, the trend of the model is similar to the experimental results. Furthermore, we found that also M$_s$ is angle dependent. We do not have an explanation for this observation.

We did not determine quantitatively the time scale on which the particles align and whether the alignment happens already in the solution or when they are on the surface. However, since similar experiments with a PUD-modified substrate, which would cause stronger binding, did not show any indication of alignment after 30 min assembly, it is likely that alignment is happening at the surface.

7.2.5 Assembly of PO$_3$-terminated FePtAu NPs

MUP-stabilized PO$_3$-NPs (Figure 7.4a) allows direct assembly of NPs onto an Al$_2$O$_3$ surface without the need for a linker. Figure 7.4 shows the morphology of the alumina sample after immersion in the PO$_3$-NP solution for 180 min. The NP density is $(4.2\pm0.2)x10^{10}$ NPs/cm^2. This is 5 times higher than the NP density for FePt on bare Al$_2$O$_3$ after 90 min immersion (Chapter 6) which shows that the PO$_3$-NPs are probably attached to the surface through the PO$_3$ groups and that the high density is not due to non-specific adsorption. This kind of particles may be assembled on pre-patterned surfaces protected by methyl terminated regions to create NP patterns.
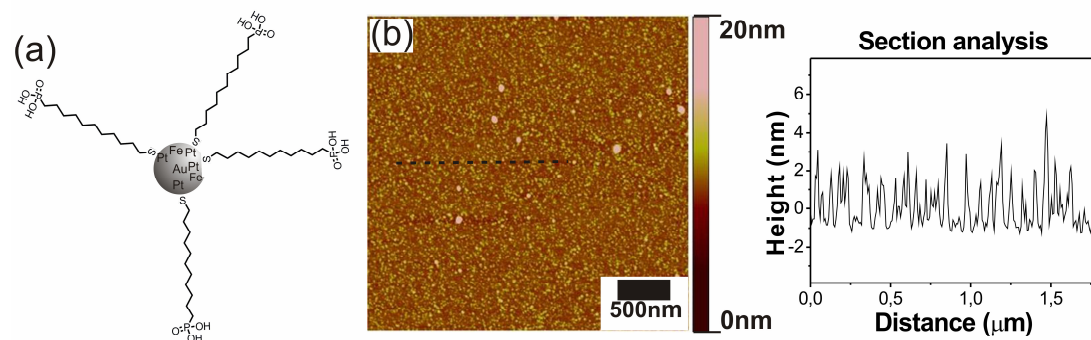

Figure 7.4 (a) MUP-stabilized PO$_3$-terminated FePtAu NPs (PO$_3$-NP) (b) AFM image and section analysis of the PO$_3$-NPs assembled on a bare Al$_2$O$_3$ substrate after 180 min immersion.

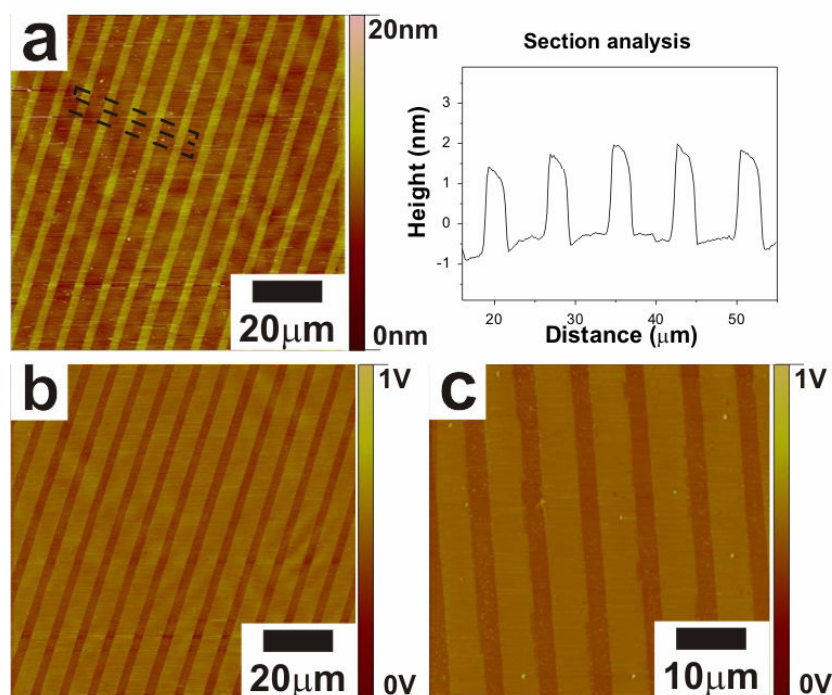**7.2.6 SAM patterns prepared by NIL**

Figure 7.5 Contact-mode height (a) and friction (b)AFM images of 5 µm lines of tetradecylphosphate (TDP) on Al_2O_3 with 8 µm period; (c) friction AFM image after subsequent evaporation of an amino alkyl silane. In the friction images, brighter areas indicate higher friction.

Tetradecylphosphate (TDP) SAM lines were prepared as described in Figure 7.1. The residual layer was removed by oxygen plasma which enabled anisotropic etching and positive transfer of the mold features onto the substrate. A uniform TDP pattern was formed with homogeneous thickness, corresponding to one SAM layer (Figure 7.5a). Nanopatterns of TDP SAMs were also prepared with a similar method but it was not possible to get a clear image probably due to the quite small size of the patterns. Alumina appears bright in the friction image (Figure 7.5) because of a higher friction force relative to the TDP area. The TDP pattern was back-filled with *N*-[3-(trimethoxysilyl)propyl)ethylene]-diamine from gas phase to chemically pattern the substrate with two different kinds of SAMs. The friction force of the more hydrophilic NH_2-terminated area is higher compared to the CH_3-terminated TDP region (Figure 7.5c).

7.2.7 Nanoparticle pattern preparation by NIL and SAMs

Figure 7.6 shows the morphologies of the FePtAu patterns on Al$_2$O$_3$ substrates prepared by NIL and self-assembly as described in Figure 7.1. PMMA was spin-coated on Al$_2$O$_3$ substrates with 460 nm and 120 nm thickness for micron and nanosize patterning, respectively. NIL was performed at a pressure of 40 bar at 180 ^{o}C. The residual layer was removed by oxygen plasma etching (RIE). The particles assembled on NH$_2$, SH and COOH terminated SAM patterns. Figure 7.6 a,b shows that lines of FePtAu below 200 nm width formed by using a nano-mold and PUD as the linker. The heights of the FePtAu NP patterns were around 6 nm which shows a monolayer coverage. For the micron patterns, a similar height of FePtAu NP features was observed (not shown). An important advantage of nanoimprint lithography is the good edge definiton. When compared to NP patterns prepared by using microcontact printing (Chapter 6), NIL patterns have well defined edges, and better contrast between patterned and bare regions. The FePtAu NP densities were similar for MUP and PUD-patterned surfaces, $(1.6\pm0.1) \times 10^{10}$ and $(1.5\pm0.1) \times 10^{10}$ NPs/cm^2, respectively. Since a similar coverage was reached with immersion time of 10 min for -SH and -COOH-modified surfaces, the relative rates of binding of NPs on modified surfaces are similar for MUP and PUD (Chapter 6).
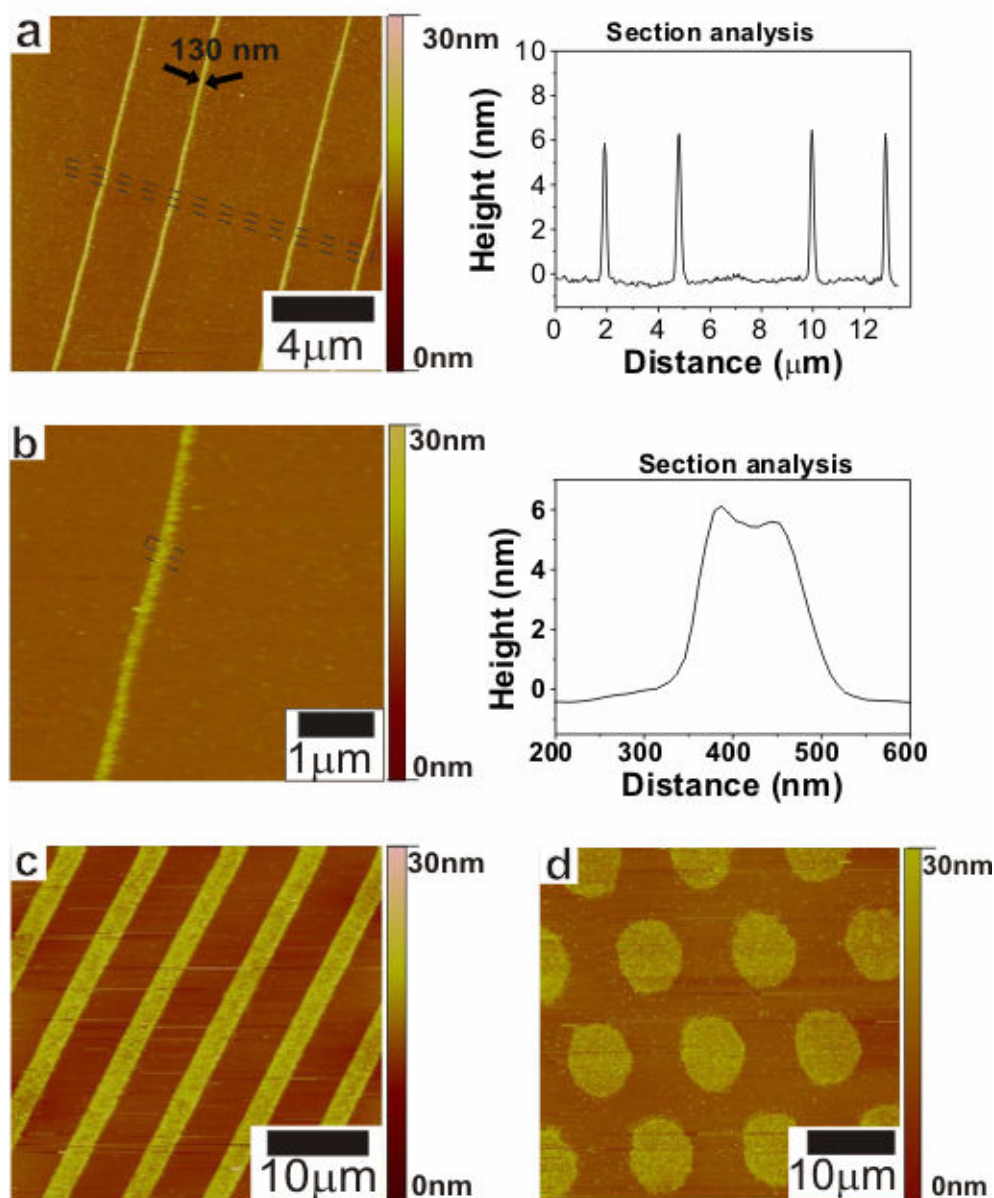
Figure 7.6 Tapping-mode (TM) AFM height images of nanoparticles adsorbed on SAM-modified Al_2O_3 substrates. FePtAu nanoparticles, (a, b) 130 nm wide PUD lines, 10 min immersion, (c) 3 μm PUD lines, 10 min immersion, (d) 10 μm MUP dots, 10 min immersion.

The shape of the patterns are defined by the shape of the mold. As seen in Figure 7.6d, dot patterns can also be prepared as well as lines. The lateral dimensions of the patterns were in good agreement with the feature size of the molds. The process is not limited to FePt NPs, any particle or molecule which has affinity to the end group of the SAM layer can bind to the surface to form a pattern.

7.2.8 Electroless deposition of Ag

As an application to use the patterned FePtAu NPs, Ag was grown by electroless deposition on NP patterns prepared by NIL and linked to Al$_2$O$_3$ by MUP. AgNO$_3$ and NaBH$_4$ solutions were used to deposit Ag ions and form SAg nucleation sites there to initiate Ag electroless deposition (Figure 7.7a). In another experiment, Ag was grown directly, relying on possible surfactant free sites on FePtAu NP surfaces which would initiate the Ag electroless deposition (Figure 7.7b). In both cases, a Ag layer of 30-60 nm was formed within 20 min.
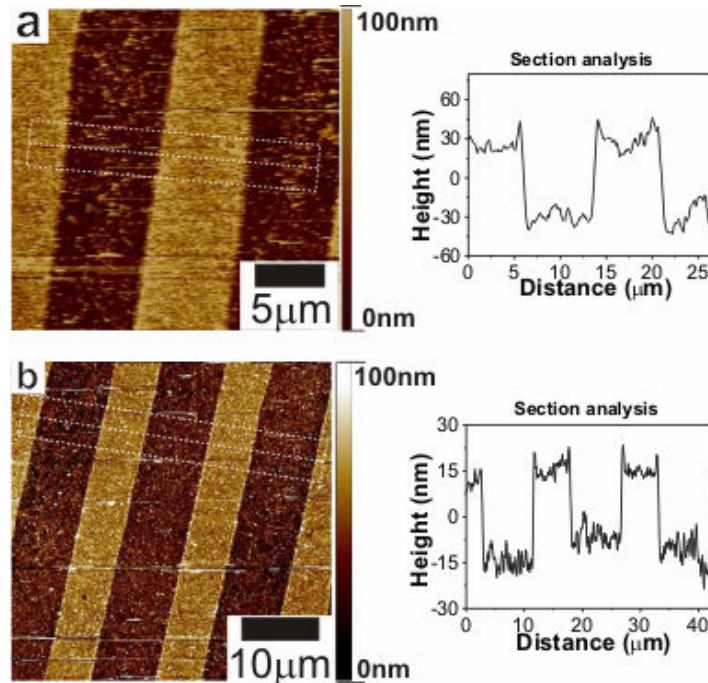
Figure 7.7 Tapping-mode (TM) height AFM images of Ag lines prepared by electroless deposition on MUP-FePtAu patterns on alumina, by (a) forming SAg nucleation sites, (b) direct growth without activation.

7.2.9 Multilayers of FePt NPs prepared by NIL

The magnetic properties of patterned FePt NPs were studied with MFM, which is known to be a powerful technique for studying patterned magnetic structures.[12] It can effectively separate the magnetic from the topographical information of the sample. Due to the magnetic interaction between the magnetic dipoles of the sample and the tip, a phase contrast is observed which gives information on the magnetic state independent of the topography.[12] The phase contrast can be either positive or negative which corresponds to attractive or repulsive forces

between the tip and the sample. Thick FePt NP patterns were prepared by using a concentrated solution of NPs. A drop of a 20 mg/ml solution of FePt NPs in hexane was deposited on a PMMA-PUD patterned alumina sample. The NPs precipitated on the surface upon evaporation of hexane and formed a multilayer due to the high concentration. Then the sample was gently immersed in acetone to remove PMMA without damaging the NP layer. The sample was further annealed to transfer the nanoparticle into its ferromagnetic $L1_0$ phase.[25] Instead of a monolayer, a thick layer was used to have a strong enough magnetic signal for MFM measurement. Figure 7.8 shows the AFM and corresponding MFM image of the FePt lines after annealing, which were recorded simultaneously. The height of the patterns was about 35 nm which corresponds to 8-9 layers of NPs and the width was around 5 μm (Figure 7.8a). The magnetic contrast in the MFM phase image is clearly visible, but is not identical to the height image (Figure 7.8). This is due to the random momentum directions of the NPs giving a non-homogeneous magnetic contrast. In other words, some NPs attract the magnetic tip while others repel the magnetic tip. At some regions the magnetic contrast is weaker than at other places which may be due to the small particle size, differences in coverage, or to the momentum direction of NPs being perpendicular to the magnetization of the tip.
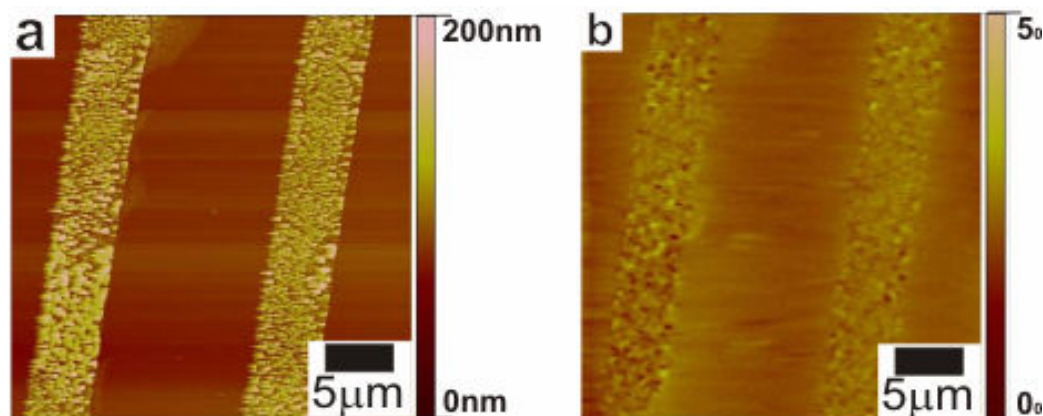

Figure 7.8 AFM height (a) and MFM phase (b) images of FePt NP multilayer patterns after annealing under reducing environment (96%Ar/4%H$_2$) for 2 h at 800°C.

7.2.10 Multilayers of PO$_3$-terminated FePtAu NP patterns prepared by NAMIC

PO$_3$-NPs were used to create NP patterns on PUD-modified alumina, by nanomolding in capillaries (NAMIC), as illustrated in Figure 7.9a. The main reason to

use PO_3-NPs dispersed in ethanol+Et_3N is to prevent swelling of PDMS. Hexane was not used as a solvent, because it would destroy uniform contact and cause pattern deformation upon swelling. As seen in Figure 7.9b,c continuous nanolines of FePtAu NPs were prepared without obvious defects over a large area. The shape of the pattern is in good agreement with the stamp used. The width of the NP patterns are close to the width of the nano-channels (Figure 7.9e). Multilayers were achieved probably due to irreversible aggregation during drying. The height of the NP patterns was around 70 nm which corresponds to 15-20 layers of NPs. This value is lower than the nano-channel height (100 nm). This may be due to shrinkage after drying, to a low concentration of particles in the NP dispersion, or to the use of oxygen plasma on the mold before NAMIC. NAMIC enables to prepare densely packed NP multilayers, the height can be controlled by the height of the channels.
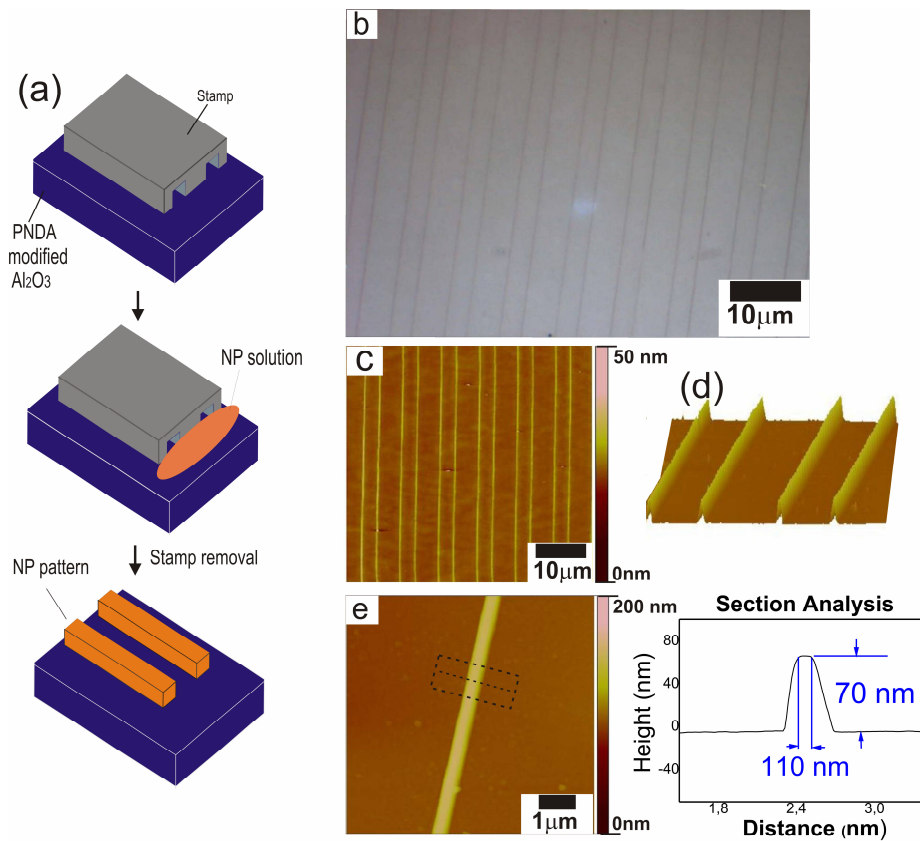

Figure 7.9. (a) The NAMIC process. FePt Au patterns prepared by NAMIC on a PUD-modified alumina substrate, (b) optical image, (c,e) AFM height image with section analysis, (d) 3D AFM topography image.

7.3 Conclusions

We have shown that NIL and self-assembly combined with phosph(on)ate based PUD and MUP SAMs having different end-groups can be an effective tool to fabricate line and dot patterns of FePtAu NP patterns with high contrast between patterned and non-patterned regions with a high resolution below 150 nm as well as in micron range. Multilayer NP nano-patterns can be prepared by NAMIC. Metal structures can be created on top of these by electroless deposition. MFM shows the magnetic property of the ferromagnetic FePt NP patterns. Applying an external magnetic field during assembly of ferromagnetic FePtAu NPs results in partial magnetic alignment of the NPs. The here developed process may be used in the micro-electronic industry and in fabrication of spintronic devices.

7.4 Experimental
Materials

Polished substrates of R-(1-102) Al_2O_3 (1x10x10 mm) and (100) $SrTiO_3$ were purchased from SurfaceNet GmbH, Germany. These substrates were cleaned by ultrasonication in acetone and ethanol for 30 min each. Tetradecylphosphoric acid (TDP) was supplied by A. Wagenaar and J. Engbersen (RUG, Groningen). Phosphonoundecanoic acid (PUD, purity 96%), PMMA (weight-average molecular weight, M_w 350kD), *N*-[3-(trimethoxysilyl)propyl)ethylene]-diamine, $Pt(acac)_2$, oleic acid and silver enhancer solutions a and b were purchased from Sigma-Aldrich. Oleyl amine was purchased from Fluka. Hexadecanediol and iron pentacarbonyl were purchased from ABCR. Mercaptoundecyl phosphonic acid (MUP) was synthesized according to a literature method.[26]

Synthesis of FePtAu NPs

The NPs were prepared using a modification of the reported procedure by Jia et. al.[27] The synthesis were performed by heating the precursors' solution at 350° for 3 h. At first, a solution of platinum acetylacetonate (0.5 mmol), gold acetate (0.35 mmol), and 1,2-hexadecanediol (1.5 mmol) in 20 mL octyl ether and 20 mL hexadecylamine was heated up to 100° C in a three-necked, round-bottom flask under a nitrogen atmosphere. To this solution was added, via syringe, oleic acid (0.5 mmol), oleylamine (0.5 mmol), and iron pentacarbonyl (1 mmol). The mixture was heated to reflux and allowed to reflux for 3 h resulting in a black dispersion. Then the heat

source was removed and the dispersion was allowed to cool to the room temperature. The inert gas protected solution could then be opened to ambient environment. Adding 40 mL of ethanol led to precipitation of the black product. The mixture was centrifuged to isolate the particles from the brown supernatant. The particles were redispersed in hexane, precipitated with ethanol, and isolated by centrifuging. The particles were dried at room temperature in a vacuum oven to give 100–200 mg of particles. The dispersion and precipitation removed impurities. During synthesis, the relative amounts of platinum acetylacetonate and iron pentacarbonyl and gold acetate were fixed in order to produce NPs with similar compositions (FePt)$_{85}$Au$_{15}$.

Synthesis of PO$_3$ terminated FePtAu NPs

The NPs were prepared using a modification of the procedure reported by Bagaria *et. al.*[16] Cyclohexanone was chosen as the solvent for the ligand exchange because it dissolves FePt NPs and mercaptoundecylphosphonic acid (MUP). A solution of MUP was prepared by mixing 2.7 mg MUP with 5 ml cyclohexanone. 50 mg of FePtAu nanoparticles dispersed in 0.5 ml hexane was added to this solution. The mixture stired overnight, then centrifuged and the supernatant was discarded. Cyclohexanone (10 ml) was added to the precipitate to remove FePtAu with oleic acid and oleylamine ligands and any excess MUP. The solution was centrifuged and the supernatant was discarded. As a final cleaning, the precipitate was mixed with 10 ml acetone. The solution was again centrifuged and the supernatant was discarded. The particles were then dispersed in 3ml of ethanol:Et$_3$N (10:1).

Nanoparticle assembly in a magnetic field

ABP modified SrTiO$_3$ subtrate was immersed in a dilute FePtAu solution overnight at 4 ^{o}C under 7000 Oe magnetic field and rinsed with hexane afterwards. A similar control sample was used for assembly of NPs without external magnetic field. The samples were further analysed by VSM to see the effect of alignment in the magnetic field.

Nanoimprint lithography (NIL)

The molds were fabricated by photolithography followed by reactive-ion etching (RIE, Elektrotech Twin system PF 340) or by EBL followed by titanium evaporation and lift-off. They consisted of 5 μm wide lines at 15 μm period, 3 μm lines with 8 μm period with a height of 570 nm or 100 nm lines with around 4 μm period with a height of 125 nm.

1*H*, 1*H*, 2*H*, 2*H*-perfluorodecyltrichlorosilane was used as an anti-adherent layer to facilitate the stamp-imprint separation. Al_2O_3 substrates were cleaned by oxygen-plasma for 7 minutes and covered with a 460 nm thick layer of PMMA by spin-coating in case of micron size patterning. Stamp and substrate were put in contact and pressure of 40 bar was appliedat 180 ^{o}C using a hydraulic press (Specac). The residual layer was removed by dipping the samples in acetone for 25 sec or by oxygen-plasma for 90 s using a RIE system. For nano patterns 120 nm thick PMMA and 18 s RIE was done. In the last step of NP pattern fabrication, the polymer layer was removed by 5 minutes acetone followed by 5 minutes chloroform immersion. For TDP SAM patterns, polymer layer was removed by 3 hours ultrasonication in acetone. The imprint cycle was 30 min.

Monolayer patterning using NIL

PMMA paterned Al_2O_3 substrates were immersed into 0.125 mM TDP solution in 100:1 v/v hexane:isopropanol, a 1 mM PUD solution in 50:50 v/v ethanol:H_2O or a 0.5mM mM MUP solution in ethanol for 2 days at room temperature. Afterwards, the samples were rinsed with the corresponding pure solvents or solvent mixtures, and dried under a flow of N_2.

Nanoparticle assembly

Al_2O_3 substrates covered with PMMA and self-assembled monolayer (SAM) patterns of PUD or MUP were immersed into a FePtAu (0.250 mg/ml) NP solution for 10-95 min to assemble NPs on the modified Al_2O_3 surfaces. For VSM measurement, fully MUP-covered Al_2O_3 substrate was immersed into a FePtAu (0.250 mg/ml) solution for 10 min. Subsequently the samples were rinsed with pure hexane to wash off physisorbed particles. After PMMA removal, samples were imaged by AFM.

Electroless deposition of Ag

The sample having FePtAu NP patterns attached to Al_2O_3 by MUP were immersed into a mixture of silver enhancer solutions for 20 minutes. Afterwards, the samples were rinsed with H_2O and ethanol, and dried under a flow of N_2. For the activation of SH end groups, a similar sample was immersed in $AgNO_3$ and $NaBH_4$ solutions for 1 min prior to Ag electroless deposition.

Nanomolding in capillaries (NAMIC)

Before NAMIC, the PDMS nanomold was shortly treated with oxygen plasma to to promote adhesion upon contacting the substrate.[28] 100 nm line features with 100 nm height was brought into conformal contact with PUD-functionalized alumina

substrates. A drop of PO$_3$-terminated FePtAu NPs functionalized with MUP and dispersed in ethanol:Et$_3$N was put at one part of the PDMS for filling in the channels through capillary force. Here, FePtAu dispersed in hexane was not used since hexane causes swelling of PDMS which would cause non-uniform contact between the stamp and the substrate.

The sample was left for solvent evaporation and NP precipitation in the nano-channels. After 10 hr the PDMS was removed, the residual polymeric material was rinsed with xylene followed by oxygen plasma and the substrate with line patterns of FePtAu was imaged by AFM and optical microscopy.

Measurements

Atomic force microscopy (AFM): The morphology of the nanoparticle-covered surfaces was observed by a digital multimode Nanoscope III (Digital Instruments, Santa Barbara, CA) scanning force microscope, equipped with a J-scanner. All measurements were done at ambient in tapping mode, contact mode. The magnetic force microscopy (MFM) was done by a Dimension 3100 (Digital Instruments, Santa Barbara, CA). The MFM tips are provided by SmartTip (type SC-20-M)

Vibrating Sample Magnetometer (VSM): Magnetic studies were carried out using a DMS Vibrating Sample Magnetometer (model VSM10) with fields up to 1500 kA/m and a sensitivity of 10^{-6} mAm^2. Measurements were done on NP assembly on MUP-modified Al$_2$O$_3$ substrate.

X-Ray Diffractometry (XRD): The nanoparticle samples after annealing were analyzed by powder X-ray diffraction (XRD) analysis using a Philips X'Pert diffractometer (CuK$_\alpha\lambda$ = 1.5418 Å).

High-Resolution Transmission Electron Microscopy (HRTEM-EDX): Particle sizes were analyzed by TEM (Philips CM-30 Twin operating at 200 kV voltage). A drop of hexane solution of the NPs was deposited on a carbon-coated copper grid.

7.5 References

1. Yakushiji, K.; Mitani, S.; Ernult, F.; Takanashi, K.; Fujimori, H., *Phys. Rep. Rev. Sec. Phys. Lett.* **2007,** *451*, 1.
2. Black, C. T.; Murray, C. B.; Sandstrom, R. L.; Sun, S. H., *Science* **2000,** *290*, 1131.
3. Liu, K.; Nogues, J.; Leighton, C.; Masuda, H.; Nishio, K.; Roshchin, I. V.; Schuller, I. K., *Appl. Phys. Lett.* **2002,** *81*, 4434.
4. Kinge, S.; Gang, T.; Naber, W. J. M.; Boschker, H.; Rijnders, G.; Reinhoudt, D. N.; van der Wiel, W. G., *Nano Lett.* **2009,** *9*, 3220.
5. Sun, S. H.; Murray, C. B.; Weller, D.; Folks, L.; Moser, A., *Science* **2000,** *287*, 1989.

6. Acet, M.; Mayer, C.; Muth, O.; Terheiden, A.; Dyker, G., *J. Cryst. Growth* **2005,** *285*, 365.
7. Sun, S. H.; Anders, S.; Hamann, H. F.; Thiele, J. U.; Baglin, J. E. E.; Thomson, T.; Fullerton, E. E.; Murray, C. B.; Terris, B. D., *J. Am. Chem. Soc.* **2002,** *124*, 2884.
8. Sun, S. H.; Anders, S.; Thomson, T.; Baglin, J. E. E.; Toney, M. F.; Hamann, H. F.; Murray, C. B.; Terris, B. D., *J. Phys. Chem. B* **2003,** *107*, 5419.
9. Yu, A. C. C.; Mizuno, M.; Sasaki, Y.; Inoue, M.; Kondo, H.; Ohta, I.; Djayaprawira, D.; Takahashi, M., *Appl. Phys. Lett.* **2003,** *82*, 4352.
10. Sugimura, H.; Hozumi, A.; Kameyama, T.; Takai, O., *Adv. Mater.* **2001,** *13*, 667.
11. Sun, S. Q.; Leggett, G. J., *Nano Lett.* **2007,** *7*, 3753.
12. Guo, Q. J.; Teng, X. W.; Yang, H., *Nano Lett.* **2004,** *4*, 1657.
13. Sun, S. H., *Adv. Mater.* **2006,** *18*, 393.
14. Huang, T. W.; Huang, Y. H.; Tu, T. H.; Lee, C. H., *J. Magn. Magn. Mater.* **2004,** *282*, 127.
15. Huang, T. W.; Yu, K. L.; Liao, Y. F.; Lee, C. H., *J. Appl. Crystallogr.* **2007,** *40*, S480.
16. Bagaria, H. G.; Ada, E. T.; Shamsuzzoha, M.; Nikles, D. E.; Johnson, D. T., *Langmuir* **2006,** *22*, 7732.
17. Gawalt, E. S.; Avaltroni, M. J.; Koch, N.; Schwartz, J., *Langmuir* **2001,** *17*, 5736.
18. Gnauck, M.; Jaehne, E.; Blaettler, T.; Tosatti, S.; Textor, M.; Adler, H. J. P., *Langmuir* **2007,** *23*, 377.
19. Liakos, I. L.; Newman, R. C.; McAlpine, E.; Alexander, M. R., *Langmuir* **2007,** *23*, 995.
20. Messerschmidt, C.; Schwartz, D. K., *Langmuir* **2001,** *17*, 462.
21. Textor, M.; Ruiz, L.; Hofer, R.; Rossi, A.; Feldman, K.; Hahner, G.; Spencer, N. D., *Langmuir* **2000,** *16*, 3257.
22. Kang, S. S.; Jia, Z. Y.; Shi, S. F.; Nikles, D. E.; Harrell, J. W., *Appl. Phys. Lett.* **2005,** *86*.
23. Grechishkin, R. M.; Soshin, S. S.; Ilyashenko, S. E., Angular variation of magnetization reversal process in high coercive multidomain uniaxial ferromagnets. In *First International Workshop on Simulation of Magnetization Processes*, Vienna, 1995; pp 72.
24. Suponev, N. P.; Grechishkin, R. M.; Lyakhova, M. B.; Pushkar, Y. E., *J. Magn. Magn. Mater.* **1996,** *157*, 376.
25. Yildirim, O.; Gang, T.; Kinge, S.; Reinhoudt, D. N.; Blank, D. H. A.; van der Wiel, W. G.; Rijnders, G.; Huskens, J., *Int. J. Mol. Sci.* **2010,** *11*, 1162.
26. Lee, T. R.; Carey, R. I.; Biebuyck, H. A.; Whitesides, G. M., *Langmuir* **1994,** *10*, 741.
27. Jia, Z. Y.; Kang, S. S.; Nikles, D. E.; Harrell, J. W., *IEEE Trans. Magn.* **2005**, 3385.
28. Duan, X. High-Resolution Imprint and Soft Lithography for Patterning Self-assembling Systems. PhD Thesis, University of Twente, Enschede, 2010.

Summary

This thesis describes the use of phosph(on)ate-based self-assembled monolayers (SAMs) to modify and pattern metal oxides. Metal oxides have interesting electronic and magnetic properties such as insulating, semiconducting, metallic, ferromagnetic etc. and SAMs can tailor the surface properties. FePt nanoparticles (NPs) are promising candidates for magnetic data storage applications due to their superior properties. In this thesis, the use of SAMs on conducting metal oxides for electrical applications and at the adsorption of magnetic NPs for data storage applications have been studied. By combining patterning techniques and self-assembly, functional inorganic-organic composite structures have been created.

Chapter 1 provides a general introduction to this thesis.

In Chapter 2, a literature overview of SAMs on metal oxides is given. SAM types were compared in terms of SAM formation (bond mechanism, interaction between the head-group and substrate surface, growth mechanism), quality (coverage, packing, order), structure (configuration) and stability. Techniques to pattern metal oxides with SAMs and several examples where SAMs were used in biomaterial or electronic applications, or as protective layers were covered. Phosp(on)ate-based molecules were found to form more densely packed, more ordered and more stable SAMs on metal oxides when compared to alkanoic acid-based molecules. At the same time, opportunies for further research have been identified.

In Chapter 3, the assembly of phosph(on)ate-based SAMs with CH_3, NH_2, SH, COOH end groups on single crystalline-aluminum oxide (Al_2O_3) substrates is described. SAMs were bound to the substrate through the phosph(on)ate headgroups, had a homogeneous and high coverage, a tails-up orientation and a certain degree of order. This was shown by contact angle (CA), atomic force microscopy (AFM), X-ray photoelectron spectroscopy (XPS) and Fourier transform infrared spectroscopy (FTIR). The thickness of a TDP layer was smaller than the length of an extended TDP molecule. This indicated a tilt in the SAM layer. There was no indication of in-plane registry between the surface atoms of the substrate and the phosph(on)ate headgroup. To create chemically different regions, SAM patterns were prepared on Al_2O_3 by microcontact printing.

In Chapter 4, the electrochemical properties of SAMs on conducting metal oxide Nb-STO are addressed. Unlike thiols on gold, the alkylphosphate SAMs on Nb-STO showed electrochemical stability over a wide voltage range of -2 to +2V as shown by cyclic voltammetry (CV). SAMs formed an insulating layer and inhibited the electrochemical activity of Nb-STO with an efficiency increasing with chain length. SAM-modified Nb-STO substrates had a higher resistance than bare substrates as shown by electrochemical impedance spectroscopy (EIS). Phosph(on)ate based-SAMs proved to be effective to electrically isolate the metal oxide surface and provided a stable system for electrochemical studies. This opens new possibilities to study electrochemical properties of semiconductors.

Chapter 5 describes the low kinetic energy deposition of Pt top contacts on alkylphosphate SAMs by pulsed laser deposition (PLD) and electrical characterization of these SAMs on a conducting Nb-STO metal oxide susbtrate. Electrochemical Cu deposition showed that almost 100 % of the top contacts were insulated from the substrate by the SAM which shows the dense packing and robustness of the SAM. As a control experiment top contacts were prepared on a bare substrate without a SAM layer and Cu growth was seen on all of the Pt contacts. I-V measurements showed that SAM modification caused a dramatic decrease in the leakage current when compared to bare Nb-STO, which proved the efficiency of SAMs as dielectric organic thin films. The ability to prepare top electrodes with very high yield without crashing into the SAM layer opens new possibilities for the use of phosph(on)ate-based dielectric organic thin films on metal oxides for electronic device fabrication.

Chapter 6 describes the controlled assembly of FePt NPs on phosph(on)ate-based SAM-modified Al_2O_3 substrates. The NP coverage on Al_2O_3 substrates modified with organic monolayers could be controlled by varying the immersion time into a FePt NPs solution. NPs probably assembled on NH_2 or COOH-terminated SAM-covered surfaces by ligand exchange since no assembly was observed when a CH_3-terminated SAM was used. This provided the possibility to control the adhesion of NPs on surfaces by changing the surface chemistry. The morphology and coverage of the NP assemblies were observed by AFM and their ferromagnetic properties were studied before and after thermal annealing by a vibrating sample magnetometer (VSM). Alumina substrates were patterned by microcontact printing using NH_2-terminated molecules as the ink, allowing local NP assembly. Thermal annealing under reducing conditions ($96\%N_2/4\%H_2$) led to a phase change of the FePt NPs from

the disordered FCC phase to the ordered FCT phase. This resulted in ferromagnetic behavior at room temperature.

Chapter 7 presents the preparation of high-resolution FePtAu NP patterns on an Al_2O_3 surface prepared by nanoimprint lithography (NIL) and nanomolding in capillaries (NAMIC). The polymer template generated by NIL behaved as a physical barrier and defined the patterned areas on the Al_2O_3 substrate. FePtAu nanoparticles (NPs) were assembled on phosph(on)ate SAM-modified polymer patterned substrates. After polymer removal, nano- and micro-scale, line and dot NP patterns were obtained on aluminum oxide substrates. Thick nanolines of NPs were obtained by NAMIC. FePtAu NPs are ferromagnetic as synthesized and therefore do not need to be annealed. Applying an external magnetic field during the assembly of FePtAu NPs on SAM-modified $SrTiO_3$ (STO) resulted in angle-dependent magnetic properties which showed partial alignment of the NPs. The magnetic properties of the ferromagnetic NPs were addressed by VSM and those of the patterned NPs by magnetic force microscopy (MFM). The results showed that NIL combined with surface chemistry is a powerful method to create well-defined high resolution NP patterns over large areas. The process described in Chapters 6 and 7 can potentially be used in the fabrication of spintronic devices.

The results described in this thesis show the versatility and efficiency of the use of phosph(on)ate-based SAMs to modify metal oxide surfaces. The use of SAMs on conducting metal metal oxides opens new possibilities for electrochemical studies. Metal top contact fabrication without causing shorts between the SAM and the substrate, combined with the insulating efficiency of the SAM, is promising for electrical device fabrication as well as for fundamental studies to understand the electrical properties of organic monolayers. Combining patterning techniques with chemical modification achieved by SAMs for controlled assembly and patterning magnetic nanoparticles on metal oxides can be used to prepare spintronic devices. By selecting the metal oxide properly, magnetic tunnel junctions can be fabricated. In principle, the surface modification and fabrication approach described throughout this thesis is applicable to a wide variety of metal oxides and NPs. This brings new possibilities for fabrication of functional hybrid organic-inorganic structures.

Samenvatting

Dit proefschrift beschrijft het gebruik van fosfaat-gebaseerde zelf-georganiseerde monolagen (SAMs) om metaal oxiden te veranderen en te vormen. Metaal oxiden hebben interessante elektronische en magnetische eigenschappen zoals isoleren, half-geleiding, metallisch, ferro-magnetisch, etc. Hun oppervlakte eigenschappen kunnen door SAMs bepaald worden. FePt nanodeeltjes zijn veelbelovende kandidaten voor toepassingen in magnetische gegevens opslag vanwege hun superieure eigenschappen. In dit proefschrift zijn bestudeerd het toepassen van SAMs op geleidende metaal oxiden voor elektrische toepassingen, en de absorptie van magnetische nanodeeltjes op de SAMs voor toepassingen zoals gegevens opslag. Door het combineren van patroon-vormende en zelf-organiserende technieken, zijn functionele anorganisch-organisch samengestelde structuren gecreëerd.

Hoofdstuk 1 verschaft een algemene inleiding tot dit proefschrift.

In Hoofdstuk 2 wordt een overzicht gegeven van het effect van SAMs op metaal oxiden. SAM types werden vergeleken in aspecten zoals SAM vorming (hechtingmechanismen, interactie tussen hoofd-groep en substraat oppervlak, groei mechanismen), kwaliteit (bedekking, stapeling, ordening), structuur (configuratie) en stabiliteit. Technieken om metaal oxiden te ordenen met behulp van SAMs, en diverse voorbeelden waarin SAMs werden gebruikt in biomateriaal of elektronische toepassingen, of als beschermende lagen werden behandeld. Fosfaat gebaseerde moleculen bleken SAMs met grotere dichtheid, meer ordening en meer stabiliteit te vormen op metaal oxiden indien ze vergeleken werden met alkanoïsche zuur-gebaseerde moleculen. Tevens werden mogelijkheden voor verder onderzoek geïdentificeerd.

In Hoofdstuk 3 is het samenstellen van fosfaat-gebaseerde SAMs met CH_3, NH_2, SH, COOH eindgroepen op substraten van enkel-kristallijn aluminiumoxide (Al_2O_3) beschreven. SAMs werden door de fosfaat hoofdgroepen aan het substraat gebonden, hadden een homogene en hoge graad van bedekking, een gelijkgerichte oriëntatie en een zekere mate van ordening. Dit werd aangetoond door contact hoek (CA), atoomkracht microscopie (AFM) en X-ray foto-elektrische spectroscopie (FTIR). De dikte van een TDP laag was kleiner dan de lengte van een verlengd TDP

molecuul. Dit gaf een schuinte of helling in de SAM laag aan. Er was geen aanwijzing voor een overeenkomst in de in-vlak structuur van het substraat en de fosfaat hoofdgroepen van de SAM laag. Om chemisch verschillende regio's te creëren, werden SAM patronen gemaakt op Al_2O_3 door middel van microcontact drukken.

Hoofdstuk 4 houdt zich bezig met de elektrochemische eigenschappen van SAMs op het metaal oxide Nb-STO. In tegenstelling met thiolen op goud, lieten de alkielfosfaat SAMs op Nb-STO elektro-chemische stabiliteit zien over een wijde spannings schaal van -2 tot +2V, zoals aangetoond met cyclische voltametrie (CV). SAMs vormden een isolerende laag en beperkten de elektro-chemische activiteiten van Nb-STO met een per keten lengte toenemende efficiëntie. SAM-gemodificeerde Nb-STO substraten hadden een hogere weerstand dan lege substraten, zoals aangetoond door elektro-chemische impedantie spectroscopie (EIS). SAMs bewezen effectief het metaal oxide oppervlak elektrisch te isoleren en leverden een stabiel systeem voor elektro-chemische studies. Dit voorziet in nieuwe mogelijkheden om elektro-chemische eigenschappen van halfgeleiders te bestuderen.

Hoofdstuk 5 beschrijft de laag-kinetische energie depositie van Pt top contacten op alkylfosfaat SAMs door middel van gepulseerde laser depositie (PLD) en de elektrische karakterisering van deze SAMs op een geleidend Nb-STO substraat. Elektro-chemische Cu depositie toonde aan dat bijna 100 % van de top contacten werden geïsoleerd van het substraat door de SAMs, hetgeen de dichte stapeling en de robuustheid van de SAMs aantoonde. Als controle experiment, werden top contacten gemaakt op een leeg substraat zonder een SAM, en Cu groei werd waargenomen op alle Pt contacten. I-V metingen toonden aan dat veranderingen in SAMs een dramatische afname in de lekstromen veroorzaakten, indien vergeleken met naakt Nb-STO, hetgeen de efficiëntie van SAMs als di-elektrische organische dunne films bewees. Het vermogen om top elektroden met zeer hoge opbrengst te prepareren die de SAM niet beschadigen opent nieuwe mogelijkheden voor het gebruik van fosfaat gebaseerde di-elektrische organische dunne films op metaal oxiden voor het fabriceren van elektronische entiteiten.

Hoofdstuk 6 beschrijft het gecontroleerd ordenen van FePt nanodeeltjes op door SAMs gemodificeerde Al_2O_3 substraten. De dekking door middel van nanodeeltjes op Al_2O_3 substraten, gemodificeerd met organische mono-lagen, kon gecontroleerd worden door de onderdompelingstijd in een FePt nanodeeltjes oplossing

te variëren. Nanodeeltjes verzamelden zich op NH_2 of COOH-eindigende door SAM bedekte oppervlakken door ligand uitwisseling aangezien geen verzameling geobserveerd werd wanneer een CH3-eindigende SAM werd gebruikt. Dit verschafte de mogelijkheid om de aanhechting van nanodeeltjes op oppervlakken te controleren door de oppervlak chemie te variëren. De morfologie en bedekking door de nanodeeltjes verzamelingen werden geobserveerd door AFM, en hun ferromagnetische eigenschappen werden bestudeerd voor en na thermisch uitgloeien door een vibrerende monster magnetometer (VSM). Alumina substraten werden geordend door microcontact drukken, waarbij NH2-beëindigde moleculen als inkt gebruikt werden, wat lokale nanodeeltjes ordening mogelijk maakte. Thermische uitgloeing onder reducerende omstandigheden ($96\%N_2/4\%H_2$) leidde tot een fase verandering van de FePt nanodeeltjes, van de ongeordende FCC fase naar de geordende FCT fase. Dit resulteerde in ferromagnetisch gedrag bij kamertemperatuur.

Hoofdstuk 7 beschrijft de preparatie van hoge-resolutie FePtAu-nanodeeltjes patronen op een Al_2O_3 oppervlak voorbereid door nanoafdruk lithografie (NIL) en nano vorming in capillairen (NAMIC). De polymeer ondergrond voorgebracht door NIL gedroeg zich als een fysieke barrière en bepaalde de gebieden met geordende patronen op het Al_2O_3 substraat. FePtAu-nanodeeltjes werden samengesteld op polymeer geordende substraten, gemodificeerd door fosfaat SAMs. Na verwijdering van het polymeer, op nano- en micro-schaal, werden lijn en punt patronen verkregen op aluminiumoxide substraten. Dikke nanolijnen werden door NAMIC verkregen. Wanneer gesynthetiseerd, zijn FePtAu nanodeeltjes ferromagnetisch en hoeven daarom niet nagegloeid te worden. Wanneer tijdens de samenstelling van FePtAu nanodeeltjes op SAM-gemodificeerde $SrTiO_3$ (STO) een extern magnetisch veld gebruikt werd resulteerde dit in hoek-afhankelijke magnetische eigenschappen die een gedeeltelijke gerichtheid van de nanodeeltjes toonde. VSM richtte zich op de ferromagnetische eigenschappen van nanodeeltjes, Magnetische Kracht Microscopie (MFM) op die van de geordende nanodeeltjes. Resultaten toonden dat NIL in combinatie met oppervlak chemie een krachtige methode is om goed-gedefiniëerde hoog-resolutie patronen in nanodeeltjes over grote gebieden te maken. Het proces beschreven in Hoofdstukken 6 en 7 kan potentieel gebruikt worden bij de fabricage van spintronische entiteiten.

De resultaten beschreven in dit proefschrift tonen de veelzijdigheid en efficiëntie van het gebruik van fosfaat gebaseerde SAMs om oppervlakken van metaal oxiden te wijzigen. Het gebruik van SAMs op geleidende metaal oxiden opent nieuwe mogelijkheden voor onderzoeken op het gebied van de elektrochemie. Metaal top contact fabricage zonder het veroorzaken van kortsluitingen tussen SAMs en substraten, gecombineerd met de isolatie efficiëntie van SAMs, is veelbelovend voor de fabricage van elektrische entiteiten. Dit geldt ook voor fundamentele studies naar het begrijpen van de elektrische eigenschappen van organische enkelgelaagden. Wanneer ordeningstechnieken gecombineerd worden met chemische modificatie bereikt door SAMs, voor gecontroleerd samenstellen en ordenen van nanodeeltjes op metaal oxiden, dan kunnen zij gebruikt worden voor de fabricage van spintronische entiteiten.

Bij het selecteren van het juiste metaal oxide, kunnen magnetische tunnel juncties gefabriceerd worden. In principe is de benadering van oppervlak modificatie en fabricage, die overal in dit proefschrift beschreven is, toepasbaar op een grote verscheidenheid van metaal oxiden. Dit zorgt voor nieuw mogelijkheden voor de fabricage van functioneel hybride organisch-anorganische structuren.

Acknowledgements

About the Author

Oktay Yildirim was born in Turkey, on May 1977. He studied chemical engineering at Middle East Technical University (METU), Ankara, Turkey and obtained his bachelor degree in 2000. He started master education at Izmir Institute of Technology (IZTECH), Department of Material Science and Engineering, (September 2001 – September 2004) under the supervision of Prof.Dr. Muhsin Ciftcioglu and Prof.Dr. Sebnem Harsa. His master thesis was titled 'Preparation and characterization of chitosan/calcium phosphate based composite biomaterials'. He started PhD at chemical engineering IZTECH, on biomaterials but did not finish due to the transfer to University of Twente. He worked as a Research and Teaching Assistant at IZTECH between 2001-2006. Since April 2006 he was a PhD candidate under the supervision of Prof.Dr.Ir. Jurriaan Huskens and Prof.Dr.Ing. Guus Rjinders at the University of Twente, at Molecular Nanofabrication (MnF) and Inorganic Materials Science (IMS) groups. His research was on self-assembled monolayers on metal oxides. The results of his research work are described in this thesis. Since October 2010, he is employed by TMC Physics B.V. The Netherlands.